THEORETICAL AND EXPERIMENTAL ANALYSIS OF TWO-PHASE CLOSED THERMOSYPHONS

By

Jianfeng Xu

RECOMMENDED:

Advisory Committee Chair

Chair, Department of Mechanical Engineering

APPROVED:

Dean, College of Engineering and Mines

Dean of the Graduate School

Apr 15, 2008

Date

THEORETICAL AND EXPERIMENTAL ANALYSIS OF TWO-PHASE CLOSED THERMOSYPHONS

A

THESIS

Presented to the Faculty of the University of Alaska Fairbanks

in Partial Fulfillment of the Requirements

for the Degree of

DOCTOR OF PHILOSOPHY

By

Jianfeng Xu, B.S., M.S.

Fairbanks, Alaska

May 2008

Abstract

This work presents an analytical and numerical model of a long inclined two-phase closed thermosyphon, known as a hairpin thermosyphon, which is representative of a new configuration for thermosyphons used in arctic applications. A laboratory experiment and a full scale road experiment along with associated modeling are described in detail.

The laboratory experiment studies the condensation heat transfer performance of carbon dioxide inside the thermosyphon condenser under conditions of limited heat flux. The operating condition is not far from the critical point for carbon dioxide, which has a significant impact on the condensation heat transfer. An experimental correlation is developed to predict the carbon dioxide condensation heat transfer performance under these specific conditions. The full scale road experiment studies the overall performance of hairpin thermosyphons under actual field conditions.

The model is a quasi one-dimensional formulation based on two-dimensional two-phase flow simulations at each cross section. The proposed model is useful for predicting steady state system operating characteristics such as pressure, temperature, liquid film thickness, mass flow rate, heat flow rate, etc., at local positions as well as over the entire system. The comparison of the modeling predictions with both laboratory and field experiments showed a strong correlation between modeling predictions and experimental results.

Table of Contents

Page

Page

Page

List of Figures

Page

Page

List of Tables

List of Appendices

Nomenclature

A	area, m^2
$C(z)$	phase change perimeter, m
D	inner diameter, m
c_P	specific heat, $J/(kg \cdot K)$
$\vec{F}$	body force, N
F_{fl}	fluid-dependent parameter
H	film thickness, m
h	heat transfer coefficient, $W/(m^2 K)$
k	thermal conductivity, $W/(m \cdot K)$
L	latent heat, J/kg
$\dot{M}$	mass generation $kg/(m^3 \cdot s)$
$\dot{m}$	effective mass source in cross section, $kg/(m^2 \cdot s)$
p	pressure, Pa
q	local heat flux, W/m^2
T	temperature, ^oC
u	velocity in x-direction, m/s
$\vec{V}$	velocity vector, m/s
v	velocity in y-direction, m/s
w	velocity in z-direction, m/s
x	x coordinate, m
y	y coordinate, m
z	z coordinate, m

Greek Symbols

α	thermal diffusivity, m^2/s
Δ	difference
θ	inclination angle of the thermosyphon, ^{o}
Φ	dissipation function (including the internal heat generation)
ρ	fluid density, kg/m^3
μ	dynamic viscosity, $Pa \cdot s$
υ	kinematic viscosity, m^2/s

Superscriptions

*	dimensionless parameter
$\rightarrow$	vector
$\cdot$	source term

Subscriptions

0	characteristic parameter
c	condenser
e	evaporator
l	liquid
v	vapor
w	wall
TP	two phase

Dimensionless Groups

$Bo = \frac{q}{GL}$ boiling number

$Co = \left(\frac{1-x}{x}\right)^{0.8} \left(\frac{\rho_g}{\rho_l}\right)^{0.5}$ convection number

$Fr_{lo} = \frac{G^2}{\rho_l^2 gD}$	Froude number with all flow as liquid
$Ja = \frac{c_{p,l}(T_{w,e} - T_{w,c})}{L}$	Jacob number
$Nu = \frac{hD}{k_l}$	Nusselt number
$Pr = \frac{\upsilon}{\alpha}$	Prandtl number
$Re = \frac{VD}{\upsilon}$	Reynolds number
$\Phi_l^* = -\frac{\rho_l g \sin\theta}{\mu_l} \cdot \frac{D^2}{w_0}$	dimensionless source term in the liquid phase
$\Phi_v^* = \frac{\partial P}{\partial z} \cdot \frac{1}{\mu_l} \cdot \frac{D^2}{w_0}$	dimensionless source term in the vapor phase

Acknowledgements

I would like to express my sincere appreciation to Professor Douglas J. Goering for his guidance throughout the course of this work. His advice has been invaluable. His diligence and scholarly excellence have been an inspiration. I believe the benefits will last a lifetime.

I would also like to thank Professor John P. Zarling, Professor Yuri Shur, and Professor Debendra K. Das for serving on my advisory committee. Their help, suggestions, and comments have been crucial to the completion of this work.

The funding and in-kind support from the Alaska Experimental Program to Stimulate Competitive Research (EPSCoR), the Alaska Department of Transportation (AKDOT), Arctic Foundations Inc., and Arctic Region Supercomputing Center (ARSC) are gratefully acknowledged.

I would also like to thank the faculty of the Department of Mechanical Engineering, in the College of Engineering and Mines, at the University of Alaska Fairbanks that have helped me during my study. They are Professors Jonah Lee, Gang Chen, Pin Lan, Vladimir Romanovski, Jing Zhang, Rorik Peterson, and Ed Barger.

I am also indebted to Eric Johansen, Tom McCarty, Gary Porter, Paul Brown, Bob Andresen, Nickole Conley, Sarah Hall, and Linda Ilgenfritz for helping me with the experimental research and everyday work.

I would also like to thank my fellow students for their support. Graduate students Tom Moran from the EPSCoR office and Bryr Ludington from English Department helped me improve my English writing in this dissertation. I also received generous help from

Jingbo Li, Likun Wang, Hongyan Yuan, John Zhu, Weiyuan Wang, Xiang Fang, Srivathsan Ragunathan, Fugeng Dou, Jiaqi Huang, Teresa O'Brien, Rebecca Hazen, Grace Chang, Yu Zhang, Yiming Wang, and Wei Zhang.

Finally, I am deeply grateful to my mother, my wife, and my daughter. Their sacrifice, understanding, support, and inspiration have made it possible and meaningful for me to pursue an advanced degree.

Chapter 1 Introduction

1.1 The two-phase closed thermosyphon

A two-phase closed thermosyphon is a high-effective passive heat transfer device. It utilizes gravity to assist the working fluid circulation instead of the wick structure often seen in heat pipe designs.

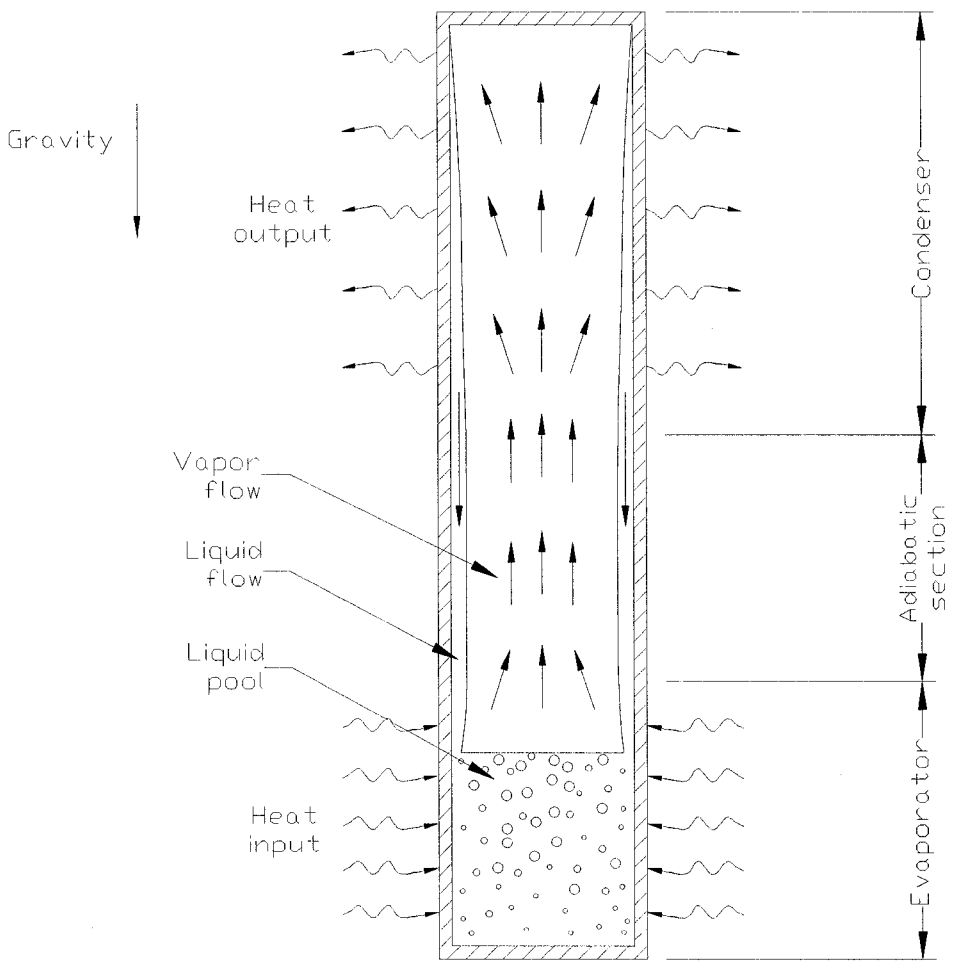

Figure 1.1 Two-phase closed thermosyphon.

As shown in Figure 1.1, the two-phase closed thermosyphon is basically a closed shell with a working fluid sealed inside. The shell is usually made of metal to provide high thermal conductivity and strength. Generally, a thermosyphon is composed of three functional parts: the evaporator, the adiabatic section, and the condenser.

When the thermosyphon is inactive, the liquid phase of the working fluid sits in the bottom of the thermosyphon with the rest of the space filled with vapor. The liquid and the vapor are in thermodynamic equilibrium.

When the evaporator is heated, this equilibrium is broken. Within the evaporator, heat absorbed from outside evaporates (boils) some liquid into vapor, which rises up through the adiabatic section into the condenser. In the condenser, heat is shed through the metal shell, causing the vapor to cool down and condense on the wall; the condensate then flows downward to the evaporator and the cycle continues. This circulation is thus driven both by the temperature difference and by gravity. As long as the lower end of the thermosyphon is warmer than the upper end, this circulation will continue and heat will be continuously transferred from the evaporator to the condenser.

There are three important properties that make the thermosyphon a unique and widely used heat transfer device: high heat transfer effectiveness, passive operation, and the thermal diode effect.

1.1.1 High heat transfer effectiveness and isothermal operation

The heat transfer process within the thermosyphon is via evaporation/condensation and fluid flow instead of via thermal conduction. In thermosyphon operation, the working fluid in both the evaporator and the condenser is at or near its saturation point. The pressure gradient required to drive the vapor from the evaporator to the condenser is generally small. Therefore, the temperature difference between the evaporator and the condenser is also small in most cases.

The high latent heat and low flow resistance make its heat transfer process much more efficient than pure heat conduction. Under certain circumstances, the thermosyphon's equivalent thermal conductivity can be three or four orders of magnitude higher than that of ordinary metal.

1.1.2 Passive operation

The operation of a thermosyphon is driven by gravity and the temperature difference along its length. No external power is needed to maintain this operation, making the thermosyphon a very reliable and economical form of heat transfer device.

1.1.3 Thermal diode effect

Because the thermosyphon operation is driven by temperature difference and gravity, the device only works when the higher temperature is imposed at the lower position with the low temperature above. If the temperature is higher on the top end, the fluid will not circulate and the thermosyphon will shut down. Therefore, the thermosyphon can also be utilized as a "thermal diode" or "thermo-switch" to control the direction of heat transfer.

Due to their excellent heat transfer characteristics, thermosyphons can be utilized in any field that requires heat transfer, including electronics cooling, aerospace engineering, nuclear reactors, waste heat recovery, and arctic engineering. One of the most well-known applications of thermosyphons in arctic regions is the Trans-Alaska Oil Pipeline (Alyeska Pipeline) system, which uses more than 114,000 thermosyphons to help stabilize the pipeline foundation throughout the permafrost areas.

1.2 Hairpin thermosyphon

The vast majority of previous installations that have utilized thermosyphons in arctic engineering have utilized air-cooled condensers with finned heat exchangers extending upward into the ambient air. In a roadway application, these air-cooled condensers represent both a safety hazard and an aesthetics issue since they typically line either side

of the roadway causing an unsightly collision hazard. In addition, the finned heat exchanger is typically the most expensive part of an air-cooled thermosyphon thus increasing the cost of manufacture.

In order to avoid the problems described above for air-cooled thermosyphons, hairpin thermosyphons represent a novel approach to thermosyphon design in that both the condenser and evaporator are buried beneath the ground surface. This type of configuration avoids the use of high-cost air-cooled heat exchangers and eliminates the safety and esthetic issues described above.

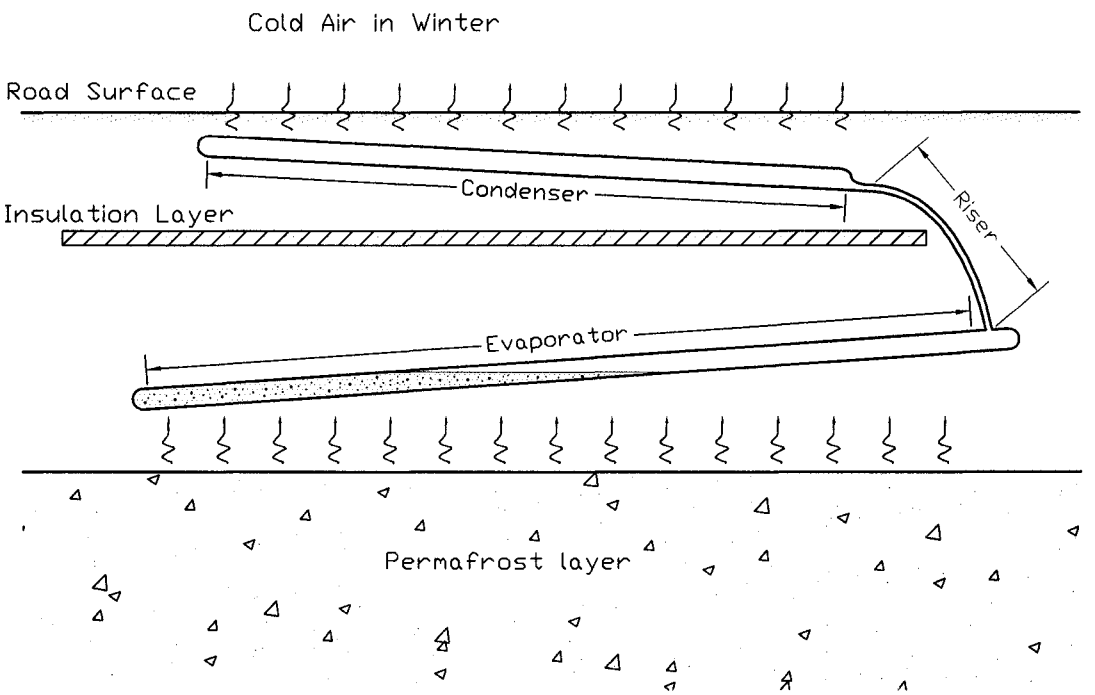

Figure 1.2 Hairpin thermosyphon.

As shown in Figure 1.2, the condenser is installed very close to the road surface to access the air temperature easily, while the evaporator is buried deep in the road foundation to extract heat from the surrounding embankment material and the permafrost layer. They

are both positioned at a small inclination angle to assist the circulation of the working fluid. The evaporator and the condenser are linked by a tube called a "riser," which functions as the adiabatic section of the thermosyphon.

Like other thermosyphons used in arctic engineering, hairpin thermosyphons are only active during the winter, when the soil temperature surrounding the condenser is lower than the foundation soil temperature surrounding the evaporator. In summer the thermosyphon shuts down because of the opposite direction of the temperature difference. To ensure the thermal diode effect of the system, a layer of horizontal insulation layer is placed just beneath the condensers to reduce the amount of heat from transferring back to the roadway embankment via the conduction mechanism during summer months.

1.3 Application background

Road projects in permafrost areas have suffered from high failure rates caused by melting permafrost and associated thaw settlement. These problems result from the thermal disturbances caused by construction activities, which typically involves removal of the native vegetation layers and replacement with granular fill. These changes tend to produce high surface temperatures during summer months because of increased solar absorption and reduced surface moisture. The surface warming eventually increases the temperature of the underlying permafrost causing thaw and settlement in areas where the permafrost is ice rich. Continual re-leveling operations and large maintenance costs are typically the results.

A number of techniques were developed to counteract the warming disturbance of road and railway embankments, and resist permafrost degradation and related thaw settlement. One class of these techniques employ passive cooling methods, which utilize the annual air temperature cycle to remove heat from the embankment passively. These technologies generally enhance the heat loss from the embankment during winter months without increasing summer heat gain, thus resulting in a passive cooling or a thermal

diode effect. The gravity-assisted two-phase closed thermosyphon is among the most effective.

In 2000, the Alaska Department of Transportation began a design for a new road building project near Fairbanks, Alaska. The project was to cross over a portion of previously undisturbed permafrost. Hairpin thermosyphons were utilized in order to reduce the possibility of failure due to permafrost thaw and associated thaw settlement.

1.4 Objective

The unique geometry and special working environment of the hairpin thermosyphon have an impact on the processes taking place within the thermosyphon and may affect the overall performance of the system in ways that are still largely unknown. To reach a better understanding of the inner processes and the overall performance of the hair-pin thermosyphon, a full scale road test and a lab experiment were carried out. In addition, a semi-numerical, semi-analytical model was developed to simulate the performance of the hairpin thermosyphon.

1.5 Scope of the dissertation

A literature review related to thermosyphon is given in the chapter to follow. A detailed description of the laboratory experiment and the full scale road test is given in Chapter 3. The modeling methods are described in detail in Chapter 4. Chapter 5 and Chapter 6 are two papers related to a thermosyphon condenser model and a thermosyphon model respectively. General conclusions and recommendations for future work are given in Chapter 7.

Chapter 2 Literature Review

2.1 History of thermosyphons

The earliest thermosyphons date back to the nineteenth century [70; 44; 75]. In 1836, J. Perkins, an American in England, invented the Perkins Tube, which is very similar in structure to modern thermosyphons; the only difference is that the non-condensable air is not removed before the charging of working fluid. The Perkins Tube found application in locomotive boilers and bread ovens. In 1892, J. Perkins's grandson, L. Perkins and his coworker, W. Buck, improved the Perkins Tube. They removed the non-condensable gas by boiling and venting part of the working fluid. After 1900, Perkins Tubes were mass-produced in Britain, the Soviet Union, and the Czech Republic for applications in bread ovens and automobile radiators. In 1929, F.W. Gay first attached fins on the evaporator and condenser of the thermosyphon to enhance the heat transfer.

From the early inventions grew the new standard heat pipe design, which was first put forward in 1942 by P.S. Gaugler. For the first time, a wick structure was used in the heat pipe to help the back flow of condensate. Gaugler referred to his design as a "Heat Transfer Device"; the name "Heat Pipe" was first used by G.M. Grover in 1963, who developed his heat transfer element independently in Los Alamos National Laboratory. The first application of thermosyphons in permafrost stabilization was in the early 1960's by E. Long [45; 46]. His patent was named "means for maintaining permafrost foundations." The space race of the 1960's and energy crisis of the 1970's both brought heat pipes to the attention of researchers across the globe, and heat pipes have been extensively studied both theoretically and experimentally ever since.

The following overview attempts to summarize the English-language references to thermosyphons in public journals and conferences from the 1950's. Because of the huge quantity of papers on this subject, only a selection of significant papers is included. This overview is organized into several categories according to the foci of the studies:

comprehensive performance, phase change, condensation, evaporation, flow pattern, working limits, inclination, aspect ratio, charge ratio, gas loading and reviews.

2.2 Comprehensive performance

Extensive research has been carried out on comprehensive thermosyphon performance since the 1970's. Much of this research has been experimental, especially during the early period. Because of the complexity of the processes taking place within a thermosyphon, the modeling is relatively difficult, and all models have had to employ significant assumptions. The following is a list of common assumptions that have been regularly made in the modeling efforts:

Steady state operation;
Tubular and vertical geometry;
One-dimensional Newtonian flow;
Thin and laminar liquid film;
Negligible compressibility;
Negligible sensible heat related to the sub-cooling and superheat;
Negligible pressure drop in the liquid film;
Negligible axial heat conduction; and
Negligible entrainment of liquid droplets.

The first comprehensive performance study was a simple theoretical model based on a dimensional analysis conducted by Y. Lee and Mital [42] in 1972. The interfacial friction between the vapor and liquid phase was deemed negligible for simplification. In the 1980's, F. Dobran [14; 15] created a "Lumped parameter" model of a two-phase thermosyphon. His model was later improved by C. Casarosa [4] by considering the liquid entrainment in the vapor core. J.G. Reed [55] proposed a comprehensive analytical model in 1987 as part of his Ph.D. research [54]. In this model, a vertical thermosyphon was divided into seven control volumes, in which complex processes were formulated

with experimental correlations. This control volume method was very successful in reducing the complexity of mathematical formulation and was adopted by C. Harley [26] and H. Farsi [18] in their modeling. However, this control volume method can only describe the overall performance of the thermosyphon; it is still difficult to determine the details of flow and heat transfer inside the thermosyphon.

Numerical methods may be a better approach to solving complicated equations in thermosyphon modeling and reveal more details of processes inside the thermosyphon. In 1974, C. Tien and A. Rohani [69] constructed the first numerical model for the vapor flow in a thermosyphon, examining the relation between the heat pipe performance and the vapor pressure drop. In 1994, Z. Zuo [84] adapted J.G. Reed's [54; 55] control volume method in a numerical model, in which the liquid-film momentum advection and axial normal stress in the countercurrent two phase flow were considered. Zuo also extended his numerical model to inclined thermosyphons [85], in which the inclination angle was classified into 3 different ranges. Zhou's work has been the only comprehensive model dealing with inclined thermosyphons. Another numerical simulation was provided by two Russian researchers, G. Kuznetsov and A. Sitnikow [39; 40], for a wicked heat pipe, in which evaporation, instead of boiling, was occurring in the evaporator. Because of the wick structure, the friction between the liquid and vapor phase was neglected.

Because of the different assumptions adopted by different researchers, the comprehensive models are all limited to certain a degree and are by no means universal. Most of the models were validated by experiments.

2.3 Phase change

As the key reason for high heat transfer performance of the thermosyphon, phase changes inside the thermosyphon are the most complicated processes in the device. Aside from thermosyphons, the extensive studies of phase change heat transfer problems are also driven by the demands of the power, refrigeration, nuclear, aerospace, and chemical

industries. According to J. Collier [12], due to the complex nature of the processes, "The fields of boiling and condensation are at present more of an art than a science and the subject remains, and will remain for some time to come, largely empirical." The only success in theoretical modeling of phase change has been in the area of laminar filmwise condensation as originally conducted by Nusselt in the early 1900's. Nusselt's theory, with a series of significant improvements, is still the basis of most successful condensation models. While in the dropwise condensation and boiling area, theories are still not good enough to give accurate predictions. Experimental or semi-empirical correlations are more practical ways to proceed.

2.3.1 Condensation

As the first successful attempt to analyze filmwise condensation, Nusselt's theory made a series of assumptions: laminar flow, constant properties, negligible subcooling, negligible momentum change, no interface shear, etc. To make the analysis more accurate, all of the later improvements focus on improving or removing one or more of the original assumptions. W. Rohsenow [56] allowed the non-linear distribution of temperature through the film due to energy convection and introduced a modified latent heat. E. Sparrow [61] removed the assumption of negligible momentum change with the boundary layer treatment. His study showed that the momentum change is indeed negligible unless the working fluid's Prandtl numbers are very low, such as for liquid metals. More recently, M. Chen [8], T. Spendel [62], S. Chen et al. [9] and others considered the influence of the drag on the liquid and vapor interface. Again, the original assumption of no interface shear appeared justified at Prandtl numbers around unity. Nusselt's theory was also extended to geometries other than flat plates by V. Dhir [13] and W. Kamminga [33].

More related to thermosyphon operation, condensation inside a pipe with a vertical or inclined orientation has been another active research area. J.C. Chato [5; 6] developed a momentum-energy integral method for the laminar condensate forming on the pipe wall

and on the bottom condensate flow in inclined tubes. Two correlations for heat transfer coefficient were provided for different inclination angles. U. Gross [22] developed another semi-empirical correlation for reflux condensation based on 66 experimental studies. J. Wang and Y. Ma [74] provided a semi-empirical correlation for the condensation heat transfer inside vertical and inclined thermosyphons. Their study showed that the heat flux and temperature difference has little effect on the divergence from Nusselt's theory. However, the inclination angle has a notable influence on the condensation coefficient. The reflux condensation was also studied by G. Chou [10], A. Narain [47] and Y. Pan [50], who believed that the reflux condensation heat transfer coefficient depends significantly on Biot number, interfacial shear, and momentum exchange.

Different from filmwise condensation, when the condensate cannot wet the solid surface, dropwise condensation occurs. The mechanism of dropwise condensation is more complicated and has not yet been understood completely. Y. Song et al. [60] and M. Jakob [32], etc., supported the theory of the existence of a very thin film between the drops, but more researchers, such as J.W. Rose [57; 58; 59], A. Umur and P. Griffith [71], believe that droplets only form on specific nucleation sites. Roughly speaking, the dropwise condensation can be considered to be a combination of several random processes: initial droplet formation, droplet growth, droplet coalescence, and droplet departure. More information about the dropwise mechanism is available in Tanasawa's [64] review. The randomness in the dropwise condensation also increases the difficulty of a model simulation.

The most successful dropwise condensation theory so far was introduced by J.W. Rose [57; 58; 59]. This modeling was based on steady conduction in each drop and the mean distribution of drop sizes. It was improved by M. Abu-Orabi [1] to consider the thermal resistance of the promoter layer and the vapor-liquid interface. Also based on J.W. Rose's single drop model, Y. Wu et al. [76] proposed a random fractal model. The

fractions of the area covered by drops of certain size were obtained from previous experiments. The results showed better agreement with the experimental data than J.W. Rose's prediction. For condensation outside a pipe, a series of studies were carried out by T. Hosokawa [28; 29] and T. Hosokawa et al. [31; 30]. Only sweeping action was included in the original modeling. When it was revised to consider the covering effect of the departing droplets, the results were claimed to have a better agreement with experimental data under low heat fluxes. The maximum heat transfer coefficient on an inclined tube was shown to occur at an angle of about 30 degrees. This conclusion was also supported by F. Ganzevles and van der Geld [21] experimentally, who found that a tilt angle enhances the drainage of condensate drops and the condensation heat transfer; the optimal angle is at about 35 degrees. A series of experiments were carried out by M. Xin and J. Xia [78] with Oleic acid and silicon oil as the promoters. As a result, two heat transfer correlations for dropwise condensation in the water thermosyphon were proposed. Other related experimental studies were also carried out by S. Hatamiya and H. Tanaka [27], A. Kananeh et al. [27; 34] and S. Vemuri and K. Kim [73] more recently.

2.3.2 Evaporation

In a thermosyphon, the evaporation process generally includes flow boiling and pool boiling. When the temperature difference between the condenser and evaporator is large, subcooled flow boiling is also likely to occur at the entrance of the evaporator. When the thermosyphon heat flux is extremely small, even convection of the working fluid may be strong enough to remove the heat from the thermosyphon wall. In this situation, there is no nucleation in the evaporator, the phase change occurrs on the liquid-vapor interface via evaporation.

Both flow boiling and pool boiling have been studied extensively. However, because of the complexities of the boiling mechanism, the basic physical process of boiling is still not completely understood. Some of the major complexities involved are bubble growth and departure behavior in the flow field of a two-phase mixture, distribution of the two

phases relative to each other and relative to the tube wall (flow pattern and entrainment effects), departure from thermodynamic equilibrium at local conditions, characteristics of the heat transfer surface, and the effects of fluid properties. A realistic comprehensive model addressing these complexities has not yet been developed. Experimental correlations are still the better way to predict the characteristics of boiling heat transfer in most cases.

In 1966, J.C. Chen [7] proposed a correlation for convective flow boiling heat transfer for nonmetallic fluids. The micro-convective (nucleate boiling) and macro-convective (non-boiling forced convection) heat transfer mechanisms were considered additive. This superposition approach was adopted by many later researchers, such as K. Gungor and R. Winterton [23; 24], S.G. Kandlikar [35], Z. Liu and R. Winterton [43], J. Thome and El Hajal [68], C.Y. Park and Hrnjak [51; 52], H. Steiner et al. [63] and W. Zhang et al. [82]. Because of the coupling of convective flow and nucleate boiling, the forced convection heat transfer is generally enhanced while the nucleate boiling is suppressed, compared to pure forced convection and pool boiling respectively. Two factors were introduced in most of the correlations to indicate the enhancement and suppression effects. S.G. Kandikar [35] also developed a fluid-dependent parameter to account for the working fluid difference. However, only parameters of ten ordinary refrigeratants were provided. A boiling heat transfer correlation in a different form was also given by M. Xin et al.[77] and coworkers, which was based on their own experiments.

Even though the general correlations cover a large portion of the flow boiling heat transfer regime, experiments are still necessary to investigate the heat transfer characteristics of particular working fluids or special flow patterns. A. Niro [49] experimentally studied the transition zone between intermittent boiling and fully-developed boiling in a thermosyphon. N. Kattan et al. [36], R. Yun et al. [79; 80] and O. Zurcher et al. [86] studied the boiling characteristics of several working fluids including CO_2 and ammonia. The results indicated that the boiling heat transfer coefficient shows a

strong dependence on the heat flux values. According to R. Yun's [79; 80] study, the average heat transfer coefficient for CO_2 is 53% higher than that for R134a, which indicates that CO_2 is a very promising working fluid for thermosyphons.

2.4 Flow pattern

In thermosyphons, the countercurrent two-phase flow, coupled with heat transfer and pipe inclination, is another complex process to simulate. First of all, the flow pattern depends on many factors such as pipe geometry, flow rate, quality, local heat flux, inclination angle, etc. Most of the two phase flow studies that have been done are not specifically for thermosyphons. The best way to determine the flow pattern inside a thermosyphon is still empirical. W. Brigham [2] and M. Xin et al. [77] carried out an experimental study of the two phase flow inside a pipe, but no quantitative methods were given to determine the flow pattern. The only way to determine the two phase flow pattern is still through the use of flow pattern maps such as those described in Collier [12]. P. Terdtoon et al. [67; 66] also developed a simple flow pattern map under critical heat flux conditions. Most of the flow pattern maps have been developed for co-current flow, which is not the same as the countercurrent flow that takes place inside the thermosyphon. However, under most of the thermosyphon's working conditions, which are not close to the critical flow limitation, the flow pattern should be mostly annular in vertical thermosyphons and stratified in inclined thermosyphons. A wavy liquid surface and some drop entrainment are common when the working conditions approach the flow limit.

2.5 Working limits

As a high performance heat transfer device, the thermosyphon performance depends not only on outside conditions, but also on its interior limitations. Working limitation is another active thermosyphon research area. The working limitations related to a heat pipe generally include capillary limitations, sonic speed limitations, entrainment limitations, boiling (or condensation) limitations, and dry-out limitations. The most common of these for a thermosyphon are entrainment, boiling, and dry-out limitations.

Occurrences of these three limitations have strong parallels to small-break loss-of-coolant accidents in a pressurized water nuclear reactor, and thus some nuclear engineering research conclusions can also be applied to the study of thermosyphon limitations.

C. Busse [3] analytically studied the entrainment and sonic limitations of a wicked heat pipe by creating a one-dimensional model to predict the axial pressure gradient and the maximum heat flux at these limitations. M. El-Genk and H. Saber [16] built a one-dimensional model to predict the flooding limit in a two-phase thermosyphon. However, some of the assumptions involved in this model, such as the average vapor flow velocity equaling the liquid-vapor interface velocity, no entrainment, etc, can lead to large errors in the results. Y. Katto [37; 38] experimentally studied the critical heat flux of countercurrent boiling and built an analytical model to predict the critical heat flux. P. Terdtoon [67; 66] conducted an experimental study showing that the flooding limit is more likely to be reached in a long thermosyphon (L>>D), while in a short thermosyphon, the boiling limitation is more likely to be reached.

2.6 Inclination

Inclination is a very common factor in real thermosyphon applications, and can complicate thermosyphon modeling compared with vertical positioning. As in a vertical thermosyphon, the vapor and liquid flow can generally be considered one-dimensional because the thermosyphon length is typically much larger than the pipe diameter. In cylindrical coordinates, the radial flow can be considered negligible. In an inclined thermosyphon, however, the gravity is not parallel to the pipe axis and, circumferential flow occurs along the direction of gravity generating a three-dimensional flow. The incline also results in a concentrated condensate flow at the bottom of the pipe cross section and a thinner mean film thickness in the condenser, which helps to improve the heat transfer performance.

E. Hahne and U. Gross [25] studied the inclination angle experimentally and found the maximum performance of the thermosyphon occurred at 40-50 degrees from the vertical position. The authors did not explain why the experimental results indicated optimum performance at 40 to 50 degree tilt. This conclusion was also supported by P. Terdtoon and M. Shiraishi [65]. Based on experimental data from a copper-water thermosyphon, H. Nguyen-Chi and M. Groll [48] developed an empirical correlation to predict the maximum performance of an inclined thermosyphon. Another semi-empirical correlation was also developed by J. Wang and Y. Ma [74] to predict the performance of vertical and inclined thermosyphons. Based on several assumptions, Z. Zuo [85] proposed a numerical model to predict the influence of inclination on a thermosyphon's performance. Their results agreed fairly well with E. Hahne and U. Gross [25] and P. Terdtoon and M. Shiraishi's [65] experimental findings, and was also supported by S. Fiedler's and H. Auracher's [19] and S. Fiedler et al.'s [20] study of condensation heat transfer and flooding limits. Basically, almost all studies in the literature agree that a thermosyphon performs best at a 40 to 50 degree angle of inclination. However the heat transfer performance is not very sensitive to the angle of incline and, as long as the angle is not too large or too small, an incline will always greatly improve the performance of a thermosyphon.

2.7 Other aspects

Some other aspects of thermosyphon research cannot be covered by the above categories. Those topics are summarized below.

2.7.1 The aspect ratio

Generally speaking, the performance of a thermosyphon is not very sensitive to the aspect ratio (L/D) unless it is extremely large or small. At a very large aspect ratio, the thermosyphon is "long," and the vapor flow accumulated in the evaporator has to circulate through the relatively small-diameter orifice of the evaporator. With the same amount of condensate coming back from the condenser, the entrainment and flooding

limitation are more likely to be reached than others. In small aspect ratio setups, the situation is just the opposite, and the most probable working limitations stem from the heat transfer processes in the evaporator or condenser themselves, such as boiling and dry-out limitations. These conclusions are supported by modeling and experimental studies by B. Clements and Y. Lee [11] and P. Terdtoon et al. [67].

2.7.2 The charging ratio

The working fluid charging ratio is another consideration in the design and operation of thermosyphons. The particular influence of the charging ratio depends on the tilt angle of the thermosyphon. In a vertical position, the falling condensate film covers the evaporator wall; as long as the charge is large enough to prevent dry-out, the charging ratio has no major impact on the thermosyphon performance. In a tilted thermosyphon, the falling condensate only covers a small potion of the evaporator wall, and the heating surface greatly depends on the charging ratio. In such a case, a high charging ratio can generally result in high evaporator performance. M. El-Genk [17] studied the charging ratio influence with an analytical model, while Y. Park [53] studied it experimentally. Both of their studies showed a different working limit liability: at a large charging ratio, the entrainment limitation is more likely to come into play, while the dry-out limitation is more likely to be reached given a small charging ratio.

2.7.3 Gas loading

Non-condensable gases can interfere with thermosyphon performance by reducing the condensate heat transfer coefficient, especially when there is a small working temperature difference. The non-condensable gas might come from an incomplete vacuum, from leakage, or from a chemical reaction between non-compatible wall material and working fluid. Under a small working temperature difference, even a very small amount of non-condensable gases can concentrate on the condensation surface to lower the partial pressure of the working fluid vapor, resulting in a high driving temperature difference and a low condensate heat transfer coefficient. Under a high working temperature

difference, on the other hand, the vapor flow is strong enough to push the non-condensable gas to the far end of the condenser. In this case, only part of the condenser is disabled, and the rest of the condenser can still function, as enough working capacity is left. Modeling and experimental research by X. Zhou [83] and coworkers showed that the diffusion mechanism dominates under low power conditions, but under high power conditions, the performance of the thermosyphon is less stable and the practical interface region is much thicker than predicted by the diffusion mechanism. Based on an experiment with steam, K. Lee et al. [41] and coworkers developed a correlation to predict the influence of non-condensable gas on reflux condensation, including a degradation factor.

2.8 Reviews

In 1992, G.S.H. Lock [44] gave an extensive overview of the thermosyphon research in his book "The Tubular Thermosyphon - Variations on a Theme." He discussed almost all aspects of thermosyphon research in the book, which serves as a very good summary of the thermosyphon related-studies in the English-speaking world. In 1996, L.L. Vasiliev [72] reviewed the heat pipe research done in the former Soviet Union. However, his review focuses only on the application side, and does not summarize any modeling or theoretical research. In China, C. Tu [70] and C. Wu [75] reviewed the heat pipe research of the 1980's, and H. Zhang [81] reviewed the development and industrial application of heat pipe technology in China. The most noteworthy aspect of the heat pipe research was the solving of the incompatibility problem of steel and water. As a result, the low-cost steel-water heat pipe heat exchangers are now widely used in a variety of applications. However, the theoretical research into heat pipes continues to lag behind.

2.9 References

[1] AbuOrabi, M. (1998). "Modeling of heat transfer in dropwise condensation." International Journal of Heat and Mass Transfer **41**(1): 81-87.

[2] Brigham, W. E. (1957). "Two-phase concurrent flow of liquids and air through inclined pipe." The Pipeline Engineering: 39-42.

[3] Busse, C. A. (1973). "Theory of the ultimate heat transfer limit of cylindrical heat pipes." International Journal of Heat and Mass Transfer **16**(1): 169-176.

[4] Casarosa, C. (1988). "Experimental investigation and analytical modeling of a closed two-phase thermosyphon with imposed convection boundary conditions." International Journal of Heat and Mass Transfer **31**(9): 1815-1833.

[5] Chato, J. C. (1960). Laminar condensation inside horizontal and inclined tubes. Department of Mechanical Engineering, Massachusetts Institute of Technology (MIT). **Doctoral:** 203.

[6] Chato, J. C. (1962). "Laminar Condensation inside horizontal and inclined tubes." ASHRAE Journal: 52-60.

[7] Chen, J. C. (1966). "Correlation for Boiling Heat Transfer to Saturated Fluids in Convective Flow." Industrial & engineering chemistry process design and development **5**(3): 322-329.

[8] Chen, M. M. (1961). "An Analytical Study of Laminar Film Condensation: Part 1 -- Flat Plates." Journal of Heat Transfer (Transactions of the ASME) **83**: 48-54.

[9] Chen, S. J., J. G. Reed, et al. (1984). "Reflux condensation in a two-phase closed thermosyphon." International Journal of Heat and Mass Transfer **27**(9): 1587-1594.

[10] Chou, G. (1999). "A general modeling for heat transfer during reflux condensation inside vertical tubes surrounded by isothermal fluid." International Journal of Heat and Mass Transfer **42**(12): 2299-2311.

[11] Clements, B. and Y. Lee (1981). "Additional parameters in two-phase closed thermosyphons: Effects of tube diameter and wall thickness." International Journal of Heat and Mass Transfer **24**(9): 1554-1555.

[12] Collier, J. G. (1972). Convective Boiling and Condensation. London, McGraw-Hill.

[13] Dhir, V. and J. Lienhard (1971). "Laminar Film Condensation on Plane and Axisymmetric Bodies in Nonuniform Gravity." Journal of Heat Transfer (Transactions of the ASME): 97-100.

[14] Dobran, F. (1985). "Heat transfer in an Annular Two-Phase Flow." Journal of Heat Transfer (Transactions of the ASME) **107**: 472-476.

[15] Dobran, F. (1985). "Steady-state characteristics and stability thresholds of a closed two-phase thermosyphon." International Journal of Heat and Mass Transfer **28**(5): 949-957.

[16] EI-Genk, M. S. (1997). "Flooding limit in closed two-phase thermosyphons." International Journal of Heat and Mass Transfer **40**(9): 2147-2164.

[17] EI-Genk, M. S. (1999). "Determination of operation envelopes for closed two-phase thermosyphons." International Journal of Heat and Mass Transfer **42**(5): 889-903.

[18] Farsi, H. (2003). "An experimental and theoretical investigation of the transient behavior of a two-phase closed thermosyphon." Applied Thermal Engineering **23**(15): 1895-1912.

[19] Fiedler, S. and H. Auracher (2004). "Experimental and theoretical investigation of reflux condensation in an inclined small diameter tube." International Journal of Heat and Mass Transfer **47**(19-20): 4031-4043.

[20] Fiedler, S., H. Auracher, et al. (2002). "Effect of inclination on flooding and heat transfer during reflux condensation in a small diameter tube." International Communications in Heat and Mass Transfer **29**(3): 289-302.

[21] Ganzevles, F. L. A. and C. W. M. van der Geld (2004). "The effect of the angle of inclination of a condenser on the gas-to-plate heat resistance in dropwise condensation." Experimental Thermal and Fluid Science **28**(2-3): 237-241.

[22] Gross, U. (1992). "Reflux Condensation Heat-Transfer inside a Closed Thermosiphon." International Journal of Heat and Mass Transfer **35**(2): 279-294.

[23] Gungor, K. E. and R. H. S. Winterton (1986). "A General Correlation for Flow Boiling in Tubes and Annuli." International Journal of Heat and Mass Transfer **29**(3): 351-358.

[24] Gungor, K. E. and R. H. S. Winterton (1987). "Simplified General Correlation for Saturated Flow Boiling and Comparisons of Correlations with Data." Chemical Engineering Research & Design **65**(2): 148-156.

[25] Hahne, E. and U. Gross (1981). The influence of the inclination angle on the performance of a closed two-phase thermosyphon. 4th International heat pipe conference, UK.

[26] Harley, C. and A. Faghri (1994). "Complete Transient two-dimensional analysis of two-phase closed thermosyphons including the falling condensate film." Journal of Heat Transfer (Transactions of the ASME) **116**(2): 418-426.

[27] Hatamiya, S. and H. Tanaka (1987). "Dropwise Condensation of Steam at Low-Pressures." International Journal of Heat and Mass Transfer **30**(3): 497-507.

[28] Hosokawa, T. (1983). "Heat transfer in dropwise condensation on the upper surface of a horizontal tube." Heat Transfer Janpanses Res. **12**(4): 76-89.

[29] Hosokawa, T. (1987). "Dropwise condensation heat transfer on a vertical row of horizontal tubes." Journal of Heat Transfer (Transactions of the ASME) **81**: 111-117.

[30] Hosokawa, T., Y. Fujiwara, et al. (1995). "Heat-Transfer Characteristics of Dropwise Condensation on an Inclined Circular Tube." Heat Recovery Systems & Chp **15**(1): 31-39.

[31] Hosokawa, T., T. Kawai, et al. (1986). "Dropwise Condensation Heat-Transfer on a Horizontal Tube." Bulletin of the JSME-Japan Society of Mechanical Engineers **29**(254): 2570-2575.

[32] Jakob, M. (1936). "Heat transfer in evaporation and condensation - II." Mech. Engng **58**: 729-739.

[33] Kamminga, W. (1980). "An analytic solution of the film thickness of laminar film condensation on inclined pipes." International Journal of Heat and Mass Transfer **23**: 1291-1293.

[34] Kananeh, A. B., M. H. Rausch, et al. (2006). "Experimental study of dropwise condensation on plasma-ion implanted stainless steel tubes." International Journal of Heat and Mass Transfer **49**(25-26): 5018-5026.

[35] Kandlikar, S. G. (1990). "A General Correlation for Saturated 2-Phase Flow Boiling Heat-Transfer inside Horizontal and Vertical Tubes." Journal of Heat Transfer-Transactions of the ASME **112**(1): 219-228.

[36] Kattan, N., J. R. Thome, et al. (1998). "Flow boiling in horizontal tubes: Part 2 - New heat transfer data for five refrigerants." Journal of Heat Transfer-Transactions of the ASME **120**(1): 148-155.

[37] Katto, Y. (1991). "Critical heat flux of counter-flow boiling in a uniformly heated vertical tube with a closed bottom." International Journal of Heat and Mass Transfer **34**(4): 993-1001.

[38] Katto, Y. (1992). "An analytical study on the critical heat flux of countercurrent boiling in a vertical tube with a closed bottom." International Journal of Heat and Mass Transfer **35**(11): 3021-3028.

[39] Kuznetzov, G. V. and A. E. Sitnikov (2002). "Numerical analysis of basic regularities of heat and mass transfer in a high-temperature heat pipe." High temperature **40**(6): 898-904.

[40] Kuznetzov, G. V. and A. E. Sitnikov (2002). "Numerical modeling of heat and mass transfer in a low-temperature heat pipe." J of Engr Physics & Thermophysics **75**(4): 840-848.

[41] Lee, K. W., H. C. No, et al. (2006). "Local heat transfer during reflux condensation mode in a U-tube with and without noncondensible gases." International Journal of Heat and Mass Transfer **49**(11-12): 1813-1819.

[42] Lee, Y. and U. Mital (1972). "A Two-phase closed thermosyphon." International Journal of Heat and Mass Transfer **13**(9): 1695-1707.

[43] Liu, Z. and R. H. S. Winterton (1991). "A General Correlation for Saturated and Subcooled Flow Boiling in Tubes and Annuli, Based on a Nucleate Pool Boiling Equation." International Journal of Heat and Mass Transfer **34**(11): 2759-2766.

[44] Lock, G. S. H. (1992). The Tubular Thermosyphon ---- Variations on a Theme. Oxford, Oxford University Press.

[45] Long, E. L. (1962). The Long Thermopile. First International Permafrost Conference, Washington D.C., NRC Press.

[46] Long, E. L. (1965). Means for maintaining permafrost foundations. U. S. P. Office. U.S.A.: 7.

[47] Narain, A. (1997). "Interfacial shear models & their required asymptotic form for annular /stratified film condensation flows in inclined channels & vertical pipes." International Journal of Heat and Mass Transfer **40**(15): 3559-3575.

[48] Nguyen-Chi, H. and M. Groll (1981). Entrainment or Flooding Limit in A Closed Two-Phase Thermosyphon. 4th International Heat Pipe Conference, London, UK.

[49] Niro, A. (1990). "Boiling regimes in a closed two-phase thermosyphon." International Journal of Heat and Mass Transfer **33**(10): 2099-2110.

[50] Pan, Y. (2001). "Condensation heat transfer characteristics and concept of sub-flooding limit in a two-phase closed thermosyphon." International Communication of Heat and Mass Transfer **28**(3): 311-322.

[51] Park, C. Y. and P. S. Hrnjak (2005). "Flow boiling heat transfer of CO2 at low temperatures in a horizontal smooth tube." Journal of Heat Transfer-Transactions of the ASME **127**(12): 1305-1312.

[52] Park, C. Y. and P. S. Hrnjak (2007). "CO2 and R410A flow boiling heat transfer, pressure drop, and flow pattern at low temperatures in a horizontal smooth tube." International Journal of Refrigeration-Revue Internationale Du Froid **30**(1): 166-178.

[53] Park, Y. J. (2002). "Heat Transfer characteristics of a two-phase closed thermosyphon to the fill charge ratio." International Journal of Heat and Mass Transfer **45**(23): 4655-4661.

[54] Reed, J. G. (1985). Analytical modeling of two-phase closed thermosyphon. Department of Mechanical Engineering. Berkeley, University of California, Berkeley. **Ph.D.:** 145.

[55] Reed, J. G. (1987). "Modeling of the two-phase closed thermosyphon." Journal of Heat Transfer (Transactions of the ASME) **109**(3): 9.

[56] Rohsenow, W. M. (1956). "Heat transfer and temperature distribution in laminar film condensation." Journal of Heat Transfer (Transactions of the ASME) **78**: 1645-1648.

[57] Rose, J. W. (1966). A theory of heat transfer by dropwise condensation. The Third International Heat Transfer Conference, Am. Inst. Chem. Engrs.

[58] Rose, J. W. (1976). "Further aspects of dropwise condensation." International Journal of Heat and Mass Transfer **19**: 1363-1370.

[59] Rose, J. W. (1981). "Dropwise condensation theory." International Journal of Heat and Mass Transfer **24**(2): 191-194.

[60] Song, Y. J., D. Q. Xu, et al. (1991). "A Study on the Mechanism of Dropwise Condensation." International Journal of Heat and Mass Transfer **34**(11): 2827-2831.

[61] Sparrow, E. M. (1959). "A boundary layer treatment of laminar film condensation." Journal of Heat Transfer (Transactions of the ASME) **81**: 13-18.

[62] Spendel, T. (1981). Laminar Film condensation Heat Transfer in Closed Two-Phase Thermosyphons. 4th International Heat Pipe Conference, London, UK.

[63] Steiner, H., A. Kobor, et al. (2005). "A wall heat transfer model for subcooled boiling flow." International Journal of Heat and Mass Transfer **48**(19-20): 4161-4173.

[64] Tanasawa, I. (1991). Advances in condensation heat transfer, Elsevier.

[65] Terdtoon, P. and M. Shiraishi (1990). Investigation of effect of inclination angle on heat transfer characteristics of closed two-phase thermosyphon. 6th International Heat Pipe Conference, Minsk.

[66] Terdtoon, P., N. Waowaew, et al. (1999). "Internal flow patterns of an inclined closed two-phase thermosyphon at critical state: Case study II, effect of bond number." Experimental Heat Transfer **12**(4): 359-373.

[67] Terdtoon, P., N. Waowaew, et al. (1999). "Internal flow patterns of an inclined, closed two-phase thermosyphon at critical state: Case study I, effect of aspect ratio." Experimental Heat Transfer **12**(4): 347-358.

[68] Thome, J. R. and J. El Hajal (2004). "Flow boiling heat transfer to carbon dioxide: general prediction method." International Journal of Refrigeration-Revue Internationale Du Froid **27**(3): 294-301.

[69] Tien, C. L. and A. R. Rohani (1974). "Analysis of the effects of vapour pressure drop on heat pipe performance." International Journal of Heat and Mass Transfer **17**: 61-67.

[70] Tu, C. (1989). Thermosyphon heat exchanger and its application in waste heat recovery. Hangzhou, Zhejiang University Publishing House.

[71] Umur, A. and P. Griffith (1965). "Mechanism of dropwise condensation." Journal of Heat Transfer (Transactions of the ASME) **87**: 275-282.

[72] VasiLiev, L. L. (1998). "State-of-the art on heat pipe technology in the former Soviet Union." Applied Thermal Engineering **18**(7): 507-551.

[73] Vemuri, S. and K. J. Kim (2006). "An experimental and theoretical study on the concept of dropwise condensation." International Journal of Heat and Mass Transfer **49**(3-4): 649-657.

[74] Wang, J. C. Y. and Y. W. Ma (1991). "Condensation Heat-Transfer inside Vertical and Inclined Thermosiphons." Journal of Heat Transfer-Transactions of the ASME **113**(3): 777-780.

[75] Wu, C. (1993). Heat Pipe Application in Thermal Engineering. Beijing, Hydraulic and electric power publishing house.

[76] Wu, Y. T., C. X. Yang, et al. (2001). "Drop distributions and numerical simulation of dropwise condensation heat transfer." International Journal of Heat and Mass Transfer **44**(23): 4455-4464.

[77] Xin, M., G. Chen, et al. (1987). Flow and heat transfer in two-phase closed thermosyphons. 5th International Heat Pipe Conference. Grenoble.

[78] Xin, M. and J. Xia (1986). Heat Transfer by dropwise condensation in the two-phase closed thermosyphon. 8th Heat Transfer Conference. France.

[79] Yun, R., Y. Kim, et al. (2005). "Convective boiling heat transfer characteristics of CO2 in microchannels." International Journal of Heat and Mass Transfer **48**(2): 235-242.

[80] Yun, R., Y. C. Kim, et al. (2005). "Flow boiling heat transfer of carbon dioxide in horizontal mini tubes." International Journal of Heat and Fluid Flow **26**(5): 801-809.

[81] Zhang, H. (2003). "Research, development and industrial application of heat pipe technology in China." Applied Thermal Engineering **23**(9): 1067-1083.

[82] Zhang, W. Z., T. Hibiki, et al. (2005). "Correlation for flow boiling heat transfer at low liquid Reynolds number in small diameter channels." Journal of Heat Transfer-Transactions of the ASME **127**(11): 1214-1221.

[83] Zhou, X. (1995). "Condensation in a gas-loaded thermosyphon." International Journal of Heat and Mass Transfer **38**(9): 1905-1917.

[84] Zuo, Z. J. and F. Gunnerson (1994). "Numerical modeling of the steady-state two-phase closed thermosyphon." International Journal of Heat and Mass Transfer **37**(17): 2715-2722.

[85] Zuo, Z. J. and F. Gunnerson (1995). "Heat transfer analysis of an inclined two-phase closed thermosyphon." Journal of Heat Transfer (Transactions of the ASME) **117**(4): 1073-1075.

[86] Zurcher, O., J. R. Thome, et al. (1999). "Evaporation of ammonia in a smooth horizontal tube: Heat transfer measurements and predictions." Journal of Heat Transfer-Transactions of the ASME **121**(1): 89-101.

Chapter 3 Experimental work

Two experiments were carried out related to the current research. One was a laboratory experiment to investigate the carbon dioxide condensation heat transfer characteristics inside a tubular condenser and the other was a full-scale heat transfer performance test of the hairpin thermosyphons, in which the thermosyphons were installed in an actual roadway project.

The laboratory experiment was designed with the guidance and help of Dr. Douglas J. Goering. Construction and assembly of the experimental condenser was completed with the help of Mr. Ed Yarmak (Arctic Foundation Inc.) and Mr. Eric Johansen. The test was assembled and conducted in the heat transfer laboratory of the Department of Mechanical Engineering at the University of Alaska Fairbanks.

The full scale field test of hairpin thermosyphon was part of a new road project, now referred to as Thompson Drive near Fairbanks. The initial proposal regarding the inclusion of hairpin thermosyphon design feature was the result of the conversations between Billy Connor, Douglas Goering, John Zarling, Steve Saboundjian, and Malcolm Pearson [4]. The analysis of the thermosyphon performance, which lead to the final design of hairpin thermosyphon system, was carried out by Dr. John Zarling. The details are available in Dr. Goering's reports [4; 5]. My role in this field test was to collect the data from roadway test sites in order to characterize the performance of these thermosyphons.

3.1 Laboratory Experiment

In the research that has been reported in the prior literatures fully developed condensation has been shown to transfer a high heat flux with a small temperature difference. The condensation heat transfer coefficients are on the order of 10^3 to 10^4 W/m^2K. A number of experimental correlations are available to predict the heat transfer performance,

and theoretical solutions are also available for some cases of film condensation. However in the current study, the condensation occurs under extremely small heat flux conditions. This condensation heat transfer lies outside of the range that can be predicted by most of the previous correlations or theories. The heat transfer mechanism of the condensation studied in the current work is likely different from that of fully developed condensation. Therefore, a lab experiment was designed to determine condensation heat transfer coefficients applicable for small heat flux conditions.

3.1.1 Experimental Facility

A schematic of the experiment rig is shown in Figure 3.1. The main component of this experimental facility is a working thermosyphon with evaporator, adiabatic section, and condenser. A CO_2 tank, a vacuum system, a coolant supply system and a heating system are appended to the main system to allow operation of the thermosyphon in the desired fashion. The thermosyphon condenser is the test section in this experiment. Most of the sensors are attached to the test section to monitor the heat transfer performance.

3.1.1.1 Test section

The test section consists of a short piece of standard schedule 40 3-inch (76.2 mm) diameter steel pipe, shown as part No.1 in Figure 3.1. It has an inner diameter of 78 mm and an average wall thickness of 5.5 mm. The same pipe is used as the condenser in the full scale road test, which will be introduced shortly. The only difference is the length of the condenser. In the full scale road test, the condenser is more than 10 meters long, while in this lab experiment, the test section is only 610 mm in length. At one end of the test section, a sight glass assembly, with a piece of "Metaglass" (part No. 3) and two ASME standard flanges, is welded on to allow visual inspection of the condensation process and condensate flow inside the test section. An Light Emitting Diode (LED) bulb (part No. 4) is set up inside the test section to provide lighting. The test section is mechanically supported by a base with which the incline angle of the test section can be adjusted.

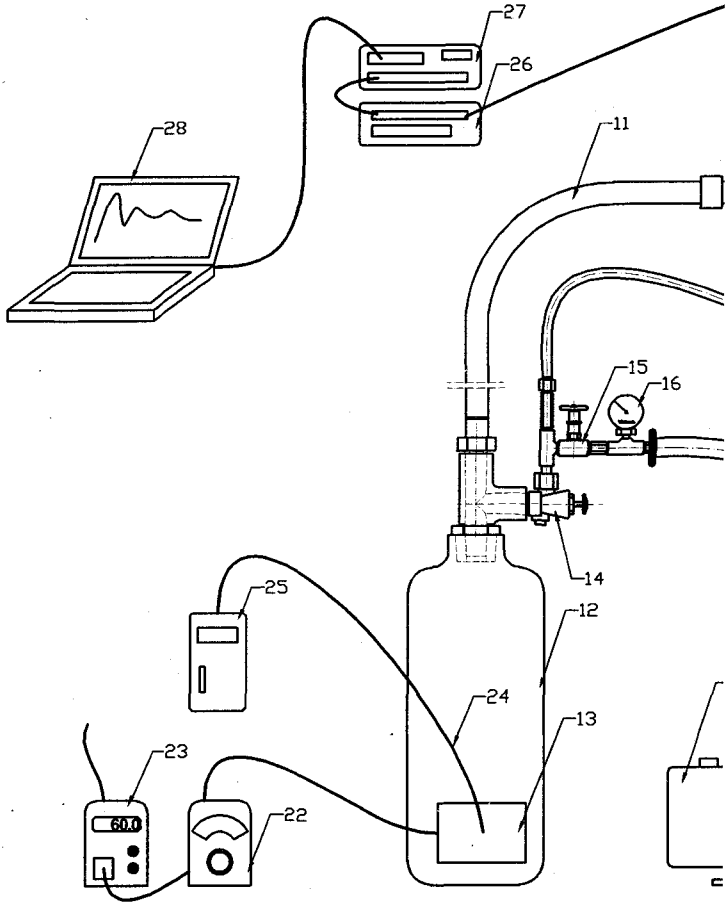

Figure 3.1 Lab experiment setup.

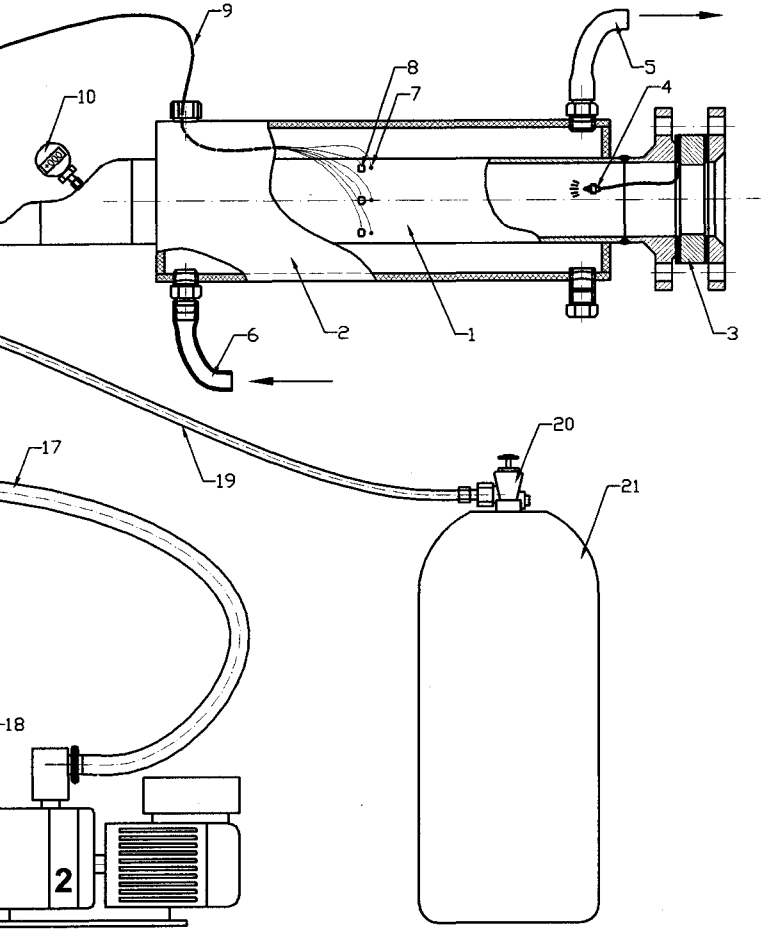
9
10
8
7
5
4
6
2
1
3
17
19
20
21
18
2

3.1.1.2 Adiabatic section

The adiabatic section (part No. 11) provides the connection between the condenser and the evaporator. It is constructed from 3/4-inch (19.0 mm) diameter soft copper tubing. This type "K" copper tube has an inside diameter of 19.0 mm and an average wall thickness of 1.65 mm. The overall length of the adiabatic section is 1400 mm. It is connected to the condenser with two welded eccentric reducers. On the other end, it is connected to a 3/4-inch diameter (19 mm) tee and the evaporator with a Swagelok fitting. The adiabatic section and all connections are insulated with pipe insulation and foam wrap.

3.1.1.3 Evaporator

The evaporator (part No. 12) is constructed from a 15 lb CO_2 fire extinguisher bottle. To provide a large orifice for vapor and condensate flow, the original CGA320 valve is removed and replaced with a bushing and a 3/4-inch (19.0 mm) diameter tee, which is connected to the adiabatic section. Spray foam insulation is applied to the outside of the evaporator and the heating pad to limit the heat loss in this section.

3.1.1.4 CO_2 tank

The CO_2 tank (part No. 21) is a 50 lb CO_2 cylinder with a standard CGA320 valve on top. It is connected to the system by a soft CO_2 hose (part No. 19). This CO_2 tank is the supplier of the working fluid for the system. It is only used in the preparation stage of the experiment. Once the system is adequately evacuated and charged with enough CO_2, the tank will be cut off from the working system by a CGA320 valve (part No. 14).

3.1.1.5 Vacuum system

The vacuum system is constructed of a vacuum pump (part No. 18), a soft vacuum hose (part No. 17), a vacuum gauge (part No. 16) and a needle valve (part No. 15). The two-stage "Edwards" vacuum pump can provide an ultimate vacuum of 2.5×10^{-2} Pa. It can be attached and removed from the main system by a quick flange fitting connecting the

pressure gauge and the soft vacuum hose, which provides some convenience in repeatedly charging, purging and evacuating the system to achieve a high purification of working fluid in the main system. When the system reached an adequate vacuum, the vacuum system was also cut off from the main system by the needle valve.

3.1.1.6 Coolant supply system

The coolant supply system consists of a Forma Scientific Model 2425 temperature controlled bath, a cooling jacket (part No. 2) outside the test section, and connection tubing. The temperature control system, which is not shown in Figure 3.1, has a thermostatic coolant bath, whose temperature can be set and controlled automatically. 1/2-inch (12.7 mm) rubber tubes with insulation outside are used to connect the temperature control system and the coolant jacket. The coolant jacket outside the test section is made of a section of 6-inch diameter (152.4 mm) PVC pipe with rubber caps on both ends. Connections to the coolant circulating tubes are made on the highest and lowest part of the jacket with barb fittings. The coolant is a 1:1 mixture of ethylene glycol and water. A circulating pump in the temperature control system provides the power to circulate coolant in the system.

3.1.1.7 Heating system

The heat input to the system was supplied by a heating pad (part No. 13) attached outside the lower part of the evaporator. The power supply was controlled by a VariAC (part No. 22) and monitored with a "WattsUp Pro" power meter (part No. 23). To avoid melting the insulation layer, a type "K" thermocouple (part No. 24) was installed directly on the outer surface of the heating pad and hooked up with an "Omega" digital thermometer to monitor the temperature.

3.1.2 Measurements and instrumentation

3.1.2.1 Vapor pressure

The vapor pressure in the condenser is measured with an Omega DPG-5000 digital pressure gauge (part No. 10) with a 0~2 volt analog output. The accuracy of this gauge is 0.25% of its full 1000-psi scale. It is installed into a 1/4-inch (6.35 mm) diameter pipe thread on the eccentric reducer at the entrance of the condenser. Assuming equilibrium saturation conditions in the condenser, the vapor temperature can be calculated from the saturation pressure. According to the relationship between the saturation pressure and temperature, the saturation temperature can be calculated from the pressure measurement with an accuracy of ± 0.1 C°. A sample calculation is given below for a temperature near the freezing point. The saturation temperature and pressure relations are given as:

0 °C ~ 505.239 psi (3.1)

1 °C ~ 518.930 psi (3.2)

A temperature difference of ±1 °C corresponds to a pressure difference of ±13.7 psi. At the 0.25% pressure gage accuracy, the highest error in pressure measurement in this pressure range is about ±2.5 psi, therefore, the accuracy of temperature calculation from the pressure measurement is $\pm\frac{2.5psi}{13.7psi}\times 1^{o}C = \pm 0.19^{o}C < \pm 0.2^{o}C$.

3.1.2.2 Wall temperature

Wall temperatures are measured by Omega SA1 4-wire surface mount RTD sensors (part No. 7). They have a 100 Ohm nominal resistance at 0 °C and ±0.06% accuracy. In the range of the current experiment, the accuracy is within ±0.08% . Three RTD sensors are installed in the middle of the test section. As shown in Figure 3.2, they are located on the top, side, and bottom potion of the pipe wall. They are numbered #1, #2 and #3 RTD sensors respectively and record the temperature around the pipe wall. Epoxy glue and clamps were used during the installation to guarantee a good thermal contact. The thermal resistance of the pipe wall is considered in calculating the inner wall temperature from the temperature measurements made at the outside surface.

3.1.2.3 Heat flux

The test section was instrumented with heat flux sensors as well. The sensors were "Omega" HFS-4 thin film heat flux sensors (part No. 8 in Figure 3.1) with a nominal sensitivity of 2.1 $\frac{\mu V}{W/m^2}$. The sensor itself is about 0.25 mm in thickness and has a thermal resistance of 0.0018 $\frac{m^2 K}{W}$. This resistance is compensated for in the data processing to get the real heat flux through an undisturbed pipe wall. Three heat flux sensors are installed on the top, side, and bottom of the pipe, right beside the RTD sensors as shown in Figure 3.2. The heat flux sensors are bonded to the pipe wall with Epoxy glue. Clamps and plastic foam were used during the installation to ensure a very thin and even glue film.

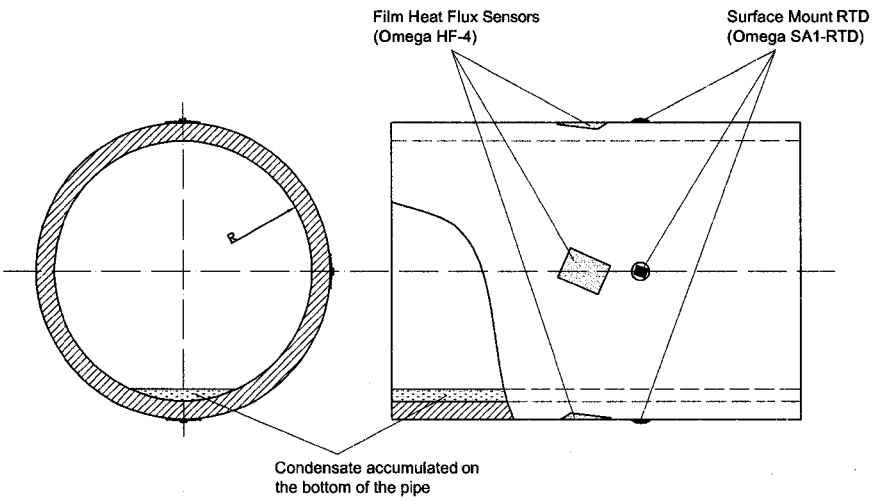

Figure 3.2 Sensor location on the condenser pipe wall.

3.1.2.4 Data logging system

All sensor wires are combined in a single bundle and passed through a fitting in the PVC jacket wall with silicon gel sealant. The temperature sensors, heat flux sensors and the analog output of the pressure gauge are all hooked up to a data logging system which

consists of a Campbell CR10X data logger (part No. 27) and a Campbell AM16/32A multiplexer (part No. 26).

The multiplexer is running in a 4×16 mode to enable the four wire half bridge measurements from the RTD sensors. The four wire half bridge wiring of RTD sensors is shown in Figure 3.3. Two analog channels and two resistors are required in this bridge. "Vx" in Figure 3.3 is the excitation of this half bridge. R1 is a current limiting resistor with a nominal resistance of 10 $k\Omega$. The completion resistor, R2, is a VISHAY PTF-56 precision metal film resistor with a nominal resistance of 100 Ω, an accuracy of $\pm0.1\%$, and a temperature coefficient of ±10 $ppm/^{o}C$. The accuracy of this 4-wire half bridge measurement is $\pm0.02\%$.

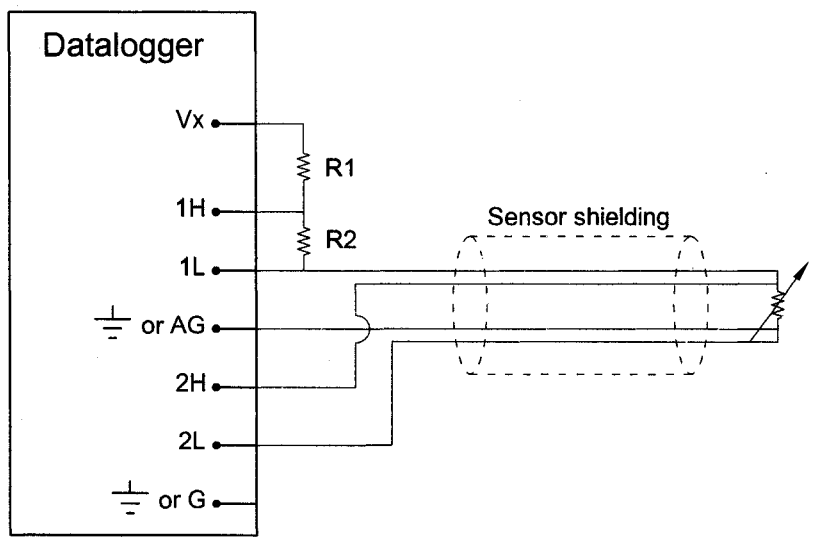

Figure 3.3 Surface mount RTD sensor wiring [1].

The heat flux sensors are hooked up directly to analog input differential channels on the multiplexer. The heat flux sensor channels are running in a "Auto 60Hz Rejection Range" mode, which has a resolution of 0.33 μV, and an accuracy of $\pm10\%$.

The output from the pressure gauge is also connected to the analog input differential channel on the multiplexer. This channel is running in a "2500 mV Slow Range" mode, which has a resolution of 333 μV, and an accuracy of ±0.05%.

The datalogger is programmed to sample data every 20 seconds and record data to a final storage area every 60 seconds. The program of the Campbell data logger is available in the appendix. A Compaq Armada E500 laptop computer is connected to the datalogger with an RS-232 cable. LoggerNet, a software package provided by Campbell Scientific, is used to monitor the real time data on the screen. Experimental data acquired from all the sensors is stored in the data logger during the experiment. When a balanced equilibrium situation is achieved, it is downloaded to the computer for later processing.

3.1.3 Procedure

Before the installation, all parts were cleaned. The main system was tested with a liquid Nitrogen bottle and regulators at the pressure of 1000 psi (6894.76 kPa). No leakage or pressure loss was observed over a period of 24 hours.

Before the experiment began, the thermosyphon system was evacuated through the needle valve (part No. 15 in Figure 3.1). To ensure a low concentration of non-condensable gas, the system was repeatedly charged with CO_2 and evacuated. This procedure was repeated 10 times to dilute and remove any non-condensable gases in the main system. The highest vacuum indicated by the vacuum gauge (part No. 16) was around 2.25 kPa. After five rounds of charging, purging, and evacuating, the final partial pressure of non-condensable gases in the system is lower than 0.0025 Pa (0.02 mTorr).

After the evacuation and purge cycles were completed, about five liters of liquid CO_2 (weighing about 4.8 kg) were charged into the system. Then valve 14 in Figure 3.1 is shut off to isolate the thermosyphon system from the vacuum system and the CO_2 tank.

The operation of the thermosyphon is initiated by activating the evaporator heating power and pumping coolant through the condenser cooling jacket. Steady-state operation of the device can be achieved in about 4 to 8 hours. When all sensor readings stop changing and remain stable for half an hour, the operation is regarded as steady-sate. Once the steady-state is achieved, the collected data are downloaded from the datalogger to the computer. Then the power input to the evaporator or the coolant temperature is adjusted and another 4 to 8 hours wait is required to re-establish the steady-state operation at another operating point.

3.1.4 Data processing

After steady state operation is achieved, small fluctuations in the data are eliminated by averaging the data over the last ten minutes of the steady-state operation. Equation (3.3) was used in the calculation of the condensation heat transfer coefficient, in which inner wall temperature, $T_{w,i}$, vapor temperature, T_v and heat flux, q, are needed.

$$h_c = \frac{q}{T_v - T_{w,i}} \tag{3.3}$$

The inner wall temperature is measured using the RTD sensors mounted on the outer pipe surface, the vapor temperature is measured from the vapor pressure using the saturation assumption, and the heat flux through the pipe wall is measured directly by the heat flux sensors. The heat flux values are influenced by the thermal resistance of the heat flux sensor itself. Before using the temperature and heat flux data in the actual calculations, corrections are made to the measurements to account for these factors and improve the accuracy of the heat transfer coefficient results.

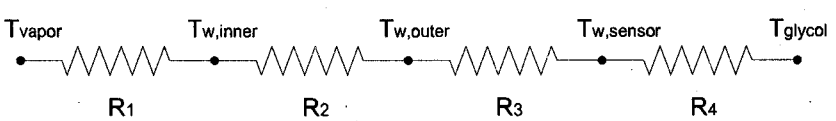

Figure 3.4 Thermal resistances through the thin film heat flux sensor.

As shown in Figure 3.4, the heat transfer process from the CO_2 vapor to the circulating glycol is mainly constrained by four thermal resistances: the resistance from CO_2 vapor to the pipe wall (R_1), the resistance from the inner wall to outer wall (R_2), the resistance of conduction through the heat flux sensor (R_3), and the resistance from the sensor surface to the glycol (R_4). During the installation of the heat flux sensors, the sensor was clamped against the pipe wall with a foam block. The epoxy glue is very thin and the thermal resistance of this epoxy glue layer is considered negligible. The glycol circulation was held at a constant flow rate that was measured to be $4.55\times10^{-5}\ m^3/s$. Within the test section, the glycol flows through an annular space with a cross sectional area of 0.012 m^2. Using the constant properties of glycol at 0 °C, the Reynolds number based on the hydraulic diameter is about 16. This is well within the laminar flow range, in which, the heat transfer is independent of the flow rate with constant Nusselt number of 6.18 characterizing the heat transfer process [6; 9]. Assuming steady-state operation, constant working fluid properties, and a constant condensation heat transfer coefficient of 200 $W/(m^2K)$ (a typical value calculated based on later calculations), the thermal resistances (based on the inner area of the condenser pipe) from the CO_2 vapor to the circulating glycol can all be estimated.

From CO_2 vapor to inner pipe wall:

$$R_1 = \frac{1}{200} = 5\times10^{-3}\left(\frac{m^2K}{W}\right) \tag{3.4}$$

From inner wall to outer wall:

$$R_2 = \frac{\ln(D_o/D_i)\cdot D_i}{2\cdot k} = \frac{\ln(0.089/0.078)\times0.078}{2\times45} = 1.14\times10^{-4}\left(\frac{m^2K}{W}\right) \tag{3.5}$$

Through the heat flux sensor [7]:

$$R_3 = 1.76\times10^{-3}\frac{D_i}{D_o} = 1.76\times10^{-3}\times\frac{0.078}{0.089} = 1.54\times10^{-3}\left(\frac{m^2K}{W}\right) \tag{3.6}$$

From the sensor surface to glycol:

$$R_4 = \frac{1}{h}\frac{D_i}{D_o} = 4.04\times10^{-2}\times\frac{0.078}{0.089} = 3.54\times10^{-2}\left(\frac{m^2K}{W}\right) \quad (3.7)$$

According to this estimation, the thermal resistance of the heat flux sensor itself will result in an error of -3.7% in the overall heat flux measurement. This can be easily compensated for during data processing.

For the wall temperature, the thermal resistance of the pipe wall is about 2.4% of the overall value from the vapor temperature to the outside pipe wall temperature. This will result in a -2.4% temperature error over the temperature difference from the vapor to the outside wall. This error can also be corrected based on the corrected heat flux reading and the thermal resistance of the pipe wall.

The saturation temperature of CO_2 vapor is calculated from the CO_2 vapor pressure based on the assumption of saturated conditions. The relationship between the saturation temperature and pressure is obtained from a CO_2 thermophysical properties table [3]. As discussed before, the accuracy of saturation temperature calculated from pressure measurement is ± 0.2 C°, which is of the same order as the RTD sensor's accuracy.

3.1.5 Results and Discussion

In this experiment, the coolant temperature ranged from 0 °C to 16 °C. The power input in the evaporator ranged from 10W to 60W in steps of 10W. Thirty six sets of data were eventually obtained from the experiment.

The condensation processes were observed through the sight glass. Before the experiment, the condenser wall was dry and there was no liquid pooled in the bottom of the condenser test section. Once the experiment started, the wall was gradually wetted by CO_2 condensate which flowed down along the wall and formed a liquid back flow stream on the bottom of the condenser pipe. The condensate film was very thin and no droplets

could be observed on the wall during any of the experimental runs. The surface of the condensate stream at the bottom of the condenser was very smooth even at the outlet of the condenser.

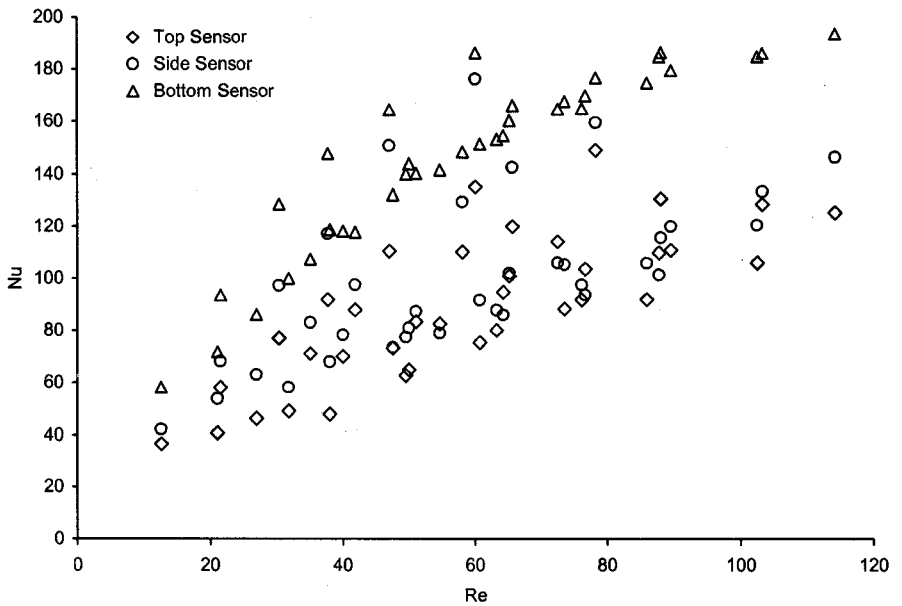

Figure 3.5 Nusselt number vs. vapor Reynolds number for all 36 experimental conditions.

The entire body of data collected from the steady state experiments is shown in Figure 3.5. The Nusselt number ($Nu = \frac{hD}{k_v}$) and vapor Reynolds number ($Re = \frac{V_v D}{\upsilon_v}$) are both defined based on the inner diameter of the condenser pipe. The fluid properties are calculated at saturation temperature. The characteristic velocity in Reynolds number is calculated from the energy and mass balance in the upper half condenser based on a uniform heat flux assumption. The variation of Nusselt number at the same Reynolds number is due to the different coolant temperatures at different operating conditions.

Because of the extremely low heat flux, the condensation in this experiment was quite different from the fully developed condensation found in most industrial applications that can be predicted by Nusselt's theory or existing empirical correlations. The measured

condensation heat transfer coefficient is much lower than the prediction of Nusselt theory. As can be seen in Figure 3.5, the Nusselt number data are quite scattered when plotted as a function of Reynolds number. However, for all three locations along the pipe cross section, it appears that a higher Reynolds number indicates a higher heat transfer coefficient. This is also different from Nusselt's prediction, in which a higher film Reynolds number indicates a lower heat transfer coefficient.

There are several effects which may account for the low heat transfer coefficient and an opposite trend as compared to the Nusselt prediction. First, the condensation in this study is not fully developed. It is in a transitional regime from single phase forced convection to condensation. The thermal resistance of the heat conduction through the thin condensate film, which is taken as the main resistance in the Nusselt solution, may not be dominant in the overall resistance chain. For these experiments the thermal resistance of convection in the vapor phase is of the same order and cannot be neglected. As a result, the vapor Reynolds number can still have an impact on the heat transfer characteristics as in the case of forced convection problems.

A second factor, which may contribute to the low heat transfer readings, is the extremely low heat flux. Because of the low overall heat flux, the vapor flow in the condenser is slow and the Reynolds numbers based on the pipe diameter are typically smaller than 200. The vapor flow in the condenser is laminar. This results in a higher thermal resistance than the turbulent vapor flow found in most of the industrial condensers. On the other hand, the small heat flux is also the reason for a small condensate mass flux flowing along the pipe wall, this also results in a very thin condensate film.

A third factor contributing to the low condensation heat transfer coefficient is the low latent heat of CO_2. Compared with other refrigerants commonly used in the refrigeration industry, CO_2 has a relatively low critical temperature of 31.06 °C (73.8 bar), so that the CO_2 latent heat near the experimental conditions (coolant temperature ranged from 0 °C

to 16 °C) is relatively small. At 10 °C, for example, the CO_2 latent heat is about 197 kJ/kg, which is more than 10 times smaller than the latent heat of water (about 2477 kJ/kg) at the same temperature.

In addition to low condensation rates, another factor that helps reduce the film thickness is the CO_2 viscosity and surface tension. At 10 °C, CO_2 liquid has a dynamic viscosity of 83 $\mu Pa \cdot S$, and a surface tension of 0.0028 N/m. While water has a viscosity of 1300 $\mu Pa \cdot S$, and a surface tension of 0.074 N/m. Extremely low viscosity and surface tension reduce the resistance of condensate flow and the film thickness as well.

Another possible explanation is the pressure drop in the condenser. The vapor pressure measurement is taken at the entrance of the condenser. When vapor flow travels deep into the condenser, the pressure should drop slightly both because of the friction and the condensation. The lower vapor pressure would result in a lower saturation temperature, a lower overall temperature difference. As a result of the assumption of uniform saturation pressure and temperature in the condenser, an artificially low heat transfer coefficient results. However, because of the extremely low vapor velocity and the small inclination angle of the condenser, a typical pressure difference over the entire condenser is about 20 Pa, which corresponds to a very small saturation temperature difference of 2.3×10^{-4} C°. Therefore, the neglecting of the pressure drop in the condenser is well justified.

All these effects discussed above working together result in two major findings: the assumption of dominant film conduction resistance used in Nusselt theory is not valid, and very low condensation heat transfer coefficients result at the reduced heat transfer rates investigated here.

To eliminate the influence of the location along the pipe cross section and generalize the experimental results for later applications, the average condensation heat transfer

coefficient (average Nusselt number) is plotted against the Reynolds number, Jakob number and Prandtl number.

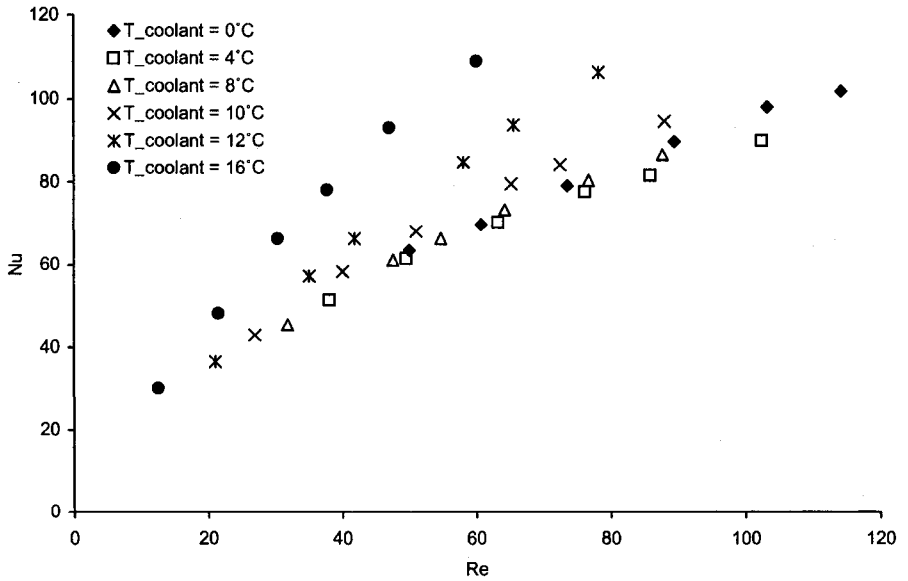

Figure 3.6 Variation of Nusselt number with vapor Reynolds number for different coolant temperatures.

As shown in Figure 3.6, the mean Nusselt number maintains a fairly linear relation with the vapor Reynolds number at different working conditions. The coolant temperature has a positive effect on the heat transfer coefficient. At higher coolant temperature, the working temperature of CO_2 liquid and vapor is also higher. The shift in working fluid properties might be responsible for the heat transfer enhancement because the vapor thermal conductivity increases rapidly when the temperature increases. Another obvious effect that can be observed from Figure 3.6 is that the nearly linear relations between the Reynolds number and Nusselt number do not go through the origin. At zero Reynolds number, a positive Nusselt number remains. This indicates that some other heat transfer mechanism other than vapor convection exist, which in this case, is the contribution due to condensation heat transfer.

Based on the preliminary analysis, both the condensation and the convection mechanism should be considered in the correlation, in this transition stage from forced convection to fully developed condensation. A weighted superposition method, introduced by J.C. Chen [2] and utilized by many later researchers for convective boiling, is adapted to describe this convective condensation. As shown in Equation (3.8), the heat transfer contributed by the convective mechanism and by the condensation mechanism are considered additive.

$$Nu = \alpha Re_v^a \, \mathrm{Pr}_v^b + \beta Ra^c Ja^d \tag{3.8}$$

For both terms, an exponential form is proposed as in most of the other forced convection and condensation correlations. Reynolds number and Prandtl ($Pr_v = \frac{\upsilon_v}{\alpha_v}$) number are selected to construct the convective term, while Rayleigh number and Jacob number are selected for the condensation term. The selection of weight factors and indices is based on a combination of iterations and least square regression to ensure a good fit and physical meaning. The final correlation is given in Equation (3.9).

$$Nu = 0.642 Re_v^{0.867} \, \mathrm{Pr}_v^{1.729} + 0.0133 Ra^{0.0298} Ja^{-1.795} \tag{3.9}$$

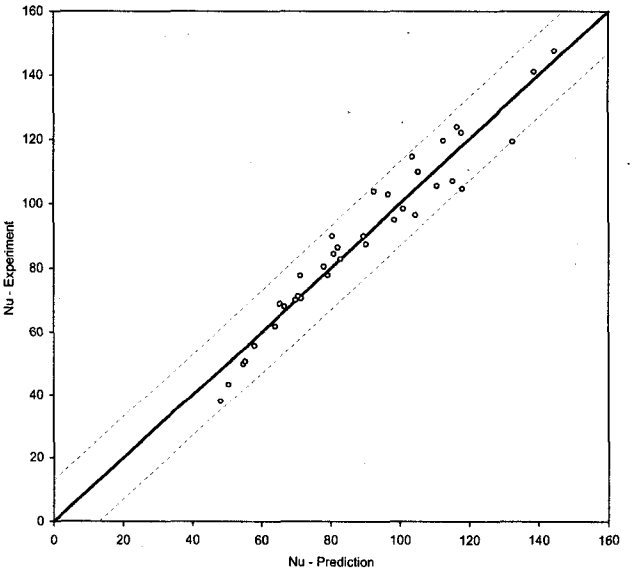

Figure 3.7 Correlation prediction vs. experimental data.

The correlation prediction is plotted against the experimental data in Figure 3.7. The average prediction error is around 5%. The highest error occurs at the lower Nusselt number end, where the temperature difference approaches the instrument accuracy limits. Because of the potential possibility of variation in the heat transfer mechanism, this correlation is only valid for CO_2 condensation in the range of the current experiment in which the highest heat flux is about 250 W/m^2, the accuracy of this correlation outside this range or for other working fluids cannot be guaranteed.

3.2 Full Scale Test

3.2.1 Introduction

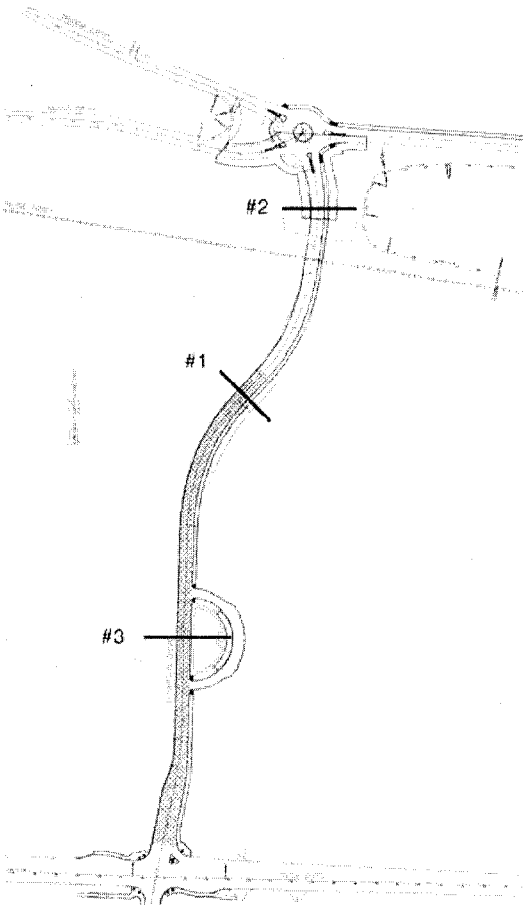

Figure 3.8 The Thompson Drive project.

As discussed in Chapter 1, a full scale performance test on the hairpin thermosyphon was carried out as a part of the Thompson Drive project, which is near the University of Alaska Fairbanks campus. This road project crosses a previously undisturbed area of warm permafrost to provide a southern entrance to UAF main campus. Thompson Drive is about one kilometer long, and the embankment height changes from less than 1 meter at the south end to about 10 meters at the north end, where the road passes over railroad tracks.

Varying embankment height in different areas of the project motivated the use of different configurations of passive cooling systems. Hairpin thermosyphons were utilized in the wooded area south of the railroad tracks, located near test section #1 and #3 as shown in Figure 3.8. A 10cm thick horizontal insulation sheet was used in the core of the embankment beneath the thermosyphon condensers in order to limit the amount of heat entry into the embankment during summer. During winter heat is transported around this insulation and out of the embankment by the hairpin thermosyphons.

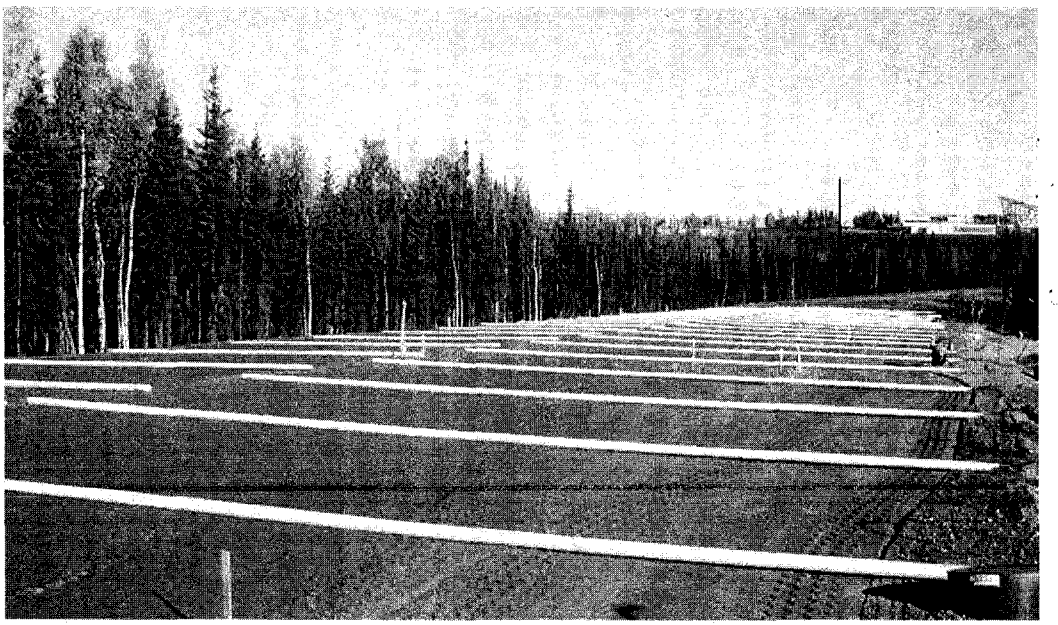

Figure 3.9 Hairpin thermosyphon condensers during installation.

Figure 3.9 shows the thermosyphon condenser pipes during the construction of the roadway. The condensers were then covered with a thin layer of aggregate and pavement, resulting in a system where the condensers were located approximately 30 cm beneath the paved surface. As shown in Figure 3.9, the hairpin thermosyphons extend inward from each edge of the roadway embankment in a left-right staggered pattern. A 5 m spacing is used between thermosyphons along the direction of the roadway for each side, resulting in a 2.5 m staggered pattern.

3.2.2 Instrumentation

To record the thermal performance of the passive cooling system, the test sections were instrumented with thermistor probes to monitor temperature variations over time. The probes were installed in the natural ground beneath the embankment and on the condenser and evaporator pipes of one of the thermosyphons. In addition to the temperature sensors, six heat flux sensors where installed on the thermosyphon, three of them on the condenser and three on the evaporator.

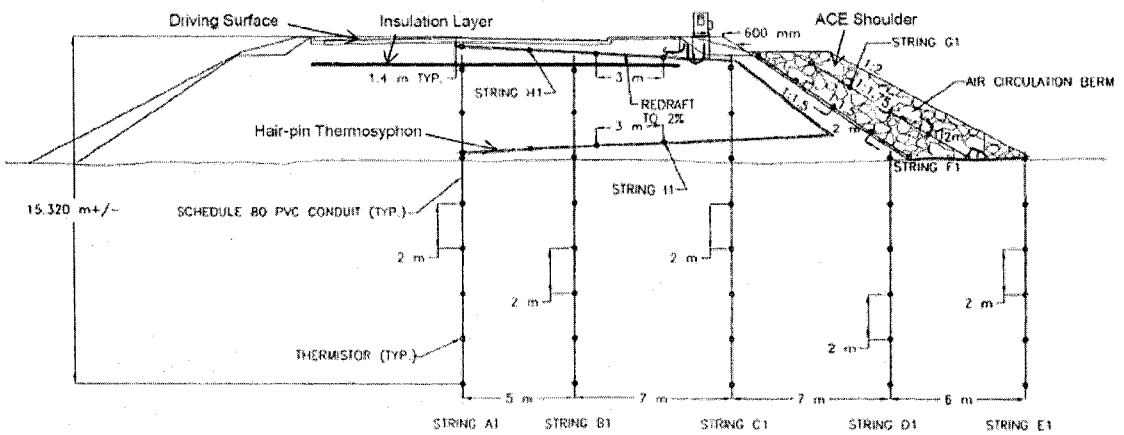

Figure 3.10 Test section #1.

Figure 3.10 is a scale drawing of the test section #1, including the location of the hairpin thermosyphon, the insulation layer and the thermistor sensor layout for this test section. A total of nine separate thermistor strings (labeled A1-I1) are included in this diagram.

String H1 and I1 are fastened directly to the evaporator and condenser pipes of the thermosyphon. The remaining strings are installed in sealed PVC tubes. All the instrumentation strings are run to the side of the embankment, where they are connected to the data logging system. For this test section, the nine thermistor strings contain a total of 54 thermistor sensors. Though the position of the thermosyphon is shown in Figure 3.10, the thermosyphons are not in fact located in the same plane as the rest of the temperature strings. Due to the thermosyphon staggering described above, the thermosyphons are actually located 2.5 m away from the instrumented section (both in and out of the plane of the Figure 3.10).

Figure 3.11 is a scale drawing of the test section #3, including the location of the hairpin thermosyphon, the insulation layer and the thermistor sensor layout for this test section. A total of seven separate thermistor strings (labeled A3-G3) are included in this test section (string G3 is not shown in Figure 3.11). String D3 and E3 are fastened directly to the evaporator and condenser pipes of the thermosyphon. The remaining strings are installed in sealed PVC tubes. For this test section, the seven thermistor strings contain a total of 39 thermistor sensors.

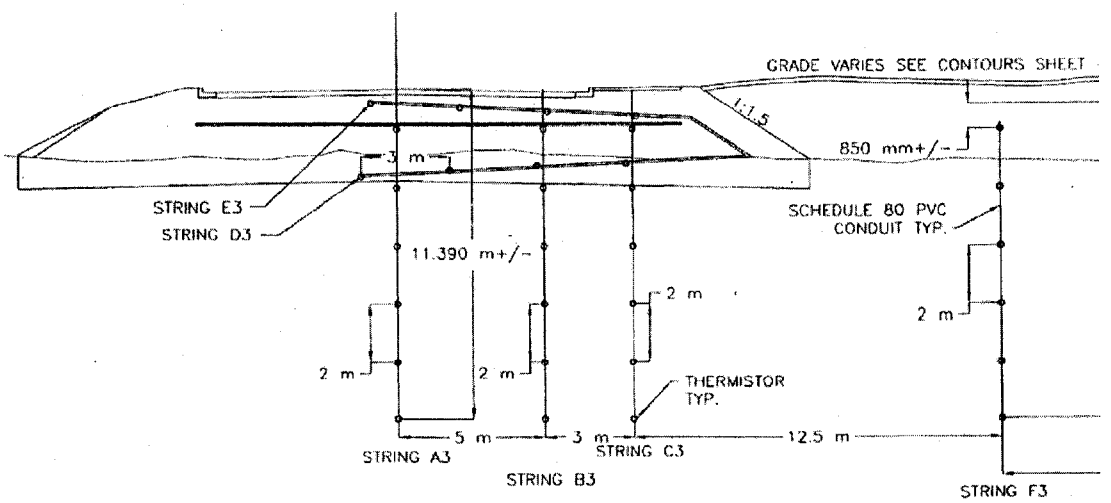

Figure 3.11 Test section #3.

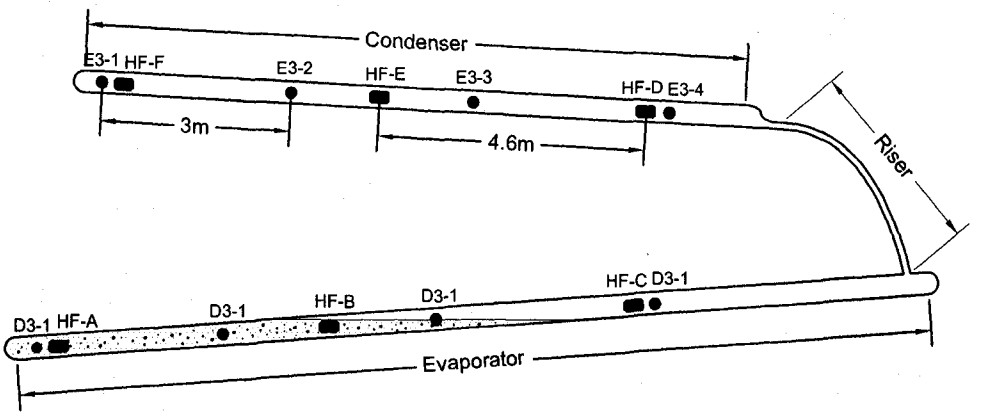

Figure 3.12 Sensor layout on the hairpin thermosyphon.

Besides the temperature sensors, six thin film heat flux sensors (HF-A to HF-F) are installed on the evaporator and condenser pipe of the thermosyphon to monitor the heat fluxes going through the thermosyphon wall. The locations of the temperature and heat flux sensors are shown in Figure 3.12.

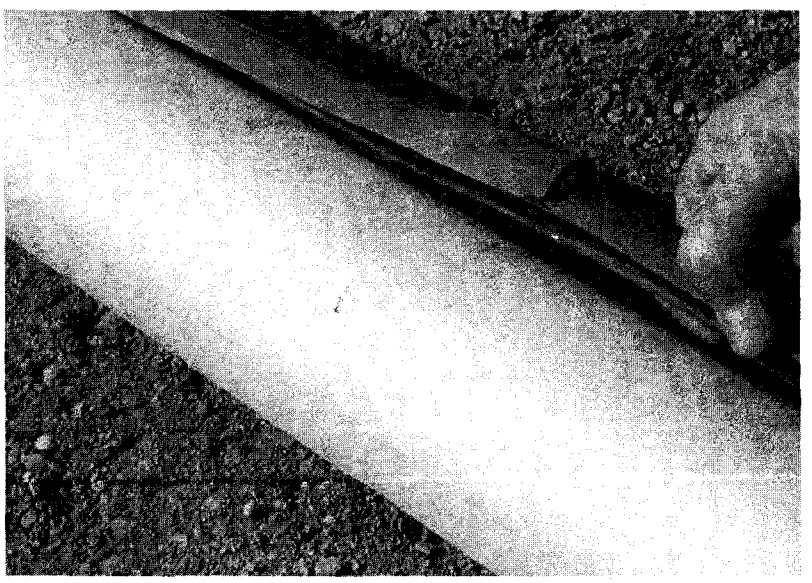

Figure 3.13 Thermistor string installed on the thermosyphon.

The thermistor string installed on the side of the thermosyphon wall is protected by a PVC pipe shell as shown in Figure 3.13. These PVC shells protect the temperature sensors and wiring from the coarse embankment material. However, they are not able to maintain good thermal contact between the temperature sensing element and the outside wall of the thermosyphon pipe. As a result, they add some extra thermal resistance to the system that may impact thermosyphon wall temperature measurements. A numerical simulation is carried out in the next section to correct the temperature measurements and improve the estimate of actual wall temperatures.

A thin film heat flux sensor installed on the tip of the thermosyphon is shown in Figure 3.14. The wiring of the heat flux sensor is also protected by PVC shells. But the sensors themselves are only protected by epoxy glue, which was mixed with carbon powder to yield a similar thermal conductivity as the surround embankment material. These heat flux sensors are also installed on the side of the pipe wall. The pipe is rotated inwards for 90 degrees from the position shown in Figure 3.14. In the final position of the thermosyphon, the thermistor string and the heat flux sensors are located on either side of the pipe.

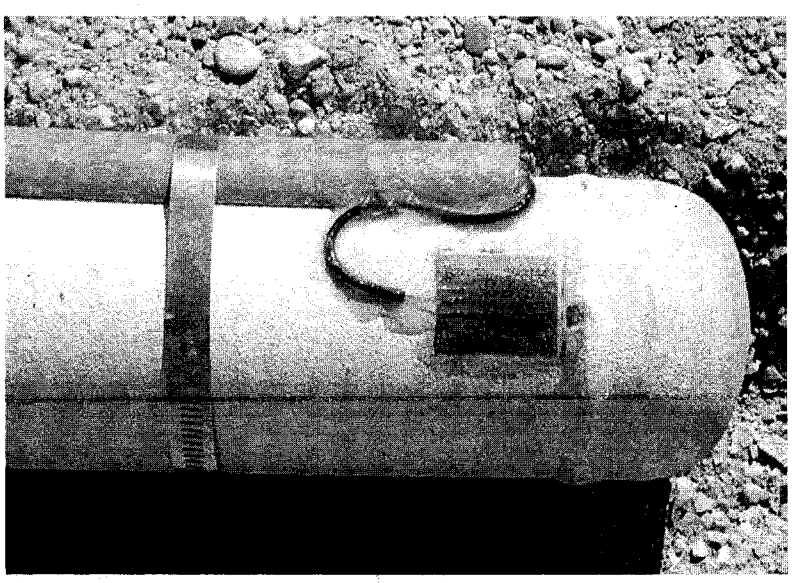

Figure 3.14 Thin film heat flux sensor on the thermosyphon.

The data acquisition equipment consists of a Campbell CR10X data logger and AM416 multiplexers. The data logging station is connected to AC power with 12 volt DC backup. The data logger is programmed to record and store temperature and heat flux data at the beginning of every hour. Temperature and heat flux data are stored in a 4 MB storage module which runs in a ring mode. Storage capacity is sufficient for more than a year of data storage. Data is periodically downloaded to a portable computer for archiving and later analysis.

3.2.3 Results and Discussion

3.2.3.1 Data history

Installation of the test section and instrumentation system was completed in the summer of 2004 and operation of the data logging system began in September of 2004. The final completion of the Thompson Drive project took place during the summer of 2005 when final paving operations were completed. During the winter of 2004-05 the roadway was not in use and snow removal operations were not at normal levels. At several times during the year, snow was allowed to accumulate to a depth of 20 cm or more before plowing operations were undertaken. The residual snow cover did provide some insulation effect which likely hindered the operation of the hairpin thermosyphons.

The performance of the hairpin thermosyphons during the first two years of operation was examined by directly analyzing the evaporator and condenser temperatures and heat flux readings. Figure 3.15 shows a time history of thermosyphon wall temperatures throughout the first two years of operation, including temperature data from sensors D3-1, D3-2, D3-3, and D3-4 located on the evaporator pipe, and E3-1, E3-2, E3-3, and E3-4 located on the condenser pipe. The black dashed line shows a record of the ambient air temperature, with its scale indicated on the right side of the plot. All eight wall temperature readings are plotted in different colors with their scale on the left side of the plot.

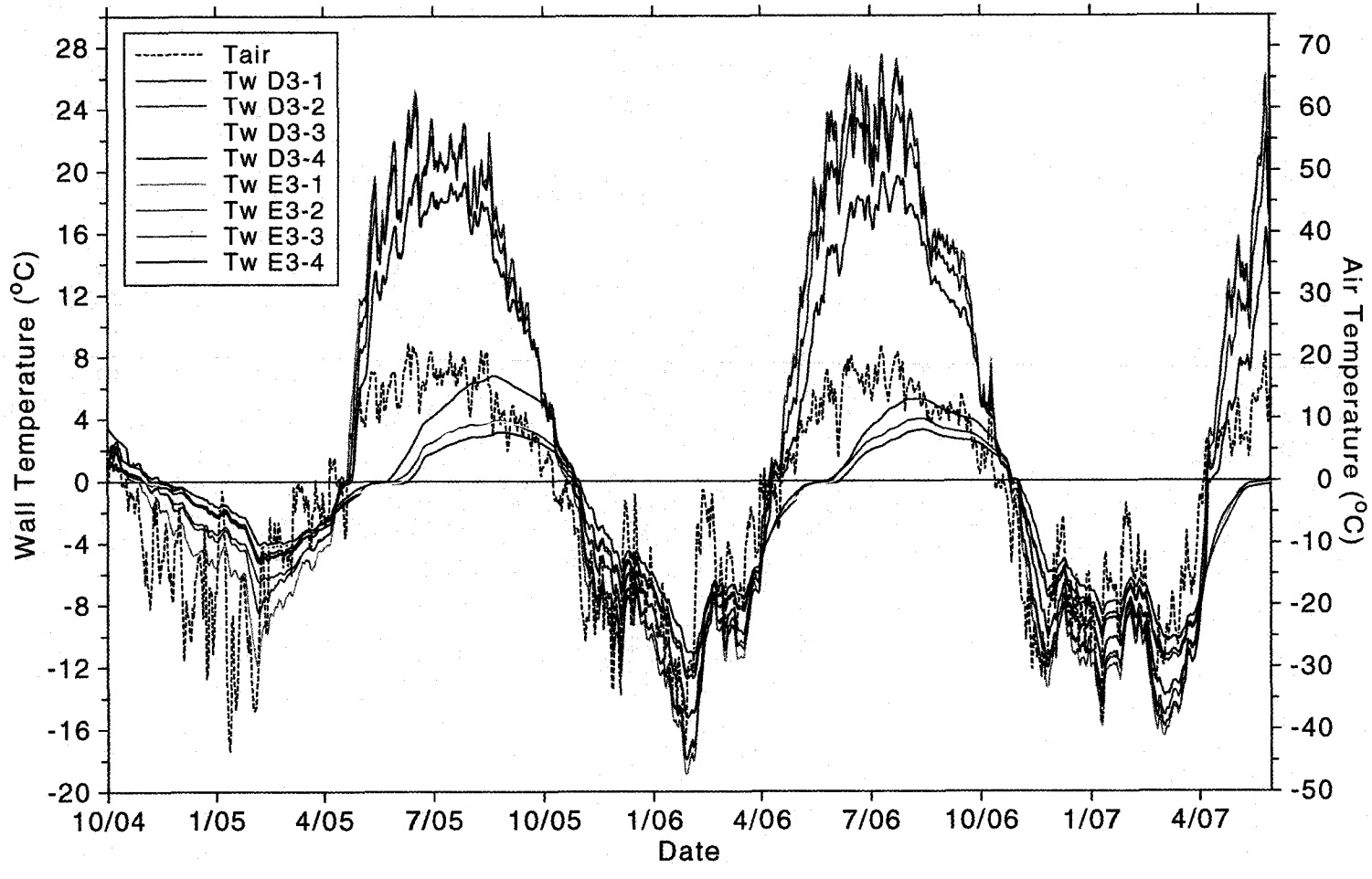

Figure 3.15 Temperature history of hairpin thermosyphon.

During winters, wall temperature readings from the condenser and the evaporator are very close to each other, indicating the thermosyphon is operational. The working fluid in the thermosyphon is circulating and the working temperature is held close to the saturation temperature in both the evaporator and the condenser. However, in summer months when the upper condenser section experiences high temperatures compared to the evaporator, the thermosyphon shuts down, resulting in a large temperature difference between the condenser and evaporator. These effects are clearly illustrated in Figure 3.15, which shows a temperature difference of just a few Celsius degrees during winters and a much larger value on the order of 15-20 C° during summer months. Large temperature differences between the evaporator and the condenser during the summer are also aided by the presence of the insulation layer separating the two.

Examining Figure 3.15 more closely for the first winter of operation reveals some significant differences between the condenser temperatures given by the E3 curves and the air temperature. There is also a relatively slow reduction in the E3 temperature curves in the November 2004 to February 2005 time frame, despite the occurrence of very low air temperatures. These effects indicate somewhat diminished thermosyphon effectiveness likely due to the insulating snow layer that was present at the surface of the embankment during this time period. On the other hand, the curves show a much more rapid temperature decrease during the falls of 2005 and 2006. Much closer tracking between the thermosyphon and air temperatures can be found during this period. This is a result of regular roadway maintenance and the lack of a surface snow layer during the fall 2005 and fall 2006 time period. Finally, examining the temperature history during the summer of 2005 and 2006, it is apparent that the condenser temperature tracks the air temperature fairly closely, although in some cases the condenser is even warmer than the ambient air, likely due to high pavement surface temperatures. On the other hand, the evaporator temperatures are much lower and do not rise above 0°C until sometime in late June, eventually reaching maximum values on the order of +4°C during late summer.

The thermosyphon wall heat flux history for the first two years of operation is shown in Figure 3.16. The black solid line shows the air temperature, plotted on the scale shown on the right side of the figure. Readings from heat flux sensors A through F are plotted using different colors. As shown in Figure 3.16, heat flux sensors A, B, and C are located on the evaporator while D, E, and F are located on the condenser. These heat flux sensors measure the local heat flux rates in W/m^2 and return a positive reading when heat enters the thermosyphon wall from the surrounding soil and a negative value when it exits. As a result, the heat flux sensors on the evaporator have positive readings during the winter, while those on the condenser have negative readings. During summer the heat flux readings are approximately zero, indicating that the thermosyphons are inactive. The noticeable spike in the heat flux value for sensor E that occurred in August of 2005 was caused by the installation of the asphalt pavement at the surface of the roadway.

The seasonal heat flux variations shown in Figure 3.16 offer strong evidence of the thermal diode effect produced by the hairpin thermosyphons. Heat transfer from the evaporator to the condenser during winter is approximately $50W/m^2$, or 150 W total, when the ambient temperature is −20 °C based on approximately equal condenser/evaporator surface areas of 3 m^2. During summer these values effectively drop to zero and heat is not re-injected into the embankment by the thermosyphon. This results in a temperature depression at the location of the thermosyphon evaporators in the base of the embankment, thus helping to preserve the underlying permafrost.

3.2.3.2 Winter performance

Winter is the time of active operation of the thermosyphons. This section provides a closer examination of the temperature and heat flux data during the winter to reveal more details of the thermosyphon performance.

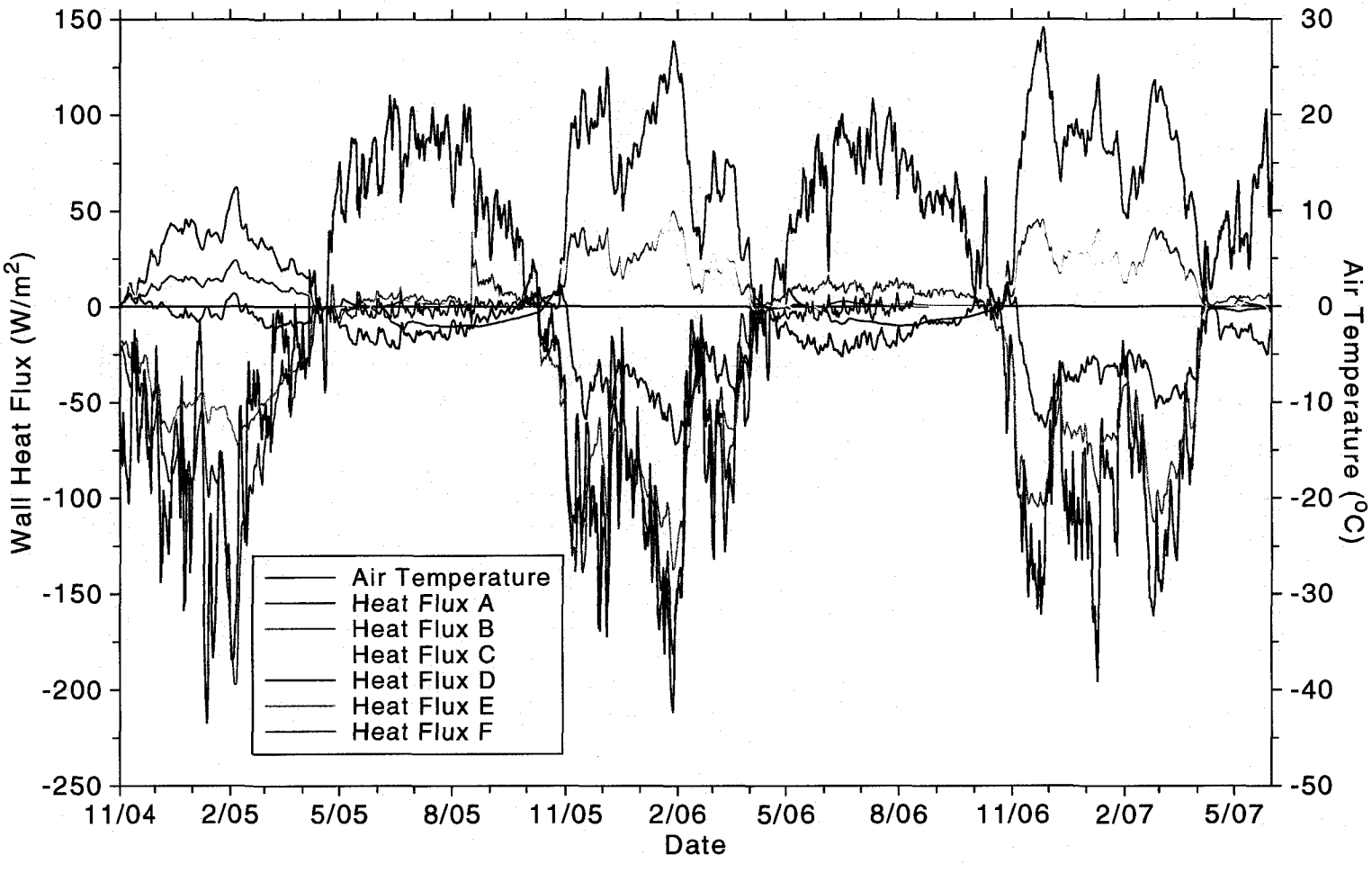

Figure 3.16 Heat flux history of hairpin thermosyphon.

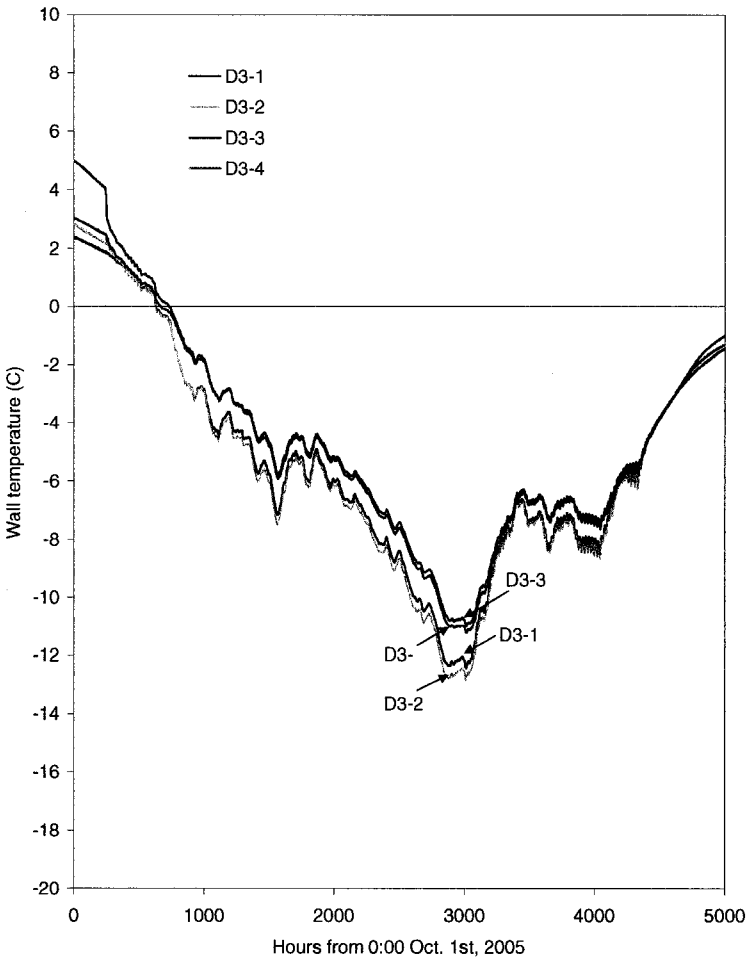

Figure 3.17 Evaporator wall temperature in winter.

Figure 3.17 shows the temperature readings on the thermosyphon evaporator during the period of October 2005 to April 2006, which was the first full winter of normal operation. There is a significant temperature difference (up to 2 C°) between sensors D3-1, D3-2 and sensors D3-3, D3-4. This temperature difference likely results because sensors D3-1 and D3-2 are located in the lower portion of the thermosyphon in the liquid puddle region where a large amount of heat is absorbed into the thermosyphon due to the large wetted pipe wall area. In the region where sensors D3-3 and D3-4 are located, it is likely that

only a small portion the pipe wall is wetted by the returning rivulet of condensate from the condenser. The wall heat flux in this upper portion is not as large as that of the liquid puddle region due to the limited area of the wetted wall surface. Therefore, the wall temperature in this portion of the evaporator is closer to the warm soil temperature. When the condensate returns from the condenser, it is typically slightly subcooled. It absorbs heat and warms as it travels down along the evaporator on the way to the liquid puddle. This is likely the reason why sensor D3-4 is slightly colder than sensor D3-3 and sensor D3-2 is slightly colder than sensor D3-1.

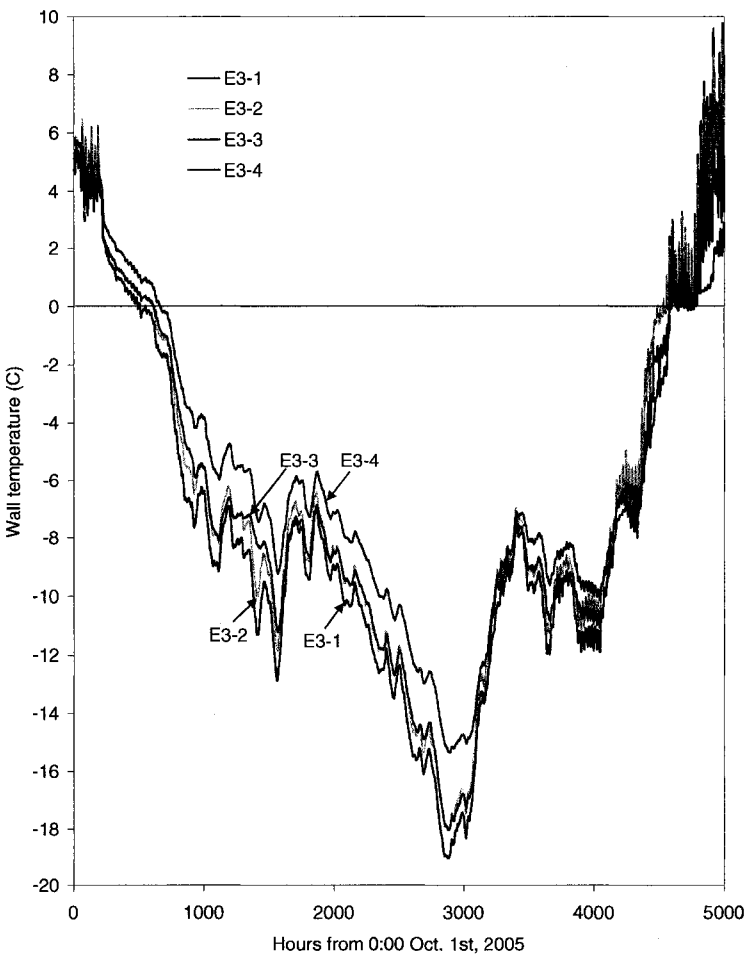

Figure 3.18 Condenser wall temperature in winter.

For the condenser wall temperature readings, a similar plot, Figure 3.18, is made to reveal the details of the condenser temperature behavior. Because the condenser location is very close to the road surface and the ambient air, the temperature fluctuations on the condenser wall are much higher in magnitude than those on the evaporator (shown in Figure 3.17). As can be seen from Figure 3.11 and Figure 3.12, sensor E3-4 is located right beneath the sidewalk where the distance between the sensor and the road surface is larger than the other condenser sensors. This results in a higher thermal resistance between the condenser and the ambient air and thus a higher wall temperature, as shown in Figure 3.18. Located under the driving surface, sensors E3-1, E3-2 and E3-3 have relatively low temperatures compared to sensor E3-4. Sensor E3-1 located on the tip of the condenser, and has the lowest temperature reading because it is located the closest to the road surface.

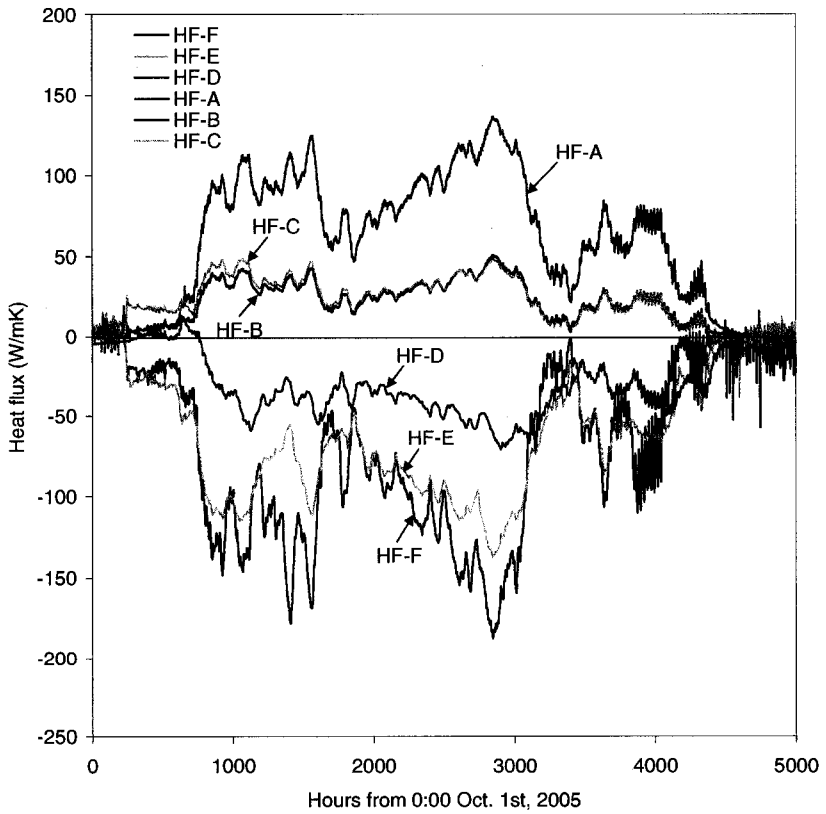

Figure 3.19 Wall heat flux during in winter.

Examination of the evaporator and condenser heat flux values shown in Figure 3.19 reveals a significantly different heat flux behavior along different segments of the condenser and evaporator. For the evaporator, it is clear that heat flux sensor A gives significantly larger readings than B or C which track fairly closely to one another. As for the temperature variation in the evaporator, this is also a result of liquid transport and distribution in the evaporator. As condensate returns via the riser from the condenser to the evaporator, it flows down the evaporator pipe in a liquid rivulet in the bottom of the pipe cross section and collects in the liquid puddle at the bottom. As a result, there is a larger fraction of wetted evaporator wall at the location of sensor A as opposed to the location of B or C. This, in turn, results in a greater potential for boiling and vapor generation and, thus, a higher heat flux at the location of sensor A. The heat flux situation is more complicated in the condenser. For the condenser, the far tip where sensor F is located is the closest to the asphalt surface and thus experiences the least thermal resistance between the condenser surface and the ambient air. Heat flux sensor D on the other hand, is located beneath the sidewalk and has a relatively large thermal resistance to the ambient air. As a result, the heat flux out of the condenser at the location of sensor F is generally larger than at E or D.

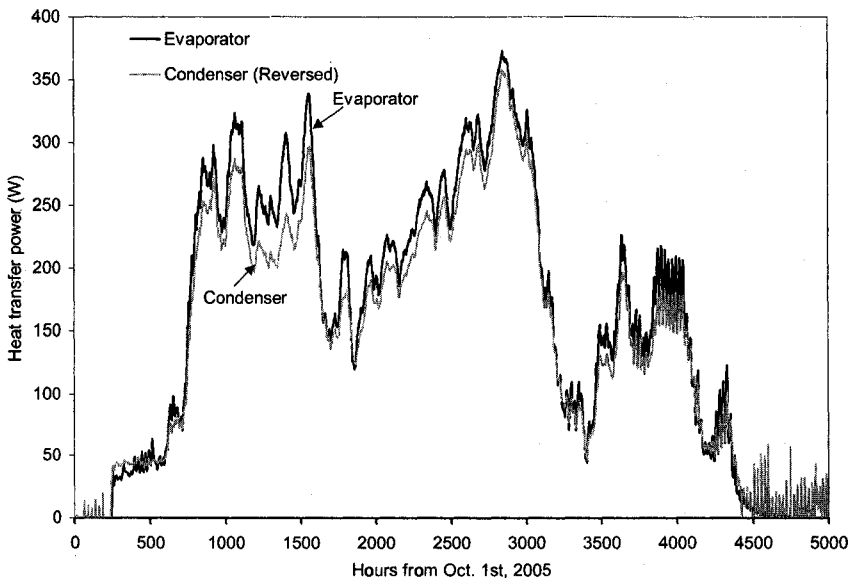

Figure 3.20 Heat transfer power comparison.

The overall heat transfer rates entering the evaporator and exiting the condenser are compared in Figure 3.20. The calculation of these two heat transfer rates is based on the arithmetic mean of heat flux readings and the outer area of each pipe. To allow a direct comparison, the sign of the condenser values are reversed. As shown in Figure 3.20, these two heat transfer rates track each other fairly well. Most of the time, the condenser heat rate is slightly smaller than the evaporator. A small portion of the heat absorbed in the evaporator might be dissipated in the riser (adiabatic section), which in reality is not insulated.

3.2.3.3 Heat transfer rate vs. temperature difference

To reveal the overall performance of the hairpin thermosyphon, the heat transfer power through the thermosyphon is plotted against the temperature difference between the evaporator and the condenser wall, as shown in Figure 3.21. The data points in this plot are spaced at one hour intervals stretching from 0:00 hrs, Jan. 01, 2005 to 23:00 hrs, Jul. 31, 2006, totaling about 14,000 points in all. The temperature difference is calculated by taking the difference between the average temperatures (arithmetic average) of the evaporator and condenser. The heat transfer rate is calculated based on the average heat flux and the outer surface area of the evaporator.

As shown in Figure 3.21, when the condenser is warmer than the evaporator (temperature difference is negative), the hairpin thermosyphon is inactive, and the measured heat transfer rates are nearly zero. Once the condenser temperature drops lower than the evaporator (positive temperature difference), the thermosyphon starts immediately. The heat transfer rate and the temperature difference maintain a quite linear relation when the hairpin thermosyphon is active. According to the plot, a 5 C° temperature difference induces a 350 W total heat transfer power, which indicates a 0.014 C^o/W effective thermal resistance of the hairpin thermosyphon. Because the air and soil temperatures are always in flux, transient effects are very likely the reason for the data scatter. Under stead-state conditions, the data should concentrate closer to a single line. The hairpin

thermosyphon that has been monitored at test section #3 has a 10 m condenser, a 2 m adiabatic section, and a 17 m evaporator. The diameter of both the evaporator and the condenser is 3-inch (76.2 mm), the diameter of the adiabatic section is 3/4-inch (19.0 mm). The conductance of this thermosyphon is about 90 W/C^o.

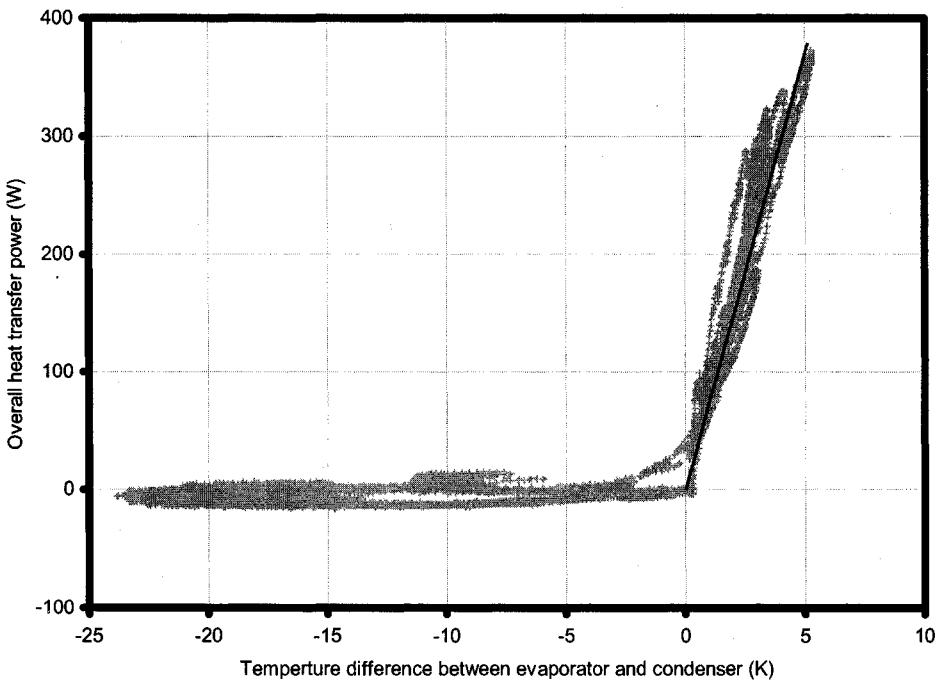

Figure 3.21 Overall heat transfer rate variation with temperature difference between the evaporator and the condenser.

As described previously, the thermistor string attachment to the thermosyphon pipe wall does not allow perfect thermal contact between the temperature sensors and the pipe wall and, thus, some error is introduced. To correct the errors from this configuration, a 2D numerical simulation is carried out to obtain the dependence between the measurement error and the heat flux through the thermosyphon wall under steady state conditions.

The geometry of the thermistor string protected by the PVC shell is shown in Figure 3.22. Only the region of the upper right quarter with a radius of 2.5 m is considered in the

numerical simulation. A heat flux boundary is used on the outer wall of the thermosyphon, and a constant temperature boundary is used at the boundary of 2.5 m radius. Symmetric boundaries are used on the horizontal and vertical boundaries. The gap between the PVC cover and the thermosyphon wall is considered filled with stagnant air. The heat transfer in this gap is assumed to be via pure conduction. The thermal conductivity of air is taken as an constant of 0.024 $W/(m \cdot K)$. The thermal conductivity of PVC is taken as 0.19 $W/(m \cdot K)$. The embankment material is assumed to be a frozen sandy gravel with a density of 1700 kg/m^3 and a water content of 10%. The thermal conductivity of this gravel is about 1.8 $W/(m \cdot K)$.

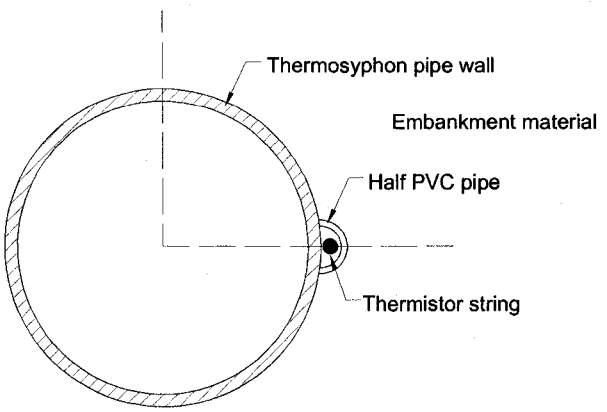

Figure 3.22 Configuration of thermistor string on the thermosyphon pipe.

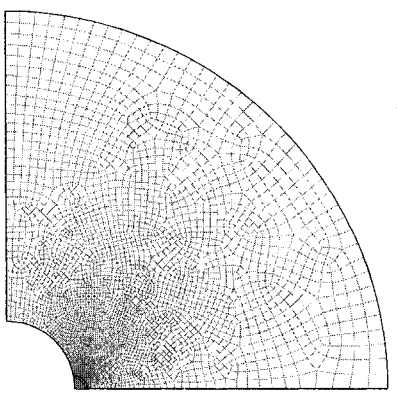

Figure 3.23 The mesh generated for the thermistor measurement correction problem.

The mesh for the problem domain is generated with GAMBIT as shown in Figure 3.23. A plot of the typical temperature contours near the PVC shell region is shown in Figure 3.24. Away from the PVC, the temperature contours are basically parallel to each other, which indicate a radial heat flow. Because of the high thermal resistance of the air trapped in the PVC cover, the temperature gradient is much higher in this region. Outside the PVC cover, heat flow is bent towards the PVC to compensate for the small heat transfer through the cover.

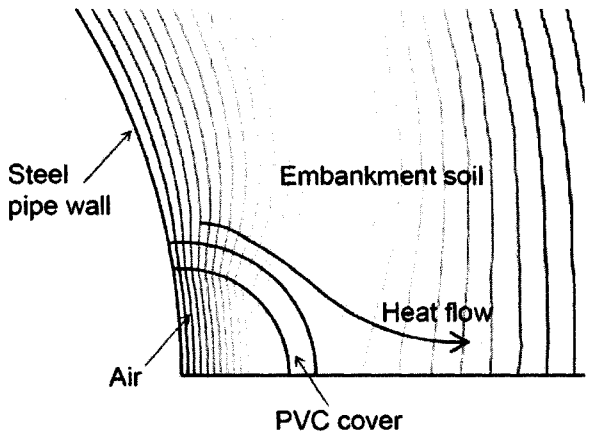

Figure 3.24 Temperature contours near the PVC cover.

The thermistors are assumed to be at the center of the air gap. Based on the nature of this problem, the temperature measurement error should have a linear relation with the heat transfer through the thermosyphon wall. At zero heat flux conditions, the error is zero. As a result, only one working condition needs to be simulated to get the relation needed for error correction. The dependence of the temperature measurement error on the heat flux was found to be:

$$\Delta T_{error} = 0.0044q \tag{3.10}$$

where $\Delta T_{error} = T_{measurement} - T_{wall}$ is the measurement error, and q is the heat flux through the pipe wall.

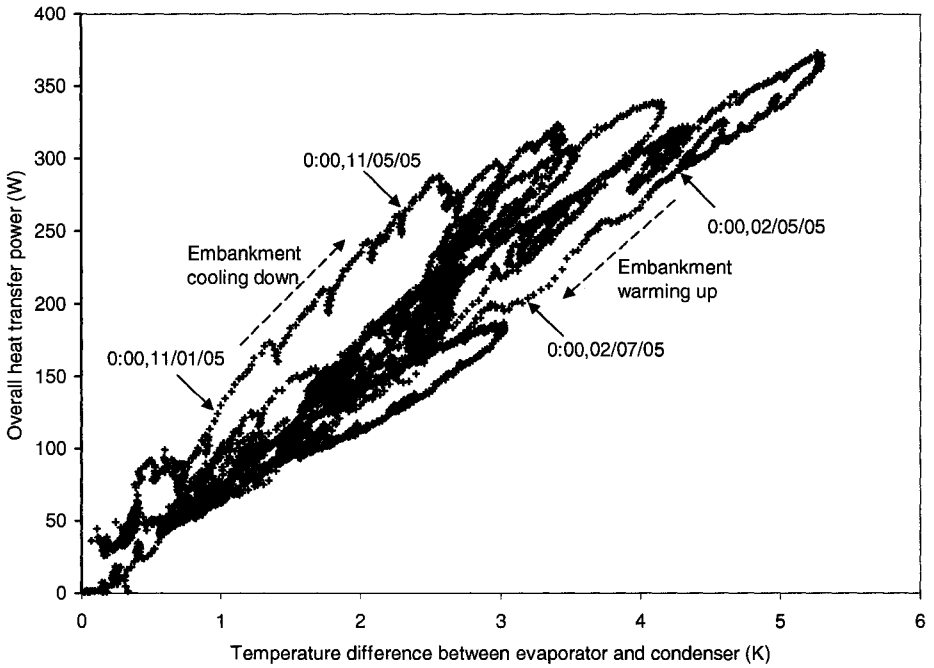

Figure 3.25 Heat transfer power vs. temperature difference for the active thermosyphon.

The data with corrected temperature measurements is plotted again in Figure 3.25 for the period when the thermosyphon is under active operation. The data points show a common pattern during embankment warming and cooling periods. Because of the shielding of the temperature sensors by the PVC covering, the time response of these temperature sensors tends to be slower than that of the heat flux sensors. During embankment cooling (e.g. the period of 11/01/2005 to 11/05/2005 indicated in Figure 3.25) the heat transfer power changes in advance of the temperature difference, which results in a higher position in the plot in Figure 3.25 than the steady-state situation. Similarly, during embankment warming, the heat transfer power changes in advance of the temperature difference, which results in a lower position on the plot than a steady-state situation. The differences in transient response combined with diurnal periodic, or annual temperature fluctuations results in the circular pattern of the data over the period of the cycle. This is illustrated by the detailed shape of the curve in Figure 3.25. When the rate of

temperature change is low, the situation is closer to steady-state and the data points should concentrate more towards centralized linear behavior.

The operational hairpin thermosyphon data described in this section is to be compared with the results from a hairpin thermosyphon model in Chapter 6. More detailed description regarding the thermosyphon road test is available in J. Xu and D. Goering [8].

3.3 References:

[1] Campbell Scientific, I. (2003). CR10X measurement and control module operator's manual. Logan, UT: 7.7-7.8.

[2] Chen, J. C. (1966). "Correlation for Boiling Heat Transfer to Saturated Fluids in Convective Flow." Industrial & engineering chemistry process design and development 5(3): 322-329.

[3] France, I. (2003). R744 Thermophysical Properties of Refrigerants. Paris.

[4] Goering, D. J. (2001). ACE and Thermosyphon Design Features Loftus Road Extension Project. Fairbanks, University of Alaska Fairbanks: 1-57.

[5] Goering, D. J. (2005). Loftus Road Extension Project - Final Report. Fairbanks, Alaska Department of Transportation & Public Facilities: 1-79.

[6] Kakac, S., R. K. Shah, et al. (1987). Handbook of Single-Phase Convective Heat Transfer. New York, John Wiley & Sons, Inc.

[7] Omega (2006). HFS-3, HFS-4 Thin Film Flux Sensors User's Guide, Omega Engineering Inc.

[8] Xu, J. and D. Goering (2008). "Experimental validation of passive permafrost cooling systems." Cold Regions Science and Technology: 15.

[9] Yang, S. (1998). Heat transfer. Beijing, Higher Education Press.

Chapter 4 Numerical Modeling

4.1 Introduction

The purpose of this chapter is to present a model of the heat transfer and fluid flow characteristics of a "hairpin" thermosyphon treated as a long inclined two-phase closed thermosyphon with carbon dioxide as the working fluid. The system is shown schematically in Figure 4.1.

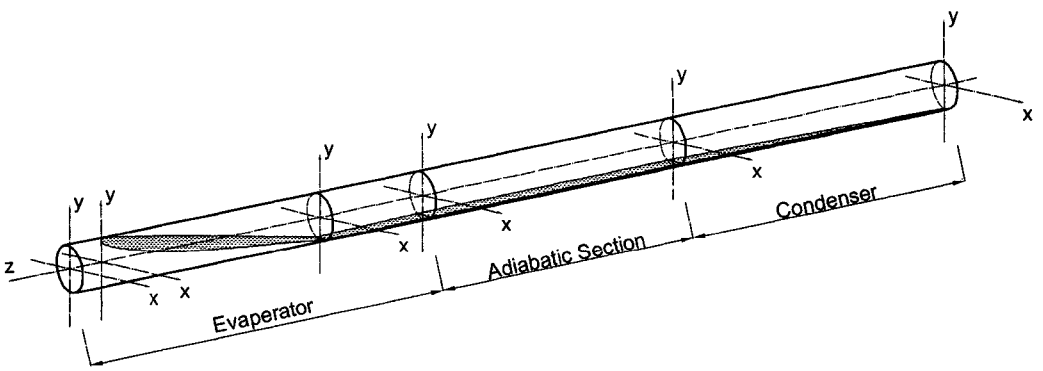

Figure 4.1 Inclined thermosyphon model domain

As a result of a temperature difference between the evaporator and condenser, the working fluid evaporates (boils) in the evaporator and rises through the adiabatic section to the condenser, where the vapor condenses on the cold pipe wall. The condensate flows back to the evaporator under the assistance of the gravity. As long as the evaporator is warmer than the condenser, the evaporation, condensation and working fluid circulation will continuously transfer heat from the evaporator to the condenser.

4.2 General Formulation

The general governing equations for an incompressible Newtonian fluid are as follows.

Mass conservation:

$$\frac{\partial \rho}{\partial t} + \nabla \cdot (\rho \vec{V}) = \dot{M} \tag{4.1}$$

where ρ is the fluid density, $\vec{V}$ is the velocity and $\dot{M}$ is the mass generation.

Momentum conservation:

$$\frac{D\vec{V}}{Dt} = \vec{F} - \frac{1}{\rho}\nabla p + \upsilon\nabla^2\vec{V} \tag{4.2}$$

where p is the pressure, $\vec{F}$ is the body force, and υ is the kinematic viscosity.

Energy conservation:

$$\frac{DT}{Dt} = \alpha\nabla^2 T + \frac{1}{\rho c_p}\Phi \tag{4.3}$$

where α is the thermal diffusivity, T is the temperature, c_p is the specific heat, and Φ is the dissipation function for incompressible flow (including the internal heat generation).

4.3 Simplifying assumptions

The assumptions made in the initial formulation are that the vapor is saturated, that the Mach number of the vapor flow is low enough that compressibility effects in the vapor phase are negligible, and that the entrainment of liquid droplets in the vapor phase is negligible. These assumptions are well justified in many systems of practical interest including the type of thermosyphon system examined here

Under actual working conditions of the hairpin thermosyphon, the temperature difference throughout the thermosyphon is small. Both the liquid and the vapor phases are near the saturation temperature. The thermophysical properties such as density, viscosity, and thermal conductivity can all be considered constants.

The governing equations in Cartesian coordinates are as follows:

Mass conservation:

$$\frac{\partial u}{\partial x} + \frac{\partial v}{\partial y} + \frac{\partial w}{\partial z} = \frac{\dot{M}}{\rho} \tag{4.4}$$

where u is the velocity in the x direction, v is the velocity in the y direction and w is the velocity in the z direction.

Momentum conservation:

$$(M_x)\quad \rho\left(\frac{\partial u}{\partial t}+u\frac{\partial u}{\partial x}+v\frac{\partial u}{\partial y}+w\frac{\partial u}{\partial z}\right)=-\frac{\partial P}{\partial x}+X+\mu\left(\frac{\partial^2 u}{\partial x^2}+\frac{\partial^2 u}{\partial y^2}+\frac{\partial^2 u}{\partial z^2}\right) \tag{4.5}$$

$$(M_y)\quad \rho\left(\frac{\partial v}{\partial t}+u\frac{\partial v}{\partial x}+v\frac{\partial v}{\partial y}+w\frac{\partial v}{\partial z}\right)=-\frac{\partial P}{\partial y}+Y+\mu\left(\frac{\partial^2 v}{\partial x^2}+\frac{\partial^2 v}{\partial y^2}+\frac{\partial^2 v}{\partial z^2}\right) \tag{4.6}$$

$$(M_z)\quad \rho\left(\frac{\partial w}{\partial t}+u\frac{\partial w}{\partial x}+v\frac{\partial w}{\partial y}+w\frac{\partial w}{\partial z}\right)=-\frac{\partial P}{\partial z}+Z+\mu\left(\frac{\partial^2 w}{\partial x^2}+\frac{\partial^2 w}{\partial y^2}+\frac{\partial^2 w}{\partial z^2}\right) \tag{4.7}$$

where X is the body force in the x direction, Y is the body force in the y direction, and Z is the body force in the z direction.

Energy conservation:

$$\rho C_p\left(\frac{\partial T}{\partial t}+u\frac{\partial T}{\partial x}+v\frac{\partial T}{\partial y}+w\frac{\partial T}{\partial z}\right)=k\left(\frac{\partial^2 T}{\partial x^2}+\frac{\partial^2 T}{\partial y^2}+\frac{\partial^2 T}{\partial z^2}\right)+\Phi \tag{4.8}$$

In addition to these basic assumptions, more assumptions are necessary to further simplify the problem:

1. Steady state conditions;
2. A long pipe, $L >> D$;
3. For both liquid and vapor, $w >> u \sim v \sim 0$;
4. The liquid film thickness varies slowly in the z direction, $\frac{dH}{dz} << 1$;
5. For both liquid and vapor, $\frac{\partial^2 w}{\partial z^2} << \frac{\partial^2 w}{\partial x^2} \sim \frac{\partial^2 w}{\partial y^2}$;
6. In liquid film, gravity is the dominant body force;
7. Both liquid and vapor flows are laminar.

Both the evaporator and the condenser of the thermosyphon are long pipe sections, in which the diameter is much smaller than the length of the pipe. In most regions of the pipe, the velocity direction (for both vapor and liquid phase) will closely parallel the pipe axis (z-axis), and the velocities in x and y direction can be regarded as negligible without introducing significant error.

Another simplification from the "long pipe" assumption is that the mass condensation or evaporation rate at a specific location is much smaller than the local bulk mass flow rate in z-direction. The mass transfer between the liquid and vapor phases can then be considered a small uniform mass source distributed over the cross section. What's more, this small mass source also indicates a small flow rate gradient in the z-direction (or a small z-velocity gradient). Under no-slip boundaries, the velocity gradients in x and y directions are relatively large, and the velocity gradient in z-direction can thus be considered negligible.

According to a typical set of data from Thompson Drive (0:00 hrs, Dec. 15, 2005), the highest Reynolds number of core vapor flow (based on the inner pipe diameter) is about 1500 which is smaller than the critical Reynolds number of 2300. Therefore, the assumption of laminar vapor flow is well justified.

A schematic of a control volume in the thermosyphon is shown in Figure 4.2. It can serve to represent any section of the thermosyphon where both liquid and vapor phases coexist in a countercurrent stratified flow. As shown in Figure 4.2, the liquid flow occupies a small fraction of the cross-section at the bottom of the pipe. Under the action of gravity it flows in the positive z direction. The vapor phase, on the other hand, flows in the opposite direction and occupies the upper portion of the flow channel. H is defined as the film thickness of the liquid rivulet and is clearly a function of the z coordinate.

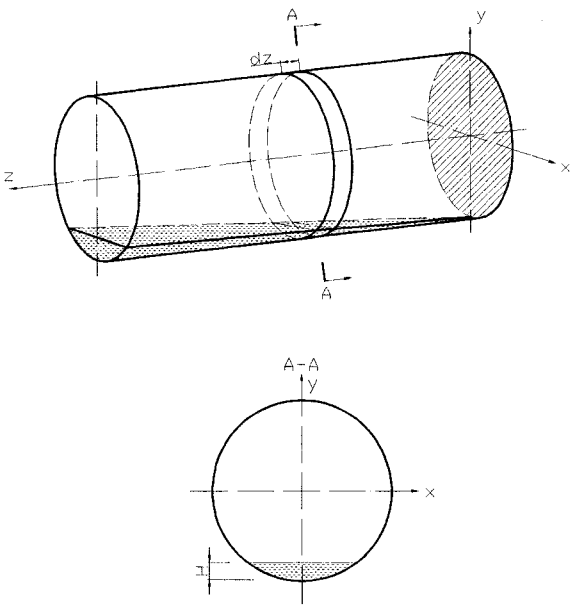

Figure 4.2 A control volume in the thermosyphon

Utilizing the above assumptions, the mass conservation can be written as:

Liquid film: $$\rho_l\left(\int_{z+dz} w_l dA_l - \int_z w_l dA_l\right) = \dot{m}_l C(z)dz \tag{4.9}$$

Vapor core: $$\rho_v\left(\int_{z+dz} w_v dA_v - \int_z w_v dA_v\right) = \dot{m}_v C(z)dz \tag{4.10}$$

Where A_l is the cross sectional area of the liquid phase, A_v is the cross sectional area of the vapor phase, $C(z)$ is the perimeter (or wetted perimeter in the evaporator) where condensation (or boiling) is occurring, and $\dot{m}_l$ and $\dot{m}_v$ are the mass source terms defined on the interface for the liquid and the vapor phase, respectively.

Because of negligible velocity in the x and y direction, only the z-momentum equation (M_z) needs to be considered. It takes a simplified form:

Liquid film: $$0 = \frac{g\sin\theta}{\upsilon_l} + \left(\frac{\partial^2 w_l}{\partial x^2} + \frac{\partial^2 w_l}{\partial y^2}\right) \tag{4.11}$$

Vapor Core: $$0 = -\frac{1}{\rho_v \upsilon_v}\frac{\partial P}{\partial z} + \left(\frac{\partial^2 w_v}{\partial x^2} + \frac{\partial^2 w_v}{\partial y^2}\right) \tag{4.12}$$

where θ is the inclination angle of the pipe.

In forced convection configurations, the mass conservation and momentum equations are sufficient for determining the velocity distribution within the flow field [1]. In such cases, the fluid temperature distribution can be determined as an afterthought, by using the just-determined velocity distribution and the energy equation.

According to the above assumptions, the vapor/liquid temperature will be near saturation throughout the entire thermosyphon. The condensation heat transfer in the condenser and the evaporation heat transfer in the evaporator are described with empirical correlations. Therefore, the energy conservation can be simplified as

$$q(z) = h(z)\Delta T(z) \tag{4.13}$$

where

- q is the local heat flux between the working fluid and the thermosyphon wall;
- h is the phase change heat transfer coefficient;
- ΔT is the temperature difference between the working fluid and the thermosyphon wall;

All of these parameters are functions of the z-coordinate.

To complete the governing equations, supplemental relations for phase change and heat transfer are required:

In the liquid: $$\dot{m}_l(z) = \frac{q(z)}{L} \tag{4.14}$$

In the vapor: $$\dot{m}_v(z) = -\dot{m}_l(z) \tag{4.15}$$

where L is the latent heat of phase change.

By combining Equation (4.13) with Equations (4.14) and (4.15), the energy conservation can also be expressed as

In the liquid: $$\dot{m}_l(z) = \frac{h(z)\Delta T(z)}{L} \tag{4.16}$$

In the vapor: $$\dot{m}_v(z) = -\frac{h(z)\Delta T(z)}{L} \tag{4.17}$$

4.4 Boundary conditions

4.4.1 Flow boundaries

No-slip boundaries, Equation (4.18) and(4.19), are applied to the wall boundaries. No-slip and force balance boundaries, Equation (4.20) to (4.22), are applied to the liquid-vapor interface.

In the liquid: $w_l = 0$ at pipe wall (4.18)

In the vapor: $w_v = 0$ at pipe wall (4.19)

On the liquid-vapor interface

$$w_l = w_v \tag{4.20}$$

$$\mu_l \frac{\partial w_l}{\partial x} = \mu_v \frac{\partial w_v}{\partial x} \tag{4.21}$$

$$\mu_l \frac{\partial w_l}{\partial y} = \mu_v \frac{\partial w_v}{\partial y} \tag{4.22}$$

4.4.2 Thermal boundaries

To focus on the inner processes of the thermosyphon, temperature boundary conditions as given in Equations (4.23) and (4.24), are used at the condenser and the evaporator walls. An adiabatic boundary, as shown in Equation (4.25), is used in the adiabatic section.

In the condenser: $T_{w,c} = T_1$ (4.23)

In the evaporator: $T_{w,e} = T_2$ (4.24)

In the adiabatic section: $q_{w,a} = 0$ (4.25)

The governing Equations, (4.11) to (4.15), and boundary conditions, (4.18) to (4.25), represent a complete quasi one-dimensional model of the inclined two-phase closed thermosyphon with a two-dimensional analysis of the longitudinal velocity distribution in the cross section.

4.5 Non-dimensional Equations

The following non-dimensional variables are introduced to put the governing equations in non-dimensional form:

$$
\begin{aligned}
x^* &= \frac{x}{D} & y^* &= \frac{y}{D} & z^* &= \frac{z}{D} \\
\rho_l^* &= \frac{\rho_l}{\rho_l} = 1 & \rho_v^* &= \frac{\rho_v}{\rho_l} & \mu_l^* &= \frac{\mu_l}{\mu_l} = 1 \\
\mu_v^* &= \frac{\mu_v}{\mu_l} & w_l^* &= \frac{w_l}{w_0} & w_v^* &= \frac{w_v}{w_0} \\
\dot{m}_l^* &= \frac{\dot{m}_l c_{p,l} D}{k_l} & \dot{m}_v^* &= \frac{\dot{m}_v c_{p,l} D}{k_l} & T^* &= \frac{T - T_0}{T_{w,e} - T_{w,c}} \\
h^* &= \frac{h}{c_{p,l} w_0 \rho_l} & C^* &= \frac{C}{D} & m^* &= \frac{m}{\rho_l D^3}
\end{aligned}
\tag{4.26}
$$

where

$$
w_0 = \frac{D^2 \rho_l g \sin\theta^2}{\mu_l} \tag{4.27}
$$

This characteristic velocity is derived from a force balance between gravity and wall friction in liquid phase. T_0 is the working saturation temperature, $T_{w,e}$ is the wall temperature of the evaporator, and $T_{w,c}$ is the wall temperature of the condenser.

The governing equations can be written in the dimensionless form using the above variables as follows.

Mass conservation:

$$\rho_l^* \int_{z^*+dz^*} w_l^* dA_l^* - \int_{z^*} w_l^* dA_l^* = \dot{m}_l^* C^* dz^* \tag{4.28}$$

$$\rho_v^* \int_{z^*+dz^*} w_v^* dA_v^* - \int_{z^*} w_v^* dA_v^* = \dot{m}_v^* C^* dz^* \tag{4.29}$$

where A_l^* and A_v^* are the dimensionless cross sectional area in the liquid and vapor phase respectively.

Momentum conservation:

$$\mu_l^* \left(\frac{\partial^2 w_l^*}{\partial x^{*2}} + \frac{\partial^2 w_l^*}{\partial y^{*2}} \right) = \Phi_l^* \tag{4.30}$$

$$\mu_v^* \left(\frac{\partial^2 w_v^*}{\partial x^{*2}} + \frac{\partial^2 w_v^*}{\partial y^{*2}} \right) = \Phi_v^* \tag{4.31}$$

where

$\Phi_l^* = -\frac{\rho_l g \sin\theta}{\mu_l} \cdot \frac{D^2}{w_0}$ is the dimensionless source term in the liquid phase;

$\Phi_v^* = \frac{\partial P}{\partial z} \cdot \frac{1}{\mu_l} \cdot \frac{D^2}{w_0}$ is the dimensionless source term in the vapor phase.

Energy conservation:

$$\dot{m}_l^* = -\dot{m}_v^* = Ja \cdot Nu \cdot (T^* - T_w^*) \tag{4.32}$$

where

$$Ja = \frac{c_{p,l}(T_{w,e} - T_{w,c})}{L} \tag{4.33}$$

$$Nu = \frac{hD}{k_l} \tag{4.34}$$

The boundary conditions can also be put in non-dimensional form as follows:

In the liquid: $w_l^* = 0$ at the wall (4.35)

In the vapor: $w_v^* = 0$ at the wall (4.36)

On the liquid-vapor interface

$$w_l^* = w_v^* \tag{4.37}$$

$$\mu_l^* \frac{\partial w_l^*}{\partial x^*} = \mu_v^* \frac{\partial w_v^*}{\partial x^*} \tag{4.38}$$

$$\mu_l^* \frac{\partial w_l^*}{\partial y^*} = \mu_v^* \frac{\partial w_v^*}{\partial y^*} \tag{4.39}$$

4.6 Boiling and Condensation Heat Transfer

As discussed in Chapter 2 and 3, the modeling of boiling and condensation in a thermosyphon has proven challenging because of the lack of knowledge and the complexity of the mechanisms. The use of empirical correlations is probably a better way to describe the heat transfer processes associated with the phase-change phenomena.

4.6.1 Condensation heat transfer

Due to the small surface tension of CO_2, it was theorized that filmwise condensation was likely to occur in the hairpin thermosyphon condensers. This result was also verified by the lab experiment described in Chapter 3. Most of the experimental correlations and theoretical solutions are unable to predict the heat transfer performance when the condensation heat flux is extremely small. As discussed in Chapter 3, it is very likely that the condensation is not the dominant heat transfer mechanism. When transitioning from forced convection heat transfer to filmwise condensation, the convection heat transfer may still serve as a key mechanism of heat transfer even though filmwise condensation occurs at the same time. The experimental correlation developed in Chapter 3 can predict this heat transfer behavior very well, so this correlation will be used as part of the thermosyphon modeling.

4.6.2 Boiling heat transfer

The boiling heat transfer in the thermosyphon evaporator is another phenomenon that is difficult to simulate theoretically. Fortunately there have been abundant experimental studies in this area, most of which have resulted in experimental correlations. Several researchers including J.C. Chen [2], K. Gungor and R. Winterton [4; 5], S.G. Kandlikar

[6], Z. Liu and R. Winterton [7], J. Thome and El Hajal [11], C.Y. Park and Hrnjak [8; 9], H. Steiner et al. [10] and W. Zhang et al. [13] developed several general boiling heat transfer correlations based on a large bank of data both from their own experiments and from the literature. Additionally the correlations by C. Park [8; 9] and R. Yun et al. [12] were developed from experiments with CO_2 as the working fluid.

Under extremely small heat flux conditions, it is possible that single-phase liquid convection is sufficient to remove heat from the evaporator wall and that no nucleate boiling takes place. Thus, evaporation at the liquid-vapor interface may be the only phase-change process in the evaporator. This transitional evaporation would require a correlation which can cover heat transfer mechanisms of both pure convection and boiling. Fortunately, several correlations have been developed using a superposition method first introduced by J.C. Chen [2]. Chen's method combines the convection heat transfer and nucleate boiling heat transfer together with weighting coefficients. The promotion and suppression relationship between these two mechanisms can easily be considered in this type of correlation. After a careful review of all the available correlations developed with this method, the one developed by S. Kandlikar [6] in 1990 was selected to predict the heat transfer coefficient in the evaporator. This correlation eliminates the discontinuity at the transition point from single-phase convection to nucleate boiling and incorporates a fluid-dependent parameter to extend the applicability to other fluids that were not used in its development. This correlation is given in Equation (4.40).

$$\frac{h_{TP}}{h_l} = C_1 Co^{C_2} (25 Fr_{lo})^{C_5} + C_3 Bo^{C_4} F_{fl} \qquad (4.40)$$

where

h_{TP} is the two phase heat transfer coefficient;

h_l is the single-phase liquid heat transfer coefficient given by $h_l = 0.023 Re_l^{0.8} Pr_l^{0.4} (k_l / D)$;

$C_1 \sim C_5$ are constants developed in this study;

$Co = \left(\frac{1-x}{x}\right)^{0.8}\left(\frac{\rho_g}{\rho_l}\right)^{0.5}$ is the convection number;

$Fr_{lo} = \frac{G^2}{\rho_l^2 gD}$ is the Froude number with all flow as liquid;

$Bo = \frac{q}{Gh_{fg}}$ is the boiling number; and

F_{fl} is a fluid-dependent parameter.

The fluid-dependent parameter for carbon dioxide was not provided by S. Kandlikar [6]. As suggested by Kandlikar, the F_{fl} for carbon dioxide in current model was estimated as the multiplier in the H. Forster and N. Zuber [3] correlation for pool boiling.

4.7 Flow simulation

Most of the vapor and liquid flow in the thermosyphon can be considered to be forced convection. Under this forced convection configuration, the mass conservation and momentum equations are sufficient for determining the flow field, that is, the velocity distribution through the fluid [1]. In such cases, the velocity field and the temperature distribution are uncoupled. The fluid temperature distribution can be determined as an afterthought, by using the velocity distribution and the energy conservation principle. The governing equations to determine the velocity field are relatively simple, it is the geometry that complicates the problem. Numerical methods were used in solving this two-dimensional problem.

4.7.1 Method

A commercial CFD code, FLUENT, was used for this numerical simulation. The problem itself is actually a simple one, and FLUENT was selected mainly due to availability. Any other computer code that can solve two-dimensional Poisson equations could also be used. To solve this problem in FLUENT, an analog was made between this flow problem and the thermal conduction problem, both of which are governed by Poisson equations of a similar form. The equation for the heat conduction problem is

$$k\nabla^2 T = -\dot{q} \tag{4.41}$$

In this analogy, the dependent variables in the flow problem, the velocities, are taken as temperatures in the heat conduction problem. The viscosity is analogous to the thermal conductivity, and the source terms in the flow problem are analogous to the energy sources in the conduction problem. Comparing Equation (4.41) with Equations (4.30) and (4.31), the thermal conductivity and energy source term in Equation (4.41) can be determined as

$$k \sim \mu_l^* = 1;\ -\dot{q} \sim \Phi_l^* = 1 \qquad \text{in } \Omega_l \tag{4.42}$$

$$k \sim \mu_v^*;\ -\dot{q} \sim \Phi_v^* = \frac{\rho_v}{\rho_l} - \frac{dp}{dz}\frac{1}{\rho_l g \sin\theta} \qquad \text{in } \Omega_v \tag{4.43}$$

4.7.2 Verification

The numerical solution of the Poisson equations in FLUENT can be verified by simulating a simpler one-dimensional problem and comparing with the analytical solution. This one-dimensional problem is illustrated in Figure 4.3.

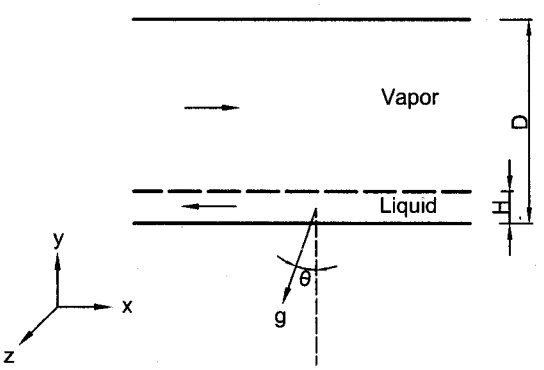

Figure 4.3 One-dimensional countercurrent problem

The distance between the top and bottom wall is D, the liquid film has a thickness of H, and the flow channel is infinite in the z direction. The liquid and vapor flow have exactly the same mass flow rate, but in opposite directions. The longitudinal component of

gravity is the dominant driving force for the liquid phase, while the pressure gradient drives the vapor phase. The countercurrent flow is balanced, and there is no acceleration in either the liquid or vapor phases. The velocity gradient in the x-direction is zero. This is a typical one-dimensional problem with velocity changing only in the y-direction. The governing equations are as follows:

$$\dot{m}_l = -\dot{m}_v \tag{4.44}$$

$$\mu_l \frac{\partial^2 w_l}{\partial y^2} = \rho_l g \sin(\theta) = \Phi_l \tag{4.45}$$

$$\mu_v \frac{\partial^2 w_v}{\partial y^2} = \frac{\partial p_v}{\partial z} = \Phi_v \tag{4.46}$$

The boundary conditions are:

$$w_l = 0 \qquad \text{at } y = 0 \tag{4.47}$$

$$w_l = w_v \qquad \text{at } y = H \tag{4.48}$$

$$\mu_l \left.\frac{dw_l}{dy}\right|_H = -\mu_v \left.\frac{dw_v}{dy}\right|_H \qquad \text{at } y = H \tag{4.49}$$

$$w_v = 0 \qquad \text{at } y = D \tag{4.50}$$

Integrating Equations (4.45) and (4.46) twice yields

$$w_l = \rho_l g \sin(\theta)\frac{y^2}{2} + C_1 y + C_2 \tag{4.51}$$

$$w_v = \frac{\partial p}{\partial z}\frac{y^2}{2} + C_3 y + C_4 \tag{4.52}$$

where, C_1 □ C_4 are coefficients from the integration. Including boundary conditions, from Equation (4.47) to (4.50), the coefficients can be determined as:

$$C_1 = -\frac{\Phi_l H^2 \mu_v - 2H^2 \Phi_l \mu_l + 2H\Phi_l D\mu_l + \Phi_v H^2 \mu_l - 2\Phi_v DH\mu_l + D^2 \mu_l \Phi_v}{2\mu_l (H\mu_v - H\mu_l + D\mu_l)} \tag{4.53}$$

$$C_2 = 0 \tag{4.54}$$

$$C_3 = -\frac{-\Phi_l H^2 \mu_v + 2H^2 \mu_v \Phi_v - \Phi_v H^2 \mu_l + D^2 \mu_l \Phi_v}{2\mu_v (H\mu_v - H\mu_l + D\mu_l)} \tag{4.55}$$

$$C_4 = \frac{DH(-\Phi_v D\mu_v + \Phi_v D\mu_l - \Phi_l H\mu_v + 2\Phi_v H\mu_v - \Phi_v H\mu_l)}{2\mu_v(H\mu_v - H\mu_l + D\mu_l)} \tag{4.56}$$

Introducing these coefficients back into Equations (4.51) and (4.52) yields the solution:

$$w_l = y^2 \frac{\Phi_l(H\mu_v - \mu_l H + \mu_l D)}{2\mu_l D(HD\mu_v - HD\mu_l + D^2\mu_l)} + y\frac{\Phi_l(2H^2\mu_l - H^2\mu_v - 2HD\mu_l) + \Phi_v\mu_l(2HD - H^2 - D^2)}{2\mu_l(H\mu_v - H\mu_l + D\mu_l)} \tag{4.57}$$

$$w_v = y^2 \frac{\Phi_v(H\mu_v - H\mu_l + D\mu_l)}{2\mu_v(H\mu_v - H\mu_l + D\mu_l)} + y\frac{(\Phi_l H^2\mu_v - 2\Phi_v H^2\mu_v + \Phi_v H^2\mu_l - \Phi_v D^2\mu_l)}{2\mu_v(H\mu_v - H\mu_l + D\mu_l)} + \frac{H^2 D(2\Phi_v\mu_v - \Phi_l\mu_v - \Phi_v\mu_l) + \Phi_v HD^2(\mu_l - \mu_v)}{2\mu_v(H\mu_v - H\mu_l + D\mu_l)} \tag{4.58}$$

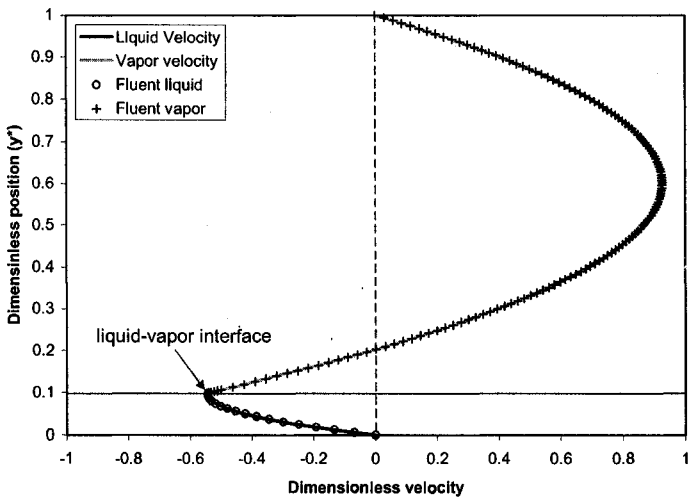

Figure 4.4 One-dimensional simulation in FLUENT with analytical solution

In the one-dimensional FLUENT simulation, the exact same method introduced in section 4.7.1 was used. In Figure 4.4, the numerical simulation result is compared with the analytical solution given in Equations (4.57) and (4.58). The diagram shows the velocity distribution in one cross-section of the flow channel for both the analytical

solution and the FLUENT simulation. In this case, the non-dimensional liquid film thickness is 0.1. The liquid-vapor interface is indicated by a horizontal solid line and the cross-section is indicated by a vertical dashed line. The y-axis is the same as in Figure 4.3 and shows the vertical position in the flow channel. The x-axis shows the non-dimensional velocity magnitude. Obviously, the FLUENT simulation matches the analytical solution very well. Therefore, it is reasonable to believe that numerical simulation in FLUENT can also provide an accurate prediction of the velocity distribution for the two-dimensional problem.

4.7.3 Two-Dimensional Simulation in FLUENT

The two-dimensional FLUENT simulation is similar to the one-dimensional case introduced in the previous section. A representative cross-section (with a 0.1D film thickness in this case) of the circular pipe flow channel is shown in Figure 4.5 with the generated mesh. A total of 2969 cells and 3052 nodes are involved in this grid. A fine boundary mesh is used near the wall area and the liquid-vapor interface to capture more details where high velocity gradients may exist.

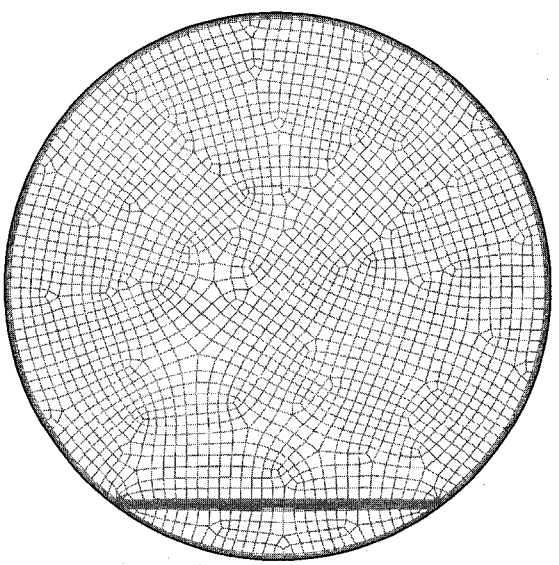

Figure 4.5 Mesh generated in Gambit for a two-dimensional pipe cross section

The source term in the liquid Equation (4.30) is known for any given film thickness, while an assumed pressure gradient can be used as the source term for the vapor Equation (4.31). Both the liquid and vapor equations can be solved together, and the flow rate of both phases can then be integrated over their own portion of the cross section. According to the steady state assumption and mass conservation, at any cross-section of the thermosyphon the mass flow rate of the liquid film and the vapor core should be equal in magnitude and opposite in direction. If the integrated flow rates of the liquid phase and vapor phases are not equal, modifications can be made to the pressure gradient term in the vapor equation. After a number of iterations, the integrated flow rates in both phases become close enough to be considered equal. This strategy is used to solve Equations (4.30) and (4.31) for a particular film thickness (H^*). In order to form a complete solution for the entire thermosyphon, these equations need to be solved for different film thicknesses. Ultimately, the velocity profile, flow rate and other flow characteristics can be regressed as functions of film thickness (H^*).

This iterative method was realized in FLUENT via the use of User Defined Functions (UDFs) that execute at the end of each iteration. These UDFs integrate the mass flow rates in both the liquid and vapor regions and compare the two. A new pressure gradient and vapor phase source term is then proposed for the next iteration based on a certain algorithm. The iterations stop when the vapor flow rate and the liquid flow rate are close enough to be regarded equal. The tolerance for integrated mass flow rate is 0.01%. A program listing for the UDFs used in this simulation can be found in Appendix A.

For different film thicknesses, a series of simulations were done in FLUENT to find the relations between the film thickness and the mass flow rate and the pressure gradients in the vapor phase. These relations are used in the comprehensive model which will be introduced later in this chapter.

4.7.4 Two-dimensional simulation results

A typical velocity distribution is illustrated by the three-dimensional surface in Figure 4.6. The non-dimensional film thickness is 0.1 as in Figure 4.5. The cross section is cut by the center line and only half of the velocity surface is shown in this figure. As shown in Figure 4.6, the velocity goes to zero on the pipe wall. The vapor and liquid is separated by the interface line shown in the figure. The liquid velocities are all positive, while some of the vapor near the interface is entrained by friction and moves in the direction of liquid flow. The bulk vapor flow still has negative velocity and moves in the opposite direction from the liquid flow.

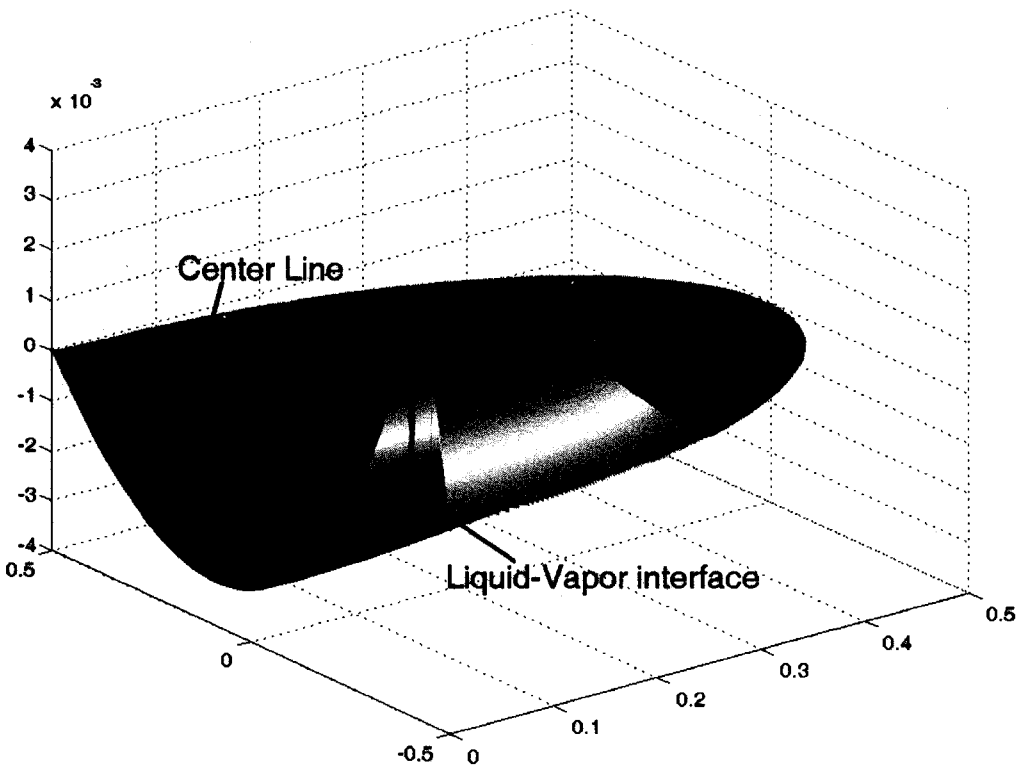

Figure 4.6 Velocity surface

This same geometric configuration is also illustrated with two-phase velocity contours as shown in Figure 4.7. The highest vapor velocity occurs in the center of the vapor core, while the highest liquid velocity occurs near the two-phase interface because it is furthest

from the wall boundary layer. Figure 4.7 (b) shows the positive velocity contours within the cross-section. The vapor phase entrained in the liquid flow direction occupies about the same cross sectional area as the liquid phase does. As shown in Figure 4.7 (c), the negative velocity contours are all distributed in the vapor phase, no liquid is entrained in the vapor flow direction.

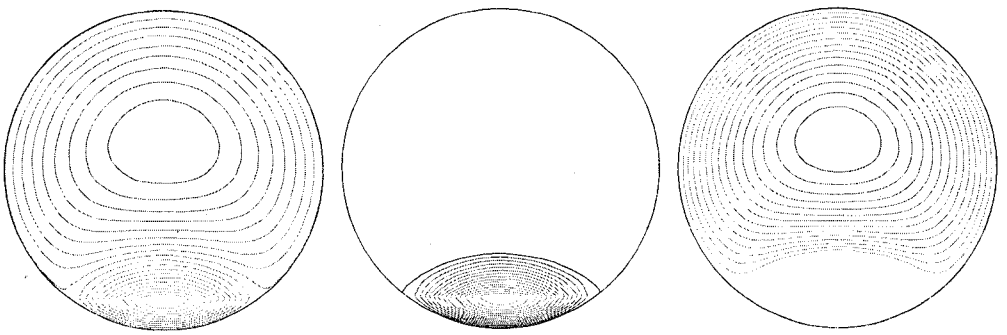

(a) (b) (c)

Figure 4.7 Velocity contours in the cross section

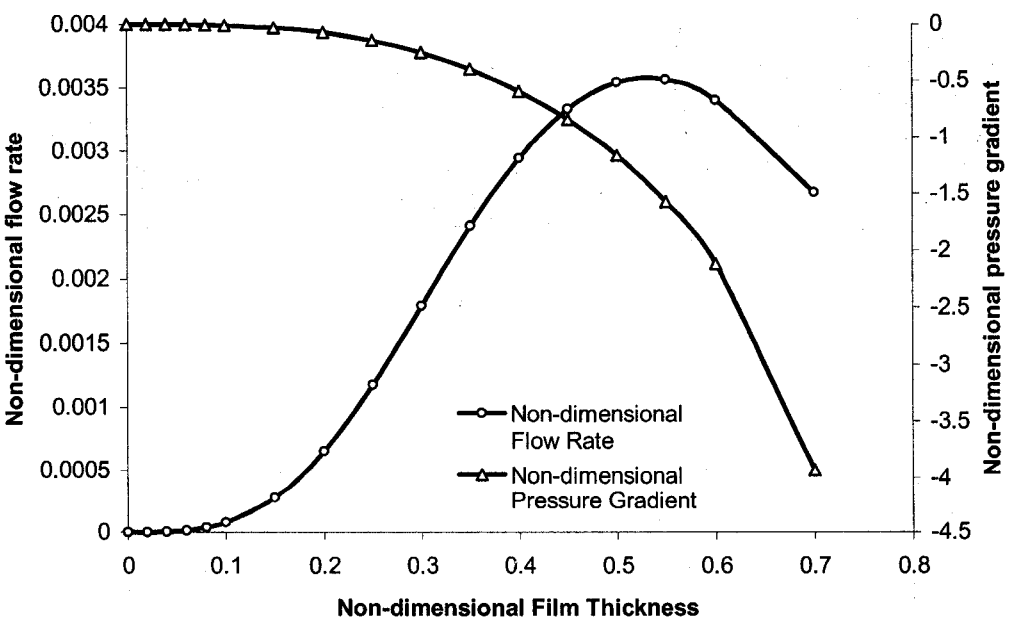

Figure 4.8 Flow rate and pressure gradient from the FLUENT simulation

One important goal of this two-dimensional simulation is to find the relation between the film thickness, the mass flow rate, and the pressure gradient. To that end, a series of simulations were performed at different film thicknesses, the results of which are shown in Figure 4.8. The non-dimensional flow rate and non-dimensional pressure gradient are plotted against the non-dimensional film thickness, with the flow rate scale on the left and the pressure gradient scale on the right. The pressure gradient always increases (in absolute value) as the film thickness increases, while the flow rate reaches a maximum value around a film thickness of 0.55. Beyond this limit, any increase of film thickness can actually result in a decrease in flow rate because the high vapor velocity and interfacial friction make a portion of the liquid flow backward. At higher flow rates the flow limit may occur at a much smaller thickness because of turbulent flow, a wavy interface, or liquid drop entrainment in the vapor flow. The flow situations that occur in a hairpin thermosyphon should only occupy in the leftmost part of the curves in this figure. To ensure accuracy linear interpolation instead of a fitted equation is used in the comprehensive model.

4.8 Solution sequence for the comprehensive model

As discussed previously, the thermosyphon to be modeled is divided into a number of control volumes. Each of these control volumes has a similar structure but different parameters such as vapor velocity, liquid velocity, film thickness, and pressure drop. These control volumes are joined to each other to constitute the condenser, the adiabatic section and the evaporator. The heat transfer and fluid flow calculations are based on these individual control volumes.

To begin, a tentative working temperature is calculated based on the mean temperature of the condenser wall and the evaporator wall. This tentative working temperature is assigned to each control volume, together with a tentative heat transfer coefficient. The heat flux and mass source in each control volume can be determined based on the fixed wall temperature and the tentative parameters for the working fluid. The mass source in

each control volume can be added to the condensate flowing through and accumulating throughout the entire condenser. There is no heat transfer or phase change in the adiabatic section, thus the mass flow rate in each of the control volumes in this section remains constant. Due to evaporation, the mass source term of the liquid phase in the evaporator is a negative number. Based on the mass flow rate in each control volume, the condensate film thickness and the pressure gradient in the vapor flow can also be determined using the relations determined via the FLUENT simulation introduced in section 4.7.4. Then the liquid mass flow rate into the liquid pool is compared with the vapor mass flow rate out of the liquid pool. Generally, these two mass flow rates are not equal at the beginning, which also indicates the overall heat flux in the condenser and the evaporator is not equal.

At this point, a new working temperature has to be proposed based on the heat transfer difference between the evaporator and the condenser. The new working temperature induces a new set of heat transfer parameters in each control volume. This temperature shift will also have a large impact on the performance ratio between the condenser and the evaporator. After several iterations, the right working temperature will finally be reached, which also determine the film thickness distribution, the temperature distribution and all the other flow and thermal parameters. At this point, all of the governing equations including mass conservation, momentum conservation, and energy conservation are satisfied together with all the boundary conditions. The parameters obtained for each control volume constitute the solution to the original modeling problem. The solution process is detailed in the flow chart given in Figure 4.9.

This model is realized with an object-orient C++ program developed in Borland Turbo C++. A list of the program is given in Appendix B.

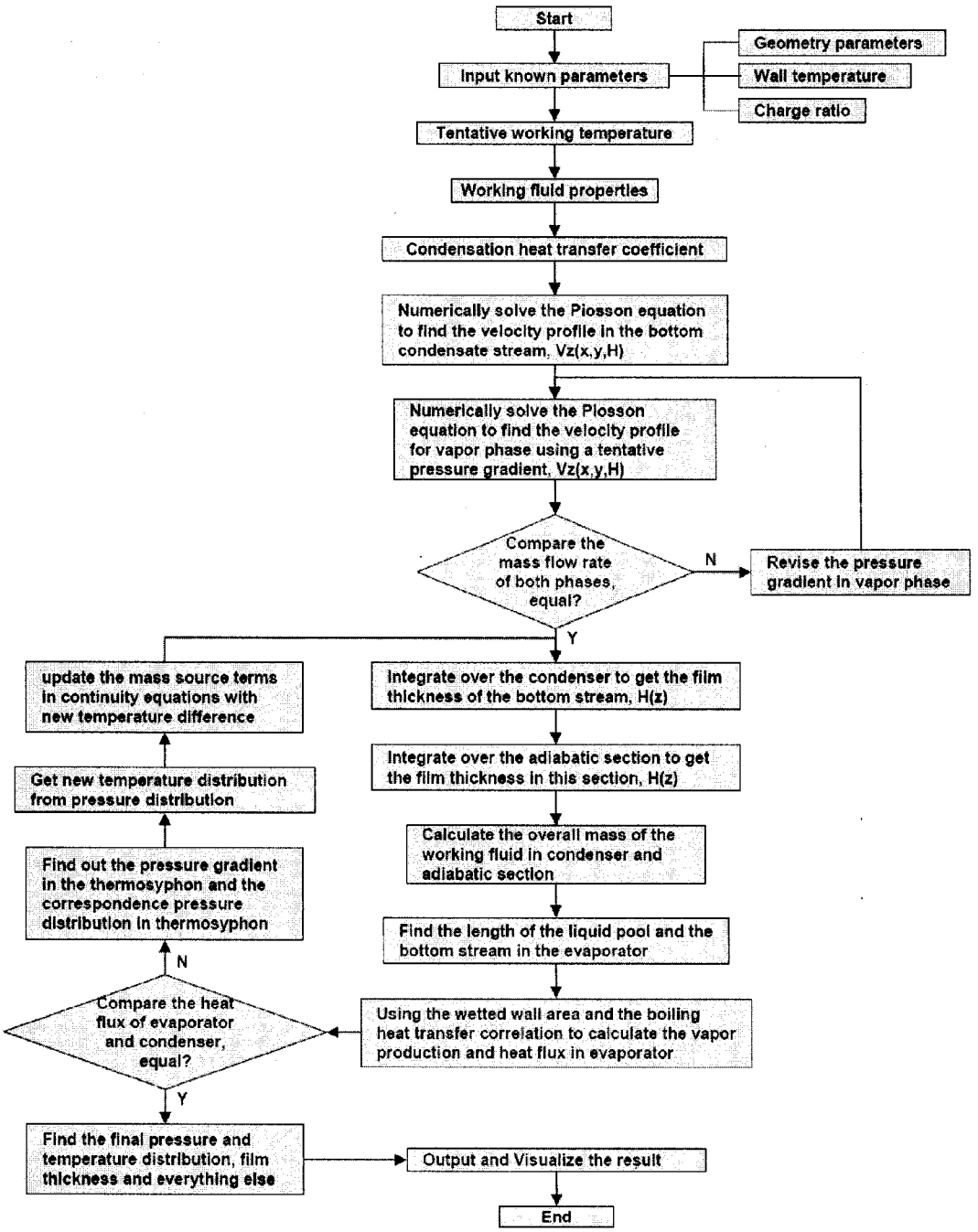

Figure 4.9 Solving flow chart

4.9 References

[1] Bejan, A. (1993). Heat Transfer. New York, John Wiley & Sons, Inc.

[2] Chen, J. C. (1966). "Correlation for Boiling Heat Transfer to Saturated Fluids in Convective Flow." Industrial & engineering chemistry process design and development **5**(3): 322-329.

[3] Forster, H. K. and N. Zuber (1955). "Dynamics of vapor Bubbles and boiling heat transfer." Journal of AIChE **1**(4): 531-535.

[4] Gungor, K. E. and R. H. S. Winterton (1986). "A General Correlation for Flow Boiling in Tubes and Annuli." International Journal of Heat and Mass Transfer **29**(3): 351-358.

[5] Gungor, K. E. and R. H. S. Winterton (1987). "Simplified General Correlation for Saturated Flow Boiling and Comparisons of Correlations with Data." Chemical Engineering Research & Design **65**(2): 148-156.

[6] Kandlikar, S. G. (1990). "A General Correlation for Saturated 2-Phase Flow Boiling Heat-Transfer inside Horizontal and Vertical Tubes." Journal of Heat Transfer-Transactions of the ASME **112**(1): 219-228.

[7] Liu, Z. and R. H. S. Winterton (1991). "A General Correlation for Saturated and Subcooled Flow Boiling in Tubes and Annuli, Based on a Nucleate Pool Boiling Equation." International Journal of Heat and Mass Transfer **34**(11): 2759-2766.

[8] Park, C. Y. and P. S. Hrnjak (2005). "Flow boiling heat transfer of CO2 at low temperatures in a horizontal smooth tube." Journal of Heat Transfer-Transactions of the ASME **127**(12): 1305-1312.

[9] Park, C. Y. and P. S. Hrnjak (2007). "CO2 and R410A flow boiling heat transfer, pressure drop, and flow pattern at low temperatures in a horizontal smooth tube." International Journal of Refrigeration-Revue Internationale Du Froid **30**(1): 166-178.

[10] Steiner, H., A. Kobor, et al. (2005). "A wall heat transfer model for subcooled boiling flow." International Journal of Heat and Mass Transfer **48**(19-20): 4161-4173.

[11] Thome, J. R. and J. El Hajal (2004). "Flow boiling heat transfer to carbon dioxide: general prediction method." International Journal of Refrigeration-Revue Internationale Du Froid **27**(3): 294-301.

[12] Yun, R., Y. Kim, et al. (2005). "Convective boiling heat transfer characteristics of CO2 in microchannels." International Journal of Heat and Mass Transfer **48**(2): 235-242.

[13] Zhang, W. Z., T. Hibiki, et al. (2005). "Correlation for flow boiling heat transfer at low liquid Reynolds number in small diameter channels." Journal of Heat Transfer-Transactions of the ASME **127**(11): 1214-1221.

Chapter 5 Modeling of an inclined thermosyphon condenser[1]

5.1 Abstract

Two-phase closed thermosyphons are widely used to protect man-made infrastructure and underlying permafrost in Arctic regions. Because of the particular working conditions, the thermosyphons often operate with limited heat fluxes and inclined geometries. These conditions have important impacts on the heat transfer processes within the thermosyphon. A numerical model is developed to predict the steady-state performance of an inclined thermosyphon condenser with carbon dioxide used as the working fluid. A pseudo-one-dimensional numerical simulation with a two-dimensional cross sectional flow simulation is developed as part of the solution process. The simulation results are compared with experimental data and show good agreement.

5.2 Introduction

Two-phase closed thermosyphons are highly efficient heat transfer devices working under the assistance of gravity. The evaporation, condensation, and circulation processes of the working fluid within the thermosyphon are the main reasons for their unique properties including high heat transfer performance, passive operation, and the thermal diode effect. Since the 1970's, thermosyphons have been used in many arctic geotechnical applications and have been studied extensively.

As a result of rapid development in the Arctic and the potential threat of global warming, thermosyphon applications in arctic engineering have received a lot of attention during the last late 20 years. In arctic engineering applications, the use of thermosyphons is motivated by the thermal diode effect. This effect enhances the heat loss from the permafrost layer beneath infrastructure to the cold winter air, while not increasing the heat gain during summer. The overall effect of the thermosyphon operation is a net cooling of the permafrost layer which helps maintain the permafrost in the frozen state.

---

[1] Xu, J. and D.J. Goering, (2008). Modeling of an inclined thermosyphon condenser. Prepared for submission to International Journal of Heat and Mass Transfer.

An application of "hairpin" thermosyphons to protect roadway embankments located in areas of warm permafrost is described by J. Xu and D. Goering [23].

Hairpin thermosyphons represent a new configuration for thermosyphons with carbon dioxide used as the working fluid. As shown in Figure 5.1, both the evaporator and condenser are buried under the road surface at shallow inclination angles. In steady-state operation, the working fluid in the evaporator absorbs heat from surrounding soil and evaporates. The vapor rises up to the condenser, where it cools and condenses back into liquid. The condensate flows downward toward under the action of gravity and flows back to the evaporator to complete the circulation loop.

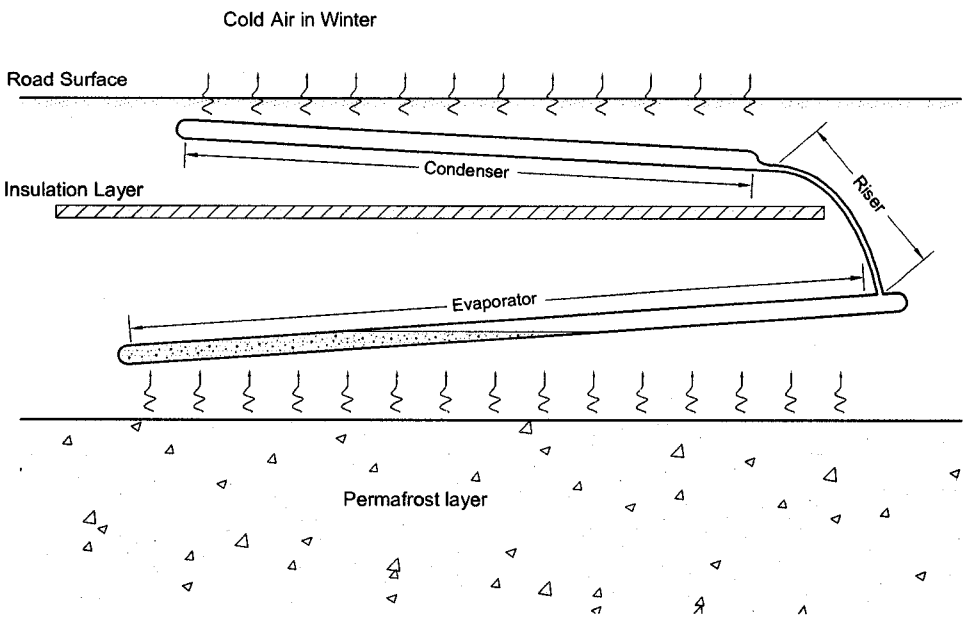

Figure 5.1 Inclined two-phase closed thermosyphon

The particular features of the hairpin thermosyphon and the special operating conditions have a significant impact on the internal processes and overall performance of the thermosyphon condenser. Unlike vertical condensers, the shallow inclination angle of the hairpin thermosyphon condenser helps to limit the condensate film thickness by

draining it into a rivulet on the bottom of the pipe. It also reduces the driving force of the liquid phase since only the longitudinal component of the gravity is acting as the driving body force to help condensate return to evaporator. Another unique feature this condenser configuration is a limited heat flux. Under typical working conditions in arctic applications, the overall heat flux through the thermosyphon is limited by the surrounding soil. This low heat flux may influence the internal phase change heat transfer processes. The carbon dioxide working fluid has a relatively low critical point ($T_{cr} = 31\,^{\circ}\mathrm{C}$, $p_{cr} = 7.38$ MPa) compared to the working condition of the hairpin thermosyphon. Thus the thermophysical properties of the working fluid are subject to relatively dramatic change over the operating range. Most of these unique aspects of the hairpin thermosyphon condenser have not been carefully studied before. The object of this study is to develop a numerical model to simulate the overall heat transfer performance of the thermosyphon condenser and improve the understanding of the condensation process within it.

Due to the complexity of the condensation process, thermosyphon models typically employ significant assumptions to simplify the problem, such as steady state operation, vertical geometry, laminar liquid film, negligible compressibility, negligible sensible heat related to sub-cooling, negligible pressure drop in liquid film, etc. The first thermosyphon model was developed by Y. Lee and U. Mital [14] based on a dimensional analysis. A "Lumped parameter" thermosyphon model was created by F. Dobran [10; 9] and was later improved by C. Casarosa [2] with consideration given to the liquid entrainment in the vapor core. J. G. Reed [16] proposed a "control volume" model as a summary of his Ph.D. research [15]. This control volume method was very successful in reducing the complexity of mathematical formulation and was adopted by C. Harley and H. Faghri [12] in their modeling. However, this control volume method can only describe the overall performance of the thermosyphon; it is still difficult to determine the local details of flow and heat transfer within the thermosyphon.

Numerical methods are better able to solve the complex governing equations confronted in thermosyphon modeling and reveal more of the flow and thermal details inside the thermosyphon. In 1974, C. Tien and A. Rohani [20] constructed the first numerical model for the vapor flow in a thermosyphon, examining the relation between the heat transfer performance and the vapor pressure drop. In 1994, Z. Zuo [24] adapted J.G. Reed's [15; 16] control volume method in a numerical model, in which the liquid-film momentum advection and axial normal stress in the counter current two phase flow were considered. Z. Zuo [25] also extended his numerical model to inclined thermosyphons, in which the inclination angle was classified into 3 different ranges depending on how the liquid pool covered the bottom of the thermosyphon pipe. An inclination angle of 30°-45° was claimed to yield the highest flooding limit. Zhou's work has been the only comprehensive model dealing with inclined thermosyphons. Although not many models have been developed specifically for the condenser only, most of the methods used in thermosyphon modeling are generally transferable to a condenser model.

The condensation process is one of the key reasons for the high heat transfer performance of the thermosyphon condenser. The only successful condensation modeling is in the area of laminar filmwise condensation first conducted by Nusselt. Nusselt's theory was improved by W. Rohsenow [17], E. Sparrow [18], and more recently by M. Chen [5], T. Spendel [19], and S. Chen et al. [6]. It was also extended to geometries other than the flat plate by V. Dhir and J. Lienhard [8] and W. Kamminga [13]. More related to thermosyphon operation, condensation inside a pipe with a vertical or inclined orientation has been another active research area. J.C. Chato [3; 4] developed a momentum-energy integral method for the laminar condensate forming on the pipe wall and on the bottom condensate flow in inclined tubes. U. Gross [11] developed a semi-empirical correlation for reflux condensation based on 66 experimental studies. J. Wang and Y. Ma's [21] study showed that the inclination angle has a notable influence on the condensation coefficient. Although a lot of studies have been conducted since Nusselt's theory, "the field of condensation is at present more of an art than a science and the subject remains, and will remain for some time to come, largely empirical [7]."

The present model is a pseudo-1D model based on a 2D analysis of counter-current two-phase flow in each cross section. This model provides a way to study the thermosyphon condenser's overall performance as well as the parameter variations along the condenser pipe.

5.3 Theoretical model

In the formulation presented below, the condenser is divided into a number of control volumes. As shown in Figure 5.2, the liquid flow occupies a small fraction of the cross-section at the bottom of the pipe. Under the action of gravity it flows in the positive z direction. The vapor phase, on the other hand, flows in the opposite direction and occupies the upper portion of the flow channel. Under steady state operation, the mass flow rates of the liquid and vapor phase are equal at any cross section of the condenser. H is defined as the film thickness of the liquid stream on the bottom, and is a function of the z coordinate.

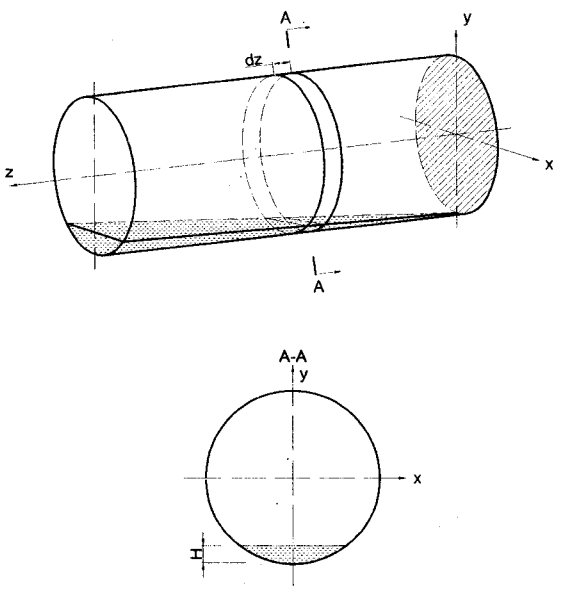

Figure 5.2 A control volume in the thermosyphon

The general governing equations for an incompressible Newtonian fluid are as follows.

Mass conservation:

$$\frac{\partial \rho}{\partial t} + \nabla \cdot (\rho \vec{V}) = \dot{M} \tag{5.1}$$

Momentum conservation:

$$\frac{D\vec{V}}{Dt} = \vec{F} - \frac{1}{\rho}\nabla p + \upsilon \nabla^2 \vec{V} \tag{5.2}$$

Energy conservation:

$$\frac{DT}{Dt} = \alpha \nabla^2 T + \frac{1}{\rho c_p}\Phi \tag{5.3}$$

The assumptions made in the initial formulation are that the vapor is saturated, that the Mach number of the vapor flow is low enough that compressibility effects in the vapor phase are negligible, and that the entrainment of liquid droplets in the vapor phase is negligible. These assumptions are well justified in many systems of practical interest. In addition to these basic assumptions, more assumptions are necessary to further simplify the problem:

1. A steady state operation;
2. A long pipe, $L >> D$;
3. For both liquid and vapor, $w >> u \sim v \sim 0$;
4. The liquid film thickness varies slowly in the z direction, $\frac{dH}{dz} << 1$;
5. For both liquid and vapor, $\frac{\partial^2 w}{\partial z^2} << \frac{\partial^2 w}{\partial x^2} \sim \frac{\partial^2 w}{\partial y^2}$;
6. In liquid film, gravity is the dominant body force;
7. Both liquid and vapor flow is laminar.

In most regions of a long condenser pipe, the velocity direction closely parallels the pipe axis (z-axis), and the velocities in x and y direction can be regarded as negligible without introducing significant errors. Another simplification made from the "long pipe"

assumption is that the mass condensation at a specific location is much smaller than the bulk mass flow rate in the z-direction. The mass transfer between the liquid and vapor phases can be considered a uniform mass source distributed over the cross section. What's more, this small mass source also indicates a small flow rate gradient in the z-direction (or a small z-velocity gradient). Under no-slip boundary conditions, the velocity gradients in x and y directions are relatively large, and the velocity gradient in z-direction can thus be considered negligible.

Utilizing the above assumptions, the mass conservation can be written as:

Liquid film: $$\rho_l\left(\int_{z+dz} w_l dA_l - \int_z w_l dA_l\right) = \dot{m}_l C(z)dz \tag{5.4}$$

Vapor core: $$\rho_v\left(\int_{z+dz} w_v dA_v - \int_z w_v dA_v\right) = \dot{m}_v C(z)dz \tag{5.5}$$

Because of negligible velocity in the x and y direction, only the z-momentum equation (M_z) needs to be considered. It takes a simplified form:

Liquid film: $$0 = \frac{g\sin\theta}{\upsilon_l} + \left(\frac{\partial^2 w_l}{\partial x^2} + \frac{\partial^2 w_l}{\partial y^2}\right) \tag{5.6}$$

Vapor Core: $$0 = -\frac{1}{\rho_v \upsilon_v}\frac{\partial p}{\partial z} + \left(\frac{\partial^2 w_v}{\partial x^2} + \frac{\partial^2 w_v}{\partial y^2}\right) \tag{5.7}$$

According to A. Bejan [1], the mass conservation and momentum conservation equations, in forced convection configurations, are sufficient for determining the velocity distribution within the flow field. In such cases, the fluid temperature distribution can be determined as an afterthought, by using the just-determined velocity distribution and the energy equation.

For the energy conservation equation, both the condensation heat transfer in the condenser and the evaporation heat transfer in the evaporator can be described with empirical correlations. The energy conservation can be simplified as

$$q(z) = h(z)\Delta T(z) \tag{5.8}$$

To complete the governing equations, supplemental relations for phase change and heat transfer are required:

In the liquid: $$\dot{m}_l(z) = \frac{q(z)}{L} \tag{5.9}$$

In the vapor: $$\dot{m}_v(z) = -\dot{m}_l(z) \tag{5.10}$$

By combining Equation (4.13) with Equations (4.14) and (4.15), the energy conservation can also be expressed as

In the liquid: $$\dot{m}_l(z) = \frac{h(z)\Delta T(z)}{L} \tag{5.11}$$

In the vapor: $$\dot{m}_v(z) = -\frac{h(z)\Delta T(z)}{L}. \tag{5.12}$$

5.3.1 Boundary conditions

No-slip boundary conditions as given in Equations (4.18) and (4.19) are applied to the wall boundaries. No-slip and force balance boundary conditions given by Equations (4.20) to (4.22) are applied to the liquid-vapor interface.

In the liquid: $w_l = 0$ at pipe wall (5.13)

In the vapor: $w_v = 0$ at pipe wall (5.14)

On the liquid-vapor interface

$$w_l = w_v \tag{5.15}$$

$$\mu_l \frac{\partial w_l}{\partial x} = \mu_v \frac{\partial w_v}{\partial x} \tag{5.16}$$

$$\mu_l \frac{\partial w_l}{\partial y} = \mu_v \frac{\partial w_v}{\partial y} \tag{5.17}$$

To focus on the internal processes of the condenser, temperature boundary conditions as given in Equation (4.23) are adopted for the condenser wall. A pressure boundary condition as given by Equation (5.19) is used at the entrance of the condenser.

$$T_{w,c} = T_0 \tag{5.18}$$

$$p_{inlet} = p_0 \tag{5.19}$$

The governing Equations (4.11) to (4.15) and boundary conditions, (4.18) to (5.19), represent a complete quasi one-dimensional model of the inclined condenser with a two-dimensional analysis of the longitudinal velocity distribution in the cross section.

5.3.2 Non-dimensional Equations

The following non-dimensional variables are introduced to put the governing equations in non-dimensional form:

$$\begin{aligned}
x^* &= \frac{x}{D} & y^* &= \frac{y}{D} & z^* &= \frac{z}{D} \\
\rho_l^* &= \frac{\rho_l}{\rho_l} = 1 & \rho_v^* &= \frac{\rho_v}{\rho_l} & \mu_l^* &= \frac{\mu_l}{\mu_l} = 1 \\
\mu_v^* &= \frac{\mu_v}{\mu_l} & w_l^* &= \frac{w_l}{w_0} & w_v^* &= \frac{w_v}{w_0} \\
\dot{m}_l^* &= \frac{\dot{m}_l c_{p,l} D}{k_l} & \dot{m}_v^* &= \frac{\dot{m}_v c_{p,l} D}{k_l} & T^* &= \frac{T - T_0}{T_{w,e} - T_{w,c}} \\
h^* &= \frac{h}{c_{p,l} w_0 \rho_l} & C^* &= \frac{C}{D} & m^* &= \frac{m}{\rho_l D^3}
\end{aligned} \tag{5.20}$$

where $w_0 = \dfrac{D^2 \rho_l g \sin\theta^2}{\mu_l}$ is the characteristic velocity, derived from the force balance of gravity and wall friction in liquid phase.

The governing equations can be written in dimensionless form using the above variables as follows:

Mass conservation:

$$\rho_l^* \int_{z^*+dz^*} w_l^* dA_l^* - \int_{z^*} w_l^* dA_l^* = \dot{m}_l^* C^* dz^* \tag{5.21}$$

$$\rho_v^* \int_{z^*+dz^*} w_v^* dA_v^* - \int_{z^*} w_v^* dA_v^* = \dot{m}_v^* C^* dz^* \tag{5.22}$$

Momentum conservation:

$$\mu_l^* \left(\frac{\partial^2 w_l^*}{\partial x^{*2}} + \frac{\partial^2 w_l^*}{\partial y^{*2}} \right) = \Phi_l^* \tag{5.23}$$

$$\mu_v^* \left(\frac{\partial^2 w_v^*}{\partial x^{*2}} + \frac{\partial^2 w_v^*}{\partial y^{*2}} \right) = \Phi_v^* \tag{5.24}$$

Energy conservation:

$$\dot{m}_l^* = -\dot{m}_v^* = Ja \cdot Nu \cdot (T^* - T_w^*) \tag{5.25}$$

The boundary conditions can also be put in non-dimensional forms as follows:

In the liquid $w_l^* = 0$ at the wall (5.26)

In the vapor $w_v^* = 0$ at the wall (5.27)

On the liquid-vapor interface

$$w_l^* = w_v^* \tag{5.28}$$

$$\mu_l^* \frac{\partial w_l^*}{\partial x^*} = \mu_v^* \frac{\partial w_v^*}{\partial x^*} \tag{5.29}$$

$$\mu_l^* \frac{\partial w_l^*}{\partial y^*} = \mu_v^* \frac{\partial w_v^*}{\partial y^*} \tag{5.30}$$

5.4 Solution method

5.4.1 Condensation heat transfer

In the condenser of hairpin thermosyphons, the condensation is most likely filmwise due to the small surface tension of CO_2. This was also verified by the lab experiment described in Chapter 3. Most of the existing experimental correlations and theoretical solutions are not able to predict the heat transfer performance when the condensation heat

flux is extremely small and the working fluid is operating near its critical point. As discussed in Chapter 3, it is very likely that condensation under these small heat flux conditions is not strong enough to be the dominant heat transfer mechanism. When transitioning from forced convection to filmwise condensation, the convection heat transfer may still serve as a key mechanism even though filmwise condensation occurs at the same time. The experimental correlation developed by J. Xu and D. Goering [22], Equation (5.31), can predict this heat transfer behavior fairly well, so this correlation will be used as part of the condenser modeling.

$$Nu = 0.642 Re_v^{0.867} Pr_v^{1.729} + 0.0133 Ra^{0.0298} Ja^{-1.795} \tag{5.31}$$

5.4.2 Flow simulation

The liquid and vapor flow within the condenser can be considered as forced convection. The governing equations for both liquid and vapor phase are Poisson equations, which are relatively simple, it is the geometry that complicates the problem. Numerical simulation with a commercial CFD code, FLUENT, was used in solving this two-dimensional problem.

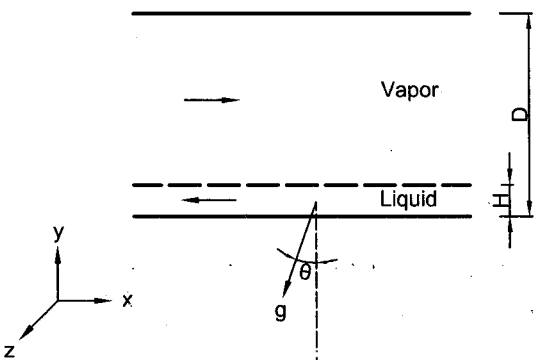

Figure 5.3 One-dimensional countercurrent problem

The numerical solution of the Poisson equations in FLUENT can be verified by simulating a simpler one-dimensional problem and comparing with the analytical solution. This one-dimensional problem is illustrated in Figure 5.3. The distance between the top

and bottom wall is D, the liquid film has a thickness of H, and the flow channel is infinite in the z direction. The liquid and vapor flow have exactly the same mass flow rate, but in opposite directions. The longitudinal component of gravity is the dominant driving force for the liquid phase, while the pressure gradient drives the vapor phase. The countercurrent flow is balanced, and there is no acceleration in either the liquid or vapor phases. The velocity gradient in the x direction is zero. Thus the problem is one-dimensional with velocity changing only in the y direction. The governing equations are as follows:

$$\dot{m}_l = -\dot{m}_v \tag{5.32}$$

$$\mu_l \frac{\partial^2 w_l}{\partial y^2} = \rho_l g \sin(\theta) = \Phi_l \tag{5.33}$$

$$\mu_v \frac{\partial^2 w_v}{\partial y^2} = \frac{\partial p_v}{\partial z} = \Phi_v \tag{5.34}$$

The boundary conditions are:

$$w_l = 0 \qquad \text{at } y = 0 \tag{5.35}$$

$$w_i = w_v \qquad \text{at } y = H \tag{5.36}$$

$$\mu_l \left.\frac{dw_l}{dy}\right|_H = -\mu_v \left.\frac{dw_v}{dy}\right|_H \qquad \text{at } y = H \tag{5.37}$$

$$w_v = 0 \qquad \text{at } y = D \tag{5.38}$$

This problem has an analytical solution given by Equation (5.39) and Equation (4.58).

$$w_l = y^2 \frac{\Phi_l\left(H\mu_v - \mu_l H + \mu_l D\right)}{2\mu_l D\left(HD\mu_v - HD\mu_l + D^2\mu_l\right)} + y\frac{\Phi_l\left(2H^2\mu_l - H^2\mu_v - 2HD\mu_l\right) + \Phi_v\mu_l\left(2HD - H^2 - D^2\right)}{2\mu_l\left(H\mu_v - H\mu_l + D\mu_l\right)} \tag{5.39}$$

$$w_v = y^2 \frac{\Phi_v\left(H\mu_v - H\mu_l + D\mu_l\right)}{2\mu_v\left(H\mu_v - H\mu_l + D\mu_l\right)} + y\frac{\left(\Phi_l H^2\mu_v - 2\Phi_v H^2\mu_v + \Phi_v H^2\mu_l - \Phi_v D^2\mu_l\right)}{2\mu_v\left(H\mu_v - H\mu_l + D\mu_l\right)} + \frac{H^2 D\left(2\Phi_v\mu_v - \Phi_l\mu_v - \Phi_v\mu_l\right) + \Phi_v HD^2\left(\mu_l - \mu_v\right)}{2\mu_v\left(H\mu_v - H\mu_l + D\mu_l\right)} \tag{5.40}$$

In Figure 5.4, the results from the numerical simulation are compared with the analytical solution for the case with a $0.1D$ film thickness. The diagram shows the velocity distribution in one cross-section from both the analytical solution and the FLUENT simulation. The liquid-vapor interface is indicated by a horizontal solid line and the cross-section is indicated by a vertical dashed line. The y-axis is the vertical position in the flow channel. The x-axis shows the non-dimensional velocity magnitude.

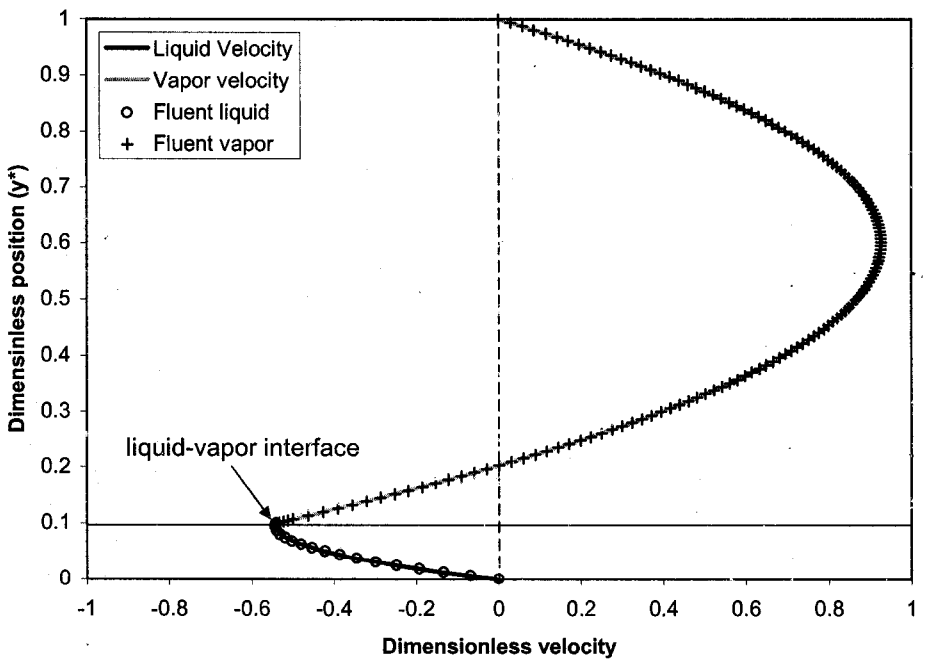

Figure 5.4 One-dimensional simulation in FLUENT with analytical solution

Obviously, the FLUENT simulation matches the analytical solution very well. Therefore, it is reasonable to believe that numerical simulation in FLUENT can also provide an accurate prediction of the velocity distribution for the two-dimensional problem.

For the two-dimensional FLUENT simulation, a representative cross-section (with a 0.1D film thickness) of the circular pipe is shown in Figure 5.5 with the generated mesh. A fine boundary mesh is used near the wall area and the liquid-vapor interface to capture more details where high velocity gradients may exist.

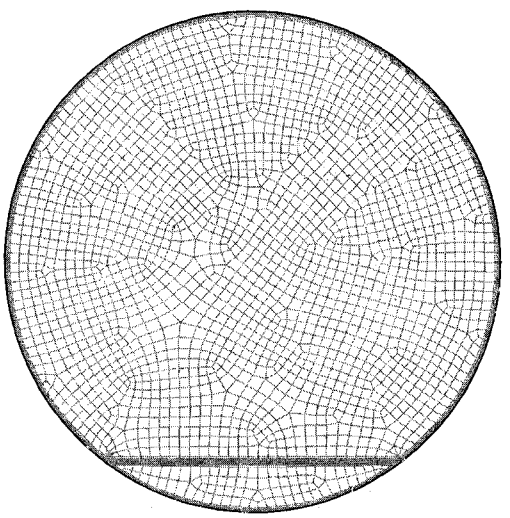

Figure 5.5 Mesh generated in Gambit for a two-dimensional pipe cross section

An iterative method is used in solving this problem. The source term in the liquid-phase is known for any given film thickness, while a tentative pressure gradient can be used as the source term in the vapor phase. Both the liquid and vapor equations can be solved together, and the total flow rate for each phase can then be found by integrating over their own portion of the cross section. According to the steady state assumption and mass conservation, at any cross-section of the thermosyphon the mass flow rate of the liquid film and the vapor core should be equal in magnitude and opposite in direction. If the integrated flow rates of the liquid phase and vapor phases are not equal, modifications can be made to the tentative pressure gradient in the vapor phase. After a number of

iterations, the integrated flow rates in both phases become close enough to be considered equal. This strategy is used to solve Equations (4.30) and (4.31) for a particular film thickness (H^*). In order to form a complete solution for the entire condenser, these equations need to be solved for different film thicknesses. Ultimately, the velocity profile, flow rate and other flow characteristics can be regressed as functions of film thickness (H^*).

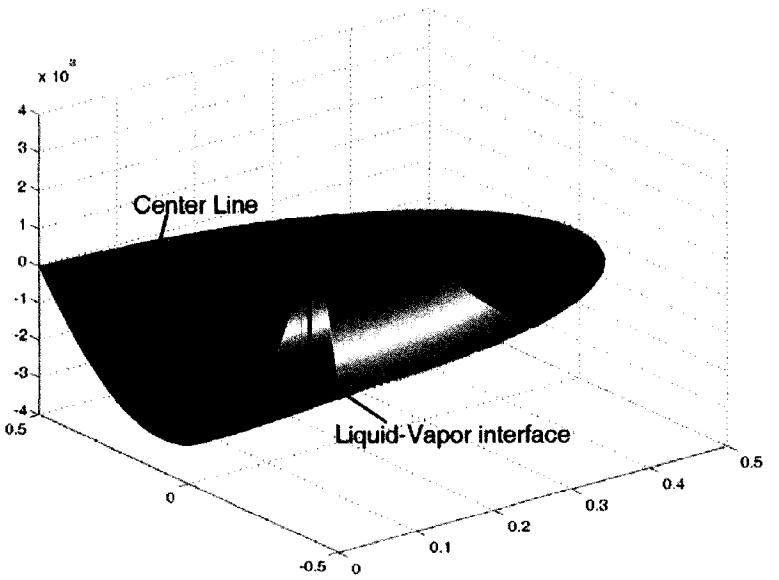

Figure 5.6 Velocity surface

The velocity distribution across the section is illustrated by the three-dimensional surface in Figure 5.6, for a $0.1D$ film thickness case. Only half of the cross section is shown to reveal the velocity profile on the center line. Obviously, the liquid velocities are all positive, while some of the vapor near the liquid-vapor interface is entrained by friction and moves in the direction of liquid flow. The bulk vapor flow still has negative velocity and moves in the opposite direction from the liquid flow.

The dependence of the mass flow rate and the pressure gradient on the film thickness is shown in Figure 5.7, with the flow rate scale on the left and the pressure gradient scale on

the right. As shown in Figure 5.7, the pressure gradient always increases (in absolute value) as the film thickness increases, while the flow rate reaches a maximum value around a film thickness of 0.55. Beyond this limit, any increase of film thickness can actually result in a decrease in flow rate because the high vapor velocity and interfacial friction make a portion of the liquid flow backward. In reality, the flow limit can actually happen at a much smaller film thickness because of turbulent flow, wavy interface, and liquid drop entrainment in the vapor flow. The flow that occurs in a hairpin thermosyphon should only happen in the leftmost part of the curves in this figure. To ensure accuracy linear interpolation instead of a fitted equation is used in the comprehensive model.

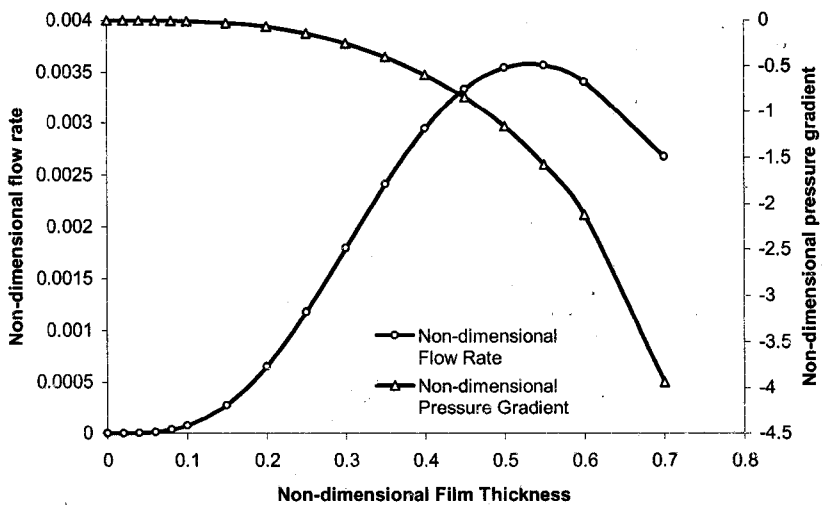

Figure 5.7 Flow rate and pressure gradient vs. film thickness

5.4.3 Solution sequence for the condenser model

As discussed previously, the condenser is divided into a number of control volumes. Each of these control volumes has a similar structure but different parameters such as vapor velocity, liquid velocity, film thickness, pressure drop, and temperature profiles. These control volumes are joined to each other to constitute the condenser. All the heat transfer and fluid flow calculations in this pseudo-1D model are based on these individual control volumes.

At the beginning, a tentative operating temperature is calculated based on the operating pressure. This tentative operating temperature is assigned to each control volume, together with a tentative local heat transfer coefficient. The heat flux and mass source can be determined in each control volume based on the boundary conditions and these tentative parameters for the working fluid. The mass source in both liquid and vapor phases can then be calculated and added to the vapor or liquid flow in each control volume. Based on the mass flow rate in each control volume, the condensate film thickness and the pressure gradient in the vapor flow can also be determined using the relations given in Figure 5.7. This procedure can be repeated based on the new parameters in each of the control volumes. The iterations converge when the parameters in each control volume stop changing in successive iterations. At this point, all of the governing equations and boundary conditions are simultaneously satisfied. The parameters determined for each control volume constitute the solution to the original modeling problem.

5.5 Results and discussions

5.5.1 Details within the thermosyphon

To illustrate the performance of this condenser model, several example simulations were carried out under typical hairpin thermosyphon working conditions. The parameters and boundary conditions used in these simulations are listed in Table 5.1. A summary of the simulation results is given in Table 5.2.

Table 5.1 Known parameters

Parameter	Units	Value
Working fluid	--	CO_2
Inclination angle	°	3.0
Condenser wall temperature	°C	0.0
Condenser diameter	mm	78.0
Condenser wall thickness	mm	5.0
Condenser length	m	0.5
Operating pressure	Pa	3674100

Table 5.2 Summary of modeling results

Parameter	Units	Value
Working temperature	°C	2.0
Working pressure	kPa	3674100
Overall pressure drop	Pa	26.3
Condenser heat rate	W	38.0
Condenser mass flow rate	g/s	0.17
Condenser mass storage	kg	1.0

The Nusselt number in each control volume of the condenser is plotted in Figure 5.8 for steady-state conditions. It shows that the distribution of the local heat transfer coefficient in the condenser is very linear as a function of position within the condenser. The highest heat transfer coefficient occurs at the entrance to the condenser where the vapor velocity is high. At the end of condenser, the vapor velocity is approaching zero and the influence of forced convection is reduced, thus the heat transfer in this portion of the condenser is due to the condensation mechanism characterized by the second term in Equation (5.31).

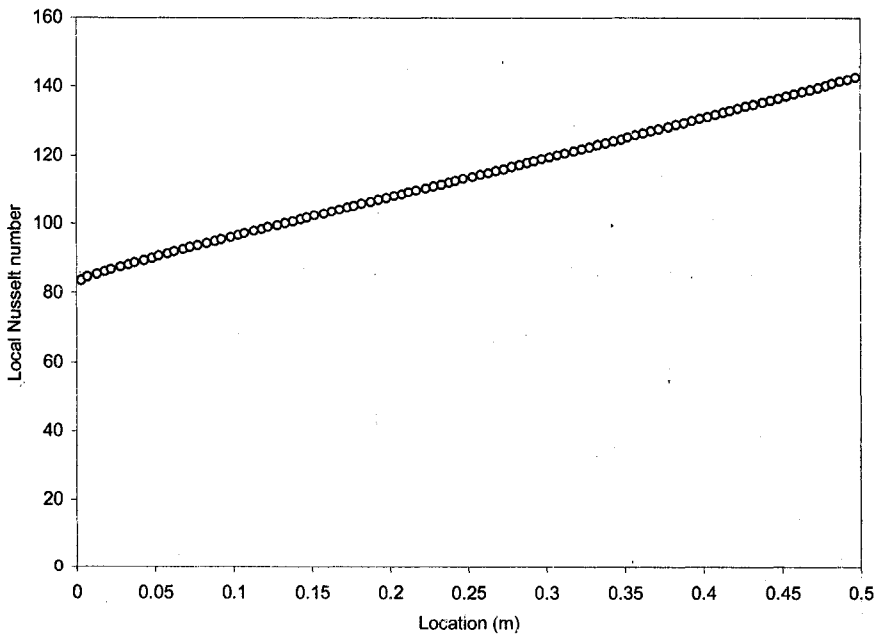

Figure 5.8 Local Nusselt number as a function of position within the condenser

The local heat transfer rate and local condensate film thickness distributions are plotted in Figure 5.9. Just like the heat transfer coefficient in Figure 5.8, the local heat transfer rate distribution is very linear. The condensate stream at the bottom has a zero thickness at the tip of the condenser. As the condensate travels downward along the condenser pipe, more condensate is collected at an increasing rate, which causes the film to get thicker quickly.

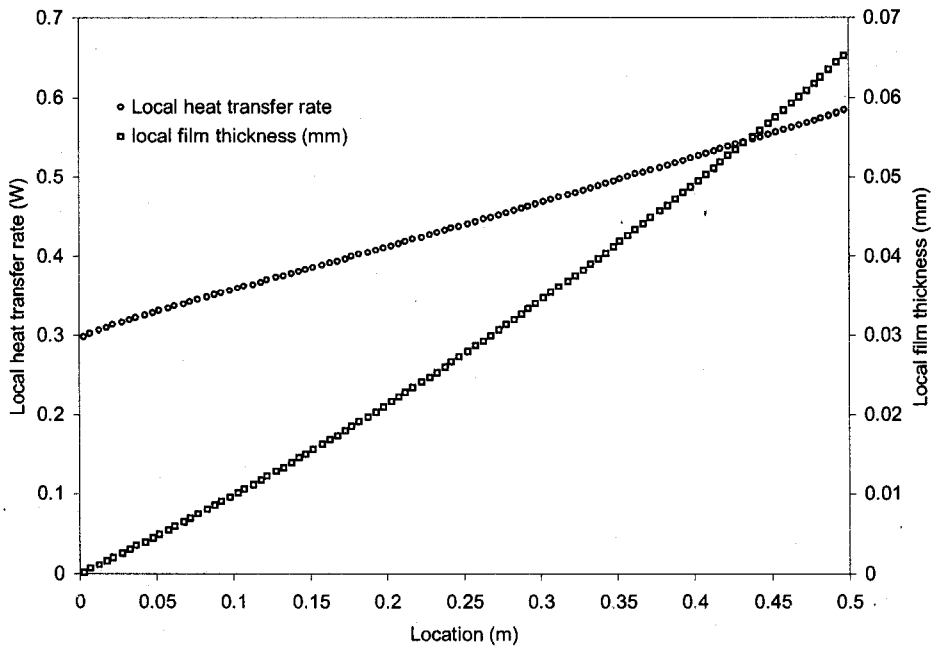

Figure 5.9 Local heat transfer rate and film thickness as a function of position within the condenser

In order to study the impact of operating temperature on the performance of the condenser, simulations are performed at operating temperatures of 0 °C and 25 °C. Results from these simulations are plotted in **Error! Reference source not found.**, with the x-coordinate indicating the temperature difference between the operating temperature and the wall temperature. As the temperature difference increases, the heat transfer rate of the condenser increases. At the operating temperature of 0 °C, the overall heat transfer

performance of the condenser is pretty linear. However, at the higher operating temperature of 25 °C, the condenser shows a non-linear increasing heat transfer rate.

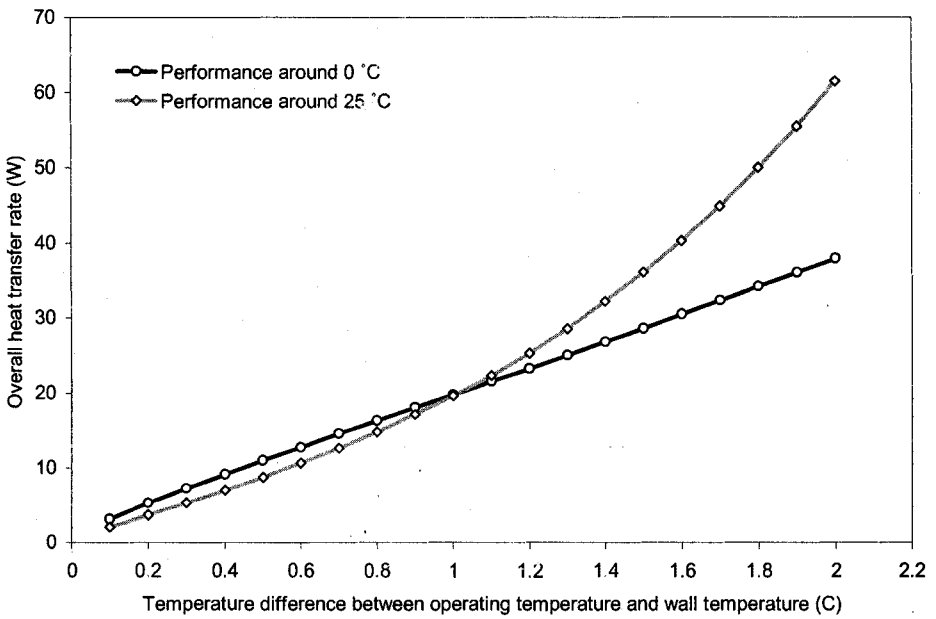

Figure 5.10 Condenser performance at operating temperatures of 0 and 25°C.

The reason for the different performance at different operating temperatures is related to property changes of the working fluid. As mentioned before, carbon dioxide has a relatively low critical point. The critical temperature of carbon dioxide is 31 °C. When near the critical point, the thermophysical properties of carbon dioxide change dramatically with the differences between the liquid and vapor phases diminishing. The latent heat related to phase change also decreases rapidly near the critical point. Once the critical point is reached, the phase change ceases completely and the only heat transfer mechanism is single phase convection. As discussed in Chapter 4 and earlier in this chapter, when the condenser is working at an operating temperature near the critical point, the heat transfer process inside the condenser is determined not only by condensation, but also by single-phase convection. The closer the operating temperature approaches the

critical point, the more important the convection mechanism is. As shown in Figure 5.11, the thermal conductivity and the heat capacity of carbon dioxide increase dramatically when approaching the critical point. These thermophysical property changes enhance the heat transfer by the single phase convection mechanism. It is reasonable to conclude that at the operating temperature of 25 °C, the convection heat transfer mechanism is very important and has a significant influence on the overall heat transfer. For this circumstance, an increase in the temperature difference of the condenser can not only increase the heat transfer driving force, but also increase the heat transfer coefficient. That's why the heat transfer performance at the 25 °C operating temperature is no longer linear.

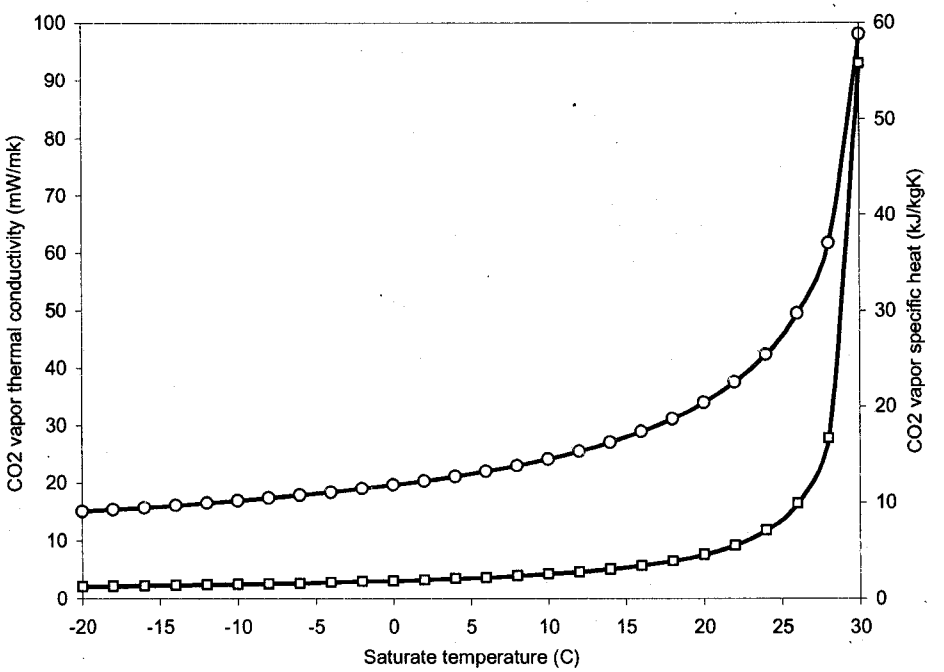

Figure 5.11 Thermal conductivity and specific heat of saturated carbon dioxide vapor

The modeling results are also compared with the lab experiment described in Chapter 4. The current model was used to simulate the 36 experimental conditions described

previously. The overall heat transfer rate of the condenser predicted by the model is compared to that recorded from the experiments in Figure 5.12. Due to limitations of measurement accuracy in the experiment, the experimental data points are somewhat scattered. However, the predictions given by the condenser model agree with the experimental data fairly well.

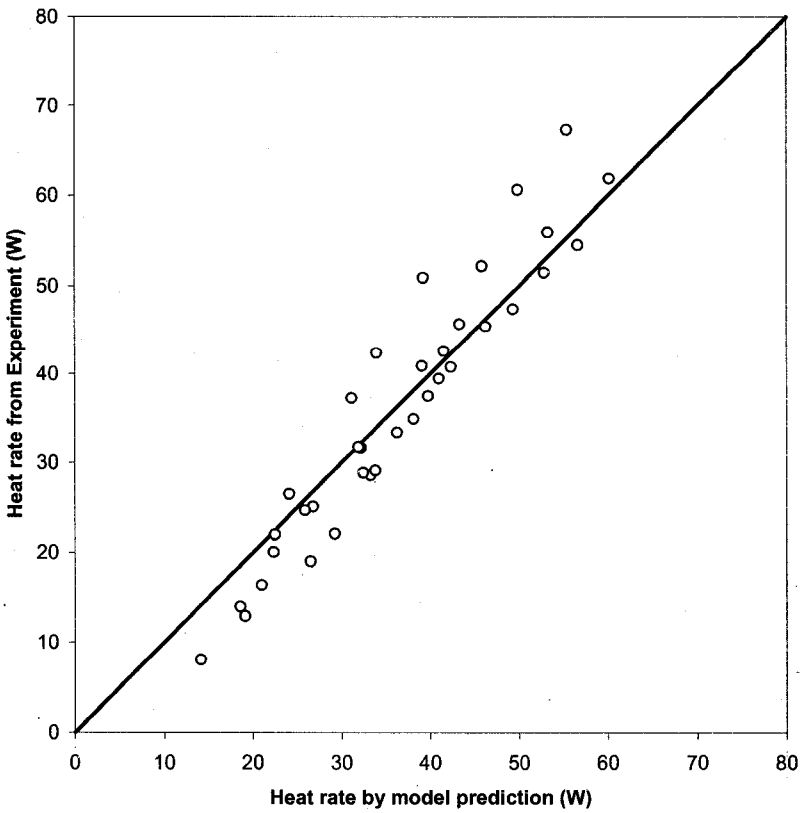

Figure 5.12 Comparison of predicted and measured heat rate in the condenser.

5.6 Conclusions

A quasi one-dimensional model for inclined thermosyphon condensers has been developed to predict heat transfer performance. A 2D numerical analysis is used to determine the two-phase velocity distribution over each pipe cross section and the relations between the vapor pressure gradient, the liquid film thickness, and the

longitudinal mass flow rate. This model uses the condensation heat transfer correlation developed for extremely low heat flux conditions, which make it suitable for predicting the performance of thermosyphon condensers operating under arctic conditions. When the operating temperature approaches the critical point of the working fluid, single-phase convection heat transfer has a significant impact on the overall condenser performance. The comparison of the model prediction and the experimental data shows fairly good agreement over the operating range of the condenser.

5.7 Acknowledgements

This work was supported by Alaska Experimental Program to Stimulate Competitive Research (EPSCoR) and Alaska Department of Transportation & Public Facilities (AKDOT).

5.8 Nomenclature

A	area
$C(z)$	phase change perimeter
D	inner diameter
c_p	specific heat
$\vec{F}$	body force
g	gravity acceleration
H	film thickness
h	heat transfer coefficient
L	latent heat
$\dot{M}$	mass generation
$\dot{m}$	effective mass source in cross section
p	pressure
q	local heat flux
T	temperature
t	time

u velocity in x-direction

$\vec{V}$ velocity vector

v velocity in y-direction

w velocity in z-direction

x x-coordinate

y y-coordinate

z z-coordinate

Greek Symbols

α thermal diffusivity

Δ difference

θ inclination angle of the thermosyphon

Φ dissipation function (including the internal heat generation).

ρ fluid density

μ dynamic viscosity

υ kinematic viscosity

Superscripts

$*$ dimensionless parameter

$\rightarrow$ vector

$\cdot$ source term

Subscripts

0 characteristic parameter

c condenser

cr critical

l liquid

v vapor

w wall

$inlet$ at the inlet of the condenser

Dimensionless Groups

$Ja = \frac{c_{p,l}(T_{w,e} - T_{w,c})}{L}$ Jacob number

$Nu = \frac{hD}{k_l}$ Nusselt number

$Pr = \frac{\upsilon}{\alpha}$ Prandtl number

$Re = \frac{VD}{\upsilon}$ Reynolds number

$\Phi_l^* = -\frac{\rho_l g \sin\theta}{\mu_l} \cdot \frac{D^2}{w_0}$ dimensionless source term in the liquid phase

$\Phi_v^* = \frac{\partial P}{\partial z} \cdot \frac{1}{\mu_l} \cdot \frac{D^2}{w_0}$ dimensionless source term in the vapor phase

5.9 References

[1] Bejan, A. (1993). Heat Transfer. New York, John Wiley & Sons, Inc.

[2] Casarosa, C. (1988). "Experimental investigation and analytical modeling of a closed two-phase thermosyphon with imposed convection boundary conditions." International Journal of Heat and Mass Transfer **31**(9): 1815-1833.

[3] Chato, J. C. (1960). Laminar condensation inside horizontal and inclined tubes. Department of Mechanical Engineering, Massachusetts Institute of Technology (MIT). **Doctoral:** 203.

[4] Chato, J. C. (1962). "Laminar Condensation inside horizontal and inclined tubes." ASHRAE Journal: 52-60.

[5] Chen, M. M. (1961). "An Analytical Study of Laminar Film Condensation: Part 1 -- Flat Plates." Journal of Heat Transfer (Transactions of the ASME) **83**: 48-54.

[6] Chen, S. J., J. G. Reed, et al. (1984). "Reflux condensation in a two-phase closed thermosyphon." International Journal of Heat and Mass Transfer **27**(9): 1587-1594.

[7] Collier, J. G. (1972). Convective Boiling and Condensation. London, McGraw-Hill.

[8] Dhir, V. and J. Lienhard (1971). "Laminar Film Condensation on Plane and Axisymmetric Bodies in Nonuniform Gravity." Journal of Heat Transfer (Transactions of the ASME): 97-100.

[9] Dobran, F. (1985). "Heat transfer in an Annular Two-Phase Flow." Journal of Heat Transfer (Transactions of the ASME) **107**: 472-476.

[10] Dobran, F. (1985). "Steady-state characteristics and stability thresholds of a closed two-phase thermosyphon." International Journal of Heat and Mass Transfer **28**(5): 949-957.

[11] Gross, U. (1992). "Reflux Condensation Heat-Transfer inside a Closed Thermosiphon." International Journal of Heat and Mass Transfer **35**(2): 279-294.

[12] Harley, C. and A. Faghri (1994). "Complete Transient two-dimensional analysis of two-phase closed thermosyphons including the falling condensate film." Journal of Heat Transfer (Transactions of the ASME) **116**(2): 418-426.

[13] Kamminga, W. (1980). "An analytic solution of the film thickness of laminar film condensation on inclined pipes." International Journal of Heat and Mass Transfer **23**: 1291-1293.

[14] Lee, Y. and U. Mital (1972). "A Two-phase closed thermosyphon." International Journal of Heat and Mass Transfer **13**(9): 1695-1707.

[15] Reed, J. G. (1985). Analytical modeling of two-phase closed thermosyphon. Department of Mechanical Engineering. Berkeley, University of California, Berkeley. **Ph.D.:** 145.

[16] Reed, J. G. (1987). "Modeling of the two-phase closed thermosyphon." Journal of Heat Transfer (Transactions of the ASME) **109**(3): 9.

[17] Rohsenow, W. M. (1956). "Heat transfer and temperature distribution in laminar film condensation." Journal of Heat Transfer (Transactions of the ASME) **78**: 1645-1648.

[18] Sparrow, E. M. (1959). "A boundary layer treatment of laminar film condensation." Journal of Heat Transfer (Transactions of the ASME) **81**: 13-18.

[19] Spendel, T. (1981). Laminar Film condensation Heat Transfer in Closed Two-Phase Thermosyphons. 4th International Heat Pipe Conference, London, UK.

[20] Tien, C. L. and A. R. Rohani (1974). "Analysis of the effects of vapour pressure drop on heat pipe performance." International Journal of Heat and Mass Transfer **17**: 61-67.

[21] Wang, J. C. Y. and Y. W. Ma (1991). "Condensation Heat-Transfer inside Vertical and Inclined Thermosiphons." Journal of Heat Transfer-Transactions of the ASME **113**(3): 777-780.

[22] Xu, J. and D. Goering (2008). Theroetical and experimental analysis of two-phase thermosyphons. Department of Mechanical Engineering. Fairbanks, University of Alaska Fairbanks. **Ph.D.:** 200.

[23] Xu, J. and D. J. Goering (2008). "Experimental validation of passive permafrost cooling systems." Cold Regions Science and Technology.

[24] Zuo, Z. J. and F. Gunnerson (1994). "Numerical modeling of the steady-state two-phase closed thermosyphon." International Journal of Heat and Mass Transfer **37**(17): 2715-2722.

[25] Zuo, Z. J. and F. Gunnerson (1995). "Heat transfer analysis of an inclined two-phase closed thermosyphon." Journal of Heat Transfer (Transactions of the ASME) **117**(4): 1073-1075.

Chapter 6 Modeling of an inclined two-phase closed thermosyphon[1]

6.1 Abstract

Two-phase closed thermosyphons are widely used to protect man-made infrastructure and underlying permafrost in Arctic regions. Because of the particular working conditions, the thermosyphons often operate with limited heat fluxes and inclined geometries. These conditions have significant impacts on the internal processes and the overall performance of thermosyphons. In this work a comprehensive model is developed to predict the steady-state performance of an inclined two-phase closed thermosyphons with carbon dioxide used as the working fluid. A pseudo-one-dimensional numerical model with a two-dimensional cross sectional flow simulation is developed as part of the solution process. The simulation results are compared with experimental data and show good agreement.

6.2 Introduction

Two-phase closed thermosyphons are highly efficient heat transfer devices working under the assistance of gravity. The evaporation, condensation, and circulation processes of the working fluid within the thermosyphon are the main reasons for their unique properties including high heat transfer performance, passive operation, and the thermal diode effect.

The rapid development of arctic regions and the potential threat of global warming is spurring the application of thermosyphons in the arctic to protect man-made infrastructure and underlying permafrost. In most of the arctic engineering applications, the thermal diode effect is the most important thermosyphon characteristic that has been utilized. It enhances heat loss from the protected infrastructure and the permafrost layer to the cold winter air, but does not increase the heat gain from the air during the summer. The thermosyphon operation over the seasonal cycle yields a net heat loss and cooling

[1] Xu, J. and D.J. Goering, (2008). Modeling of an inclined two-phase closed thermosyphon. Prepared for submission to International Journal of Heat and Mass Transfer.

effect in the foundation soil. It helps to freeze back the foundation soil and the disturbed permafrost layer. One typical application of thermosyphon for the protection of roadways located in permafrost areas is described by J. Xu and D. Goering [33].

The hairpin thermosyphon represents a new configuration for thermosyphons with carbon dioxide used as the working fluid. Both the evaporator and condenser are buried under the road surface at shallow inclination angles. The special operating conditions have a significant impact on the internal processes of the thermosyphon and the overall performance. The object of this study is to increase the understanding of the comprehensive performance of this inclined two-phase closed thermosyphon as they are applied to arctic geotechnical problems.

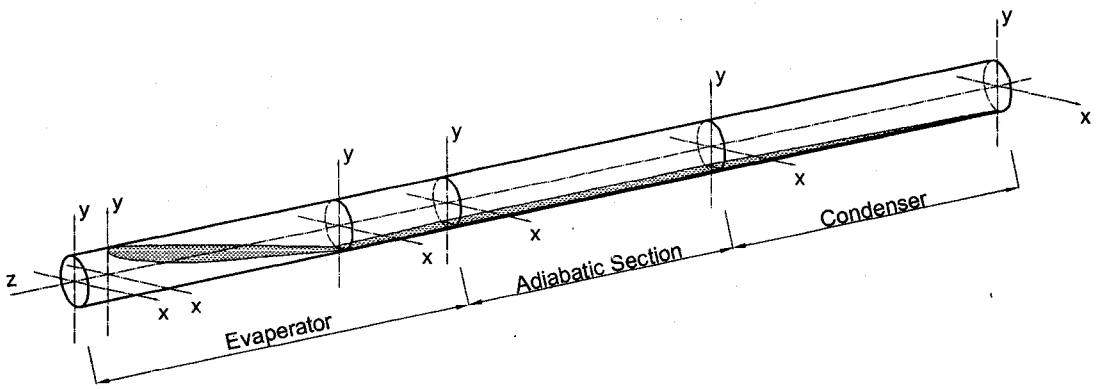

Figure 6.1 Inclined two-phase closed thermosyphon.

A schematic of the two-phase closed thermosyphon is shown in Figure 6.1. As in a typical thermosyphon, it is consist of a condenser, an adiabatic section, and an evaporator. A working fluid, carbon dioxide in this case, is sealed within the thermosyphon. In steady-state operation, the working fluid in the evaporator absorbs heat from a heat source and changes from a liquid to a vapor state, the vapor rises up to the condenser where it is cooled down and condensed back into liquid condensate. The condensate flows to the bottom of the pipe under the action of gravity and flows back to the evaporator to complete the cycle.

Unlike vertical thermosyphons, the large inclination angle in this case helps to limit the condensate film thickness by draining it into a rivulet on the bottom of the condenser pipe. It also reduces the driving force of the liquid phase since only the longitudinal component of the gravity is acting as the driving body force to help condensate return to the evaporator. The other unique aspect of this thermosyphon application is the limited heat flux. Under normal working conditions typical of arctic applications, the heat flux passing through the thermosyphon is limited by thermal conduction in the surrounding soil. This low heat flux influences the internal phase-change heat transfer processes. These unique aspects have yet to be completely understood and present challenges for the present modeling study.

Due to the complexity of the internal processes, the modeling of any thermosyphon is challenging. All models have to employ significant assumptions to simplify the problem to a solvable level, such as steady state operation, vertical geometry, laminar liquid film, negligible compressibility, negligible sensible heat related to sub-cooling and superheat, negligible pressure drop in the liquid film, etc.

The first thermosyphon model was developed by Y. Lee and U. Mital [19] based on a dimensional analysis. A "Lumped parameter" thermosyphon model was created by F. Dobran [11; 10] and was later improved by C. Casarosa [2] with consideration of the liquid entrainment in the vapor core. J. G. Reed [24] proposed a "control volume" model as a summary of his Ph.D. research [23]. This control volume method was very successful in reducing the complexity of the mathematical formulation and was adopted by C. Harley and H. Faghri [16] in their modeling. However, this control volume method can only describe the overall performance of the thermosyphon; it is still difficult to determine the local details of the flow and heat transfer within the thermosyphon.

Numerical methods are better able to solve the complicated equations governing thermosyphon behavior and reveal more details of the internal processes. In 1974, C. Tien and A. Rohani [30] constructed the first numerical model for the vapor flow in a

thermosyphon, examining the relation between the heat transfer performance and the vapor pressure drop. In 1994, Z. Zuo and F. Gunnerson [36] adapted J.G. Reed's [23; 24] control volume method in a numerical model, in which the liquid-film momentum advection and axial normal stress in the counter current two phase flow were considered. Z. Zuo and F. Gunnerson [37] also extended his numerical model to inclined thermosyphons, in which the inclination angle was classified into 3 different ranges depending on how the liquid pool covers the bottom of the thermosyphon pipe. Zuo's work has been the only comprehensive model dealing with inclined thermosyphons.

Phase change processes occurring inside the thermosyphon are the key reason for high heat transfer performance, however they are also the most difficult to model. "The fields of boiling and condensation are at present more of an art than a science and the subject remains, and will remain for some time to come, largely empirical [8]." The only success in theoretical modeling of phase change has been in the area of laminar filmwise condensation as originally conducted by Nusselt in the early 1900's. Nusselt's work has been improved on by W. Rohsenow [25], E. Sparrow [26], and more recently, M. Chen [6], T. Spendel [27], and S. Chen et al. [7]. Nusselt's theory was also extended to geometries other than flat plates by V. Dhir and J. Lienhard [9] and W. Kamminga [17]. More related to thermosyphon operation, condensation inside a pipe with a vertical or inclined orientation has been another active research area. J.C. Chato [3; 4] developed a momentum-energy integral method for the laminar condensation on a pipe wall and on the bottom condensate flow in inclined tubes. U. Gross [13] developed a semi-empirical correlation for reflux condensation based on 66 experimental studies. J. Wang and Y. Ma's [31] study showed that the inclination angle has a notable influence on the condensation coefficient.

In a thermosyphon, the evaporation process generally includes flow boiling and pool boiling. When the heat flux rates are extremely small, even forced or natural convection of the working fluid may be strong enough to remove the heat from the thermosyphon.

wall. In this situation, there is no nucleation in the evaporator and phase change occurs at the liquid-vapor interface via evaporation.

Both flow boiling and pool boiling have been studied extensively. However, theoretical modeling is still difficult and experimental correlations remain the better way to predict the heat transfer performance of boiling heat transfer in most cases. In 1966, J.C. Chen [5] proposed a correlation for convective flow boiling heat transfer for nonmetallic fluids. The micro-convective (nucleate boiling) and macro-convective (non-boiling forced convection) heat transfer mechanisms were considered additive. This superposition approach was adopted by many later researchers, such as K. Gungor and R. Winterton [14; 15], S.G. Kandlikar [18], Z. Liu and R. Winterton [20], J. Thome and El Hajal [29], C.Y. Park and P. Hrnjak [21; 22], H. Steiner et al. [28] and W. Zhang et al [35]. Because of the coupling of convective flow and nucleate boiling, the forced convection heat transfer is generally enhanced while the nucleate boiling is suppressed compared to cases of pure forced convection and pool boiling, respectively. Two factors were introduced in the correlations to indicate the enhancement and suppression effects. S.G. Kandikar [18] also developed a fluid-dependent parameter to account for working fluid differences.

6.3 Theoretical model

6.3.1 Governing equations

The general governing equations for an incompressible Newtonian fluid are as follows.

Mass conservation:

$$\frac{\partial \rho}{\partial t} + \nabla \cdot (\rho \vec{V}) = \dot{M} \tag{6.1}$$

Momentum conservation:

$$\frac{D\vec{V}}{Dt} = \vec{F} - \frac{1}{\rho}\nabla p + \upsilon \nabla^2 \vec{V} \tag{6.2}$$

Energy conservation:

$$\frac{DT}{Dt} = \alpha \nabla^2 T + \frac{1}{\rho c_p}\Phi \tag{6.3}$$

The assumptions made in the initial formulation are that the vapor is saturated, that the Mach number of the vapor flow is low enough that compressibility effects in the vapor phase are negligible, and that the entrainment of liquid droplets in the vapor phase is negligible. These assumptions are well justified in many systems of practical interest including the type of thermosyphon system examined here. In addition to these basic assumptions, more assumptions are necessary to further simplify the problem:

1. Steady state conditions;
2. A long pipe, $L >> D$;
3. For both liquid and vapor, $w >> u \sim v \sim 0$;
4. The liquid film thickness varies slowly in the z direction, $\frac{dH}{dz} << 1$;
5. For both liquid and vapor, $\frac{\partial^2 w}{\partial z^2} << \frac{\partial^2 w}{\partial x^2} \sim \frac{\partial^2 w}{\partial y^2}$;
6. In liquid film, gravity is the dominant body force;
7. Both liquid and vapor flows are laminar.

Both the evaporator and the condenser of the thermosyphon are long pipe sections in which the diameter is much smaller than the length of the pipe. In most regions of the pipe the velocity direction (for both vapor and liquid phase) closely parallels the pipe axis (z-axis), and the velocities in x and y direction can be regarded as negligible without introducing significant error.

Another simplification from the "long pipe" assumption is that the mass condensation or evaporation rate at a specific location is much smaller than the local bulk mass flow rate in the z-direction. The mass transfer between the liquid and vapor phases can then be considered a small uniform mass source distributed over the cross section. What's more, this small mass source also indicates a small flow rate gradient in the z-direction (or a small z-velocity gradient). Under no-slip boundary conditions, the velocity gradients in the x and y directions are relatively large, and the velocity gradient in z-direction can thus be considered negligible.

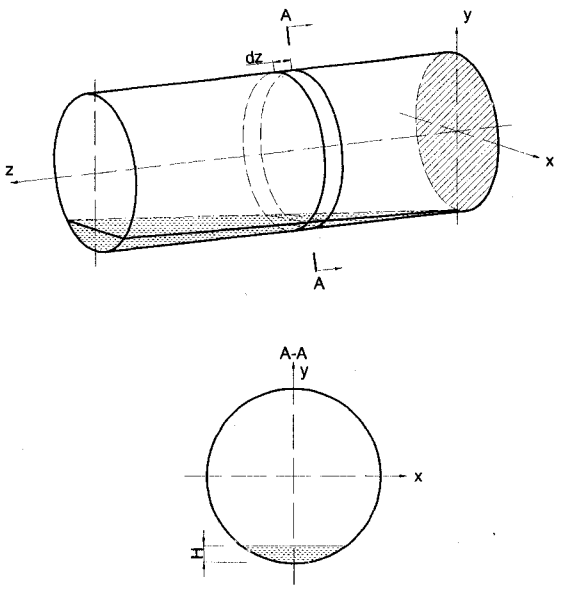

Figure 6.2 A control volume in the thermosyphon.

A schematic of a control volume in the thermosyphon is shown in Figure 6.2. It can serve to represent any section of the thermosyphon where both liquid and vapor phases coexist in a countercurrent stratified flow. As shown in Figure 6.2, the liquid flow occupies a small fraction of the cross-section at the bottom of the pipe. Under the action of gravity it flows in the positive z-direction. The vapor phase, on the other hand, flows in the opposite direction and occupies the upper portion of the flow channel. H is defined as the film thickness of the liquid rivulet and is clearly a function of the z-coordinate.

Utilizing the above assumptions, the mass conservation can be written as:

Liquid film: $$\rho_l\left(\int_{z+dz} w_l dA_l - \int_z w_l dA_l\right) = \dot{m}_l C(z)dz \qquad (6.4)$$

Vapor core: $$\rho_v\left(\int_{z+dz} w_v dA_v - \int_z w_v dA_v\right) = \dot{m}_v C(z)dz \qquad (6.5)$$

Because of negligible velocity in the x and y direction, only the z-momentum equation (M_z) needs to be considered. It takes a simplified form:

Liquid film: $$0 = \frac{g \sin\theta}{\upsilon_l} + \left(\frac{\partial^2 w_l}{\partial x^2} + \frac{\partial^2 w_l}{\partial y^2} \right) \quad (6.6)$$

Vapor Core: $$0 = -\frac{1}{\rho_v \upsilon_v} \frac{\partial P}{\partial z} + \left(\frac{\partial^2 w_v}{\partial x^2} + \frac{\partial^2 w_v}{\partial y^2} \right). \quad (6.7)$$

In forced convection configurations, according to A. Bejan [1], the mass conservation and momentum conservation equations are sufficient for determining the velocity distribution within the flow field. In such cases the fluid temperature distribution can be determined as an afterthought, by using the just-determined velocity distribution and the energy equation.

For the energy conservation equation, both the condensation heat transfer in the condenser and the evaporation heat transfer in the evaporator can be described with empirical correlations. The energy conservation can be simplified as

$$q(z) = h(z)\Delta T(z). \quad (6.8)$$

To complete the governing equations, supplemental relations for phase change and heat transfer are required:

In the liquid: $$\dot{m}_l(z) = \frac{q(z)}{L} \quad (6.9)$$

In the vapor: $$\dot{m}_v(z) = -\dot{m}_l(z). \quad (6.10)$$

By combining Equation (6.8) with Equations (6.9) and (6.10), the energy conservation can also be expressed as:

In the liquid: $$\dot{m}_l(z) = \frac{h(z)\Delta T(z)}{L} \quad (6.11)$$

In the vapor: $$\dot{m}_v(z) = -\frac{h(z)\Delta T(z)}{L}. \quad (6.12)$$

6.3.2 Boundary conditions

No-slip boundary conditions as given in Equations (6.13) and (6.14) are applied to the wall boundaries. No-slip and force balance boundary conditions given by Equations (6.15) to (6.17), are applied to the liquid-vapor interface.

In the liquid: $w_l = 0$ at pipe wall (6.13)

In the vapor: $w_v = 0$ at pipe wall. (6.14)

On the liquid-vapor interface:

$$w_l = w_v \tag{6.15}$$

$$\mu_l \frac{\partial w_l}{\partial x} = \mu_v \frac{\partial w_v}{\partial x} \tag{6.16}$$

$$\mu_l \frac{\partial w_l}{\partial y} = \mu_v \frac{\partial w_v}{\partial y}. \tag{6.17}$$

To focus on the internal processes of the thermosyphon, temperature boundaries as given in Equations (6.18) and (6.19) are adopted for the condenser and evaporator wall. A heat flux boundary, as given by Equation (6.20), is used on the adiabatic section.

In condenser $T_{w,c} = T_1$ (6.18)

In evaporator $T_{w,e} = T_2$ (6.19)

In adiabatic section $q_{w,a} = 0$. (6.20)

The governing Equations (6.6) to (6.10) and boundary conditions (6.13) to (6.20) represent a complete quasi one-dimensional model of the inclined two-phase closed thermosyphon with a two-dimensional analysis of the longitudinal velocity distribution in the cross section.

6.3.3 Non-dimensional Equations

The following non-dimensional variables are introduced to put the governing equations in non-dimensional form:

$$x^* = \frac{x}{D} \qquad y^* = \frac{y}{D} \qquad z^* = \frac{z}{D}$$

$$\rho_l^* = \frac{\rho_l}{\rho_l} = 1 \qquad \rho_v^* = \frac{\rho_v}{\rho_l} \qquad \mu_l^* = \frac{\mu_l}{\mu_l} = 1$$

$$\mu_v^* = \frac{\mu_v}{\mu_l} \qquad w_l^* = \frac{w_l}{w_0} \qquad w_v^* = \frac{w_v}{w_0} \tag{6.21}$$

$$\dot{m}_l^* = \frac{\dot{m}_l c_{p,l} D}{k_l} \qquad \dot{m}_v^* = \frac{\dot{m}_v c_{p,l} D}{k_l} \qquad T^* = \frac{T - T_0}{T_{w,e} - T_{w,c}}$$

$$h^* = \frac{h}{c_{p,l} w_0 \rho_l} \qquad C^* = \frac{C}{D} \qquad m^* = \frac{m}{\rho_l D^3}$$

where $w_0 = \dfrac{D^2 \rho_l g \sin\theta^2}{\mu_l}$ is the characteristic velocity, derived from a force balance between gravity and wall friction in liquid phase.

The governing equations can be written in dimensionless form using the above variables as follows:

Mass conservation:

$$\rho_l^* \int_{z^*+dz^*} w_l^* dA_l^* - \int_{z^*} w_l^* dA_l^* = \dot{m}_l^* C^* dz^* \tag{6.22}$$

$$\rho_v^* \int_{z^*+dz^*} w_v^* dA_v^* - \int_{z^*} w_v^* dA_v^* = \dot{m}_v^* C^* dz^* \tag{6.23}$$

Momentum conservation:

$$\mu_l^* \left(\frac{\partial^2 w_l^*}{\partial x^{*2}} + \frac{\partial^2 w_l^*}{\partial y^{*2}} \right) = \Phi_l^* \tag{6.24}$$

$$\mu_v^* \left(\frac{\partial^2 w_v^*}{\partial x^{*2}} + \frac{\partial^2 w_v^*}{\partial y^{*2}} \right) = \Phi_v^* \tag{6.25}$$

Energy conservation:

$$\dot{m}_l^* = -\dot{m}_v^* = Ja \cdot Nu \cdot (T^* - T_w^*) . \tag{6.26}$$

The boundary conditions can also be put in non-dimensional forms as follows:

In the liquid $w_l^* = 0$ at the wall (6.27)

In the vapor $w_v^* = 0$ at the wall (6.28)

On the liquid-vapor interface

$$w_l^* = w_v^* \tag{6.29}$$

$$\mu_l^* \frac{\partial w_l^*}{\partial x^*} = \mu_v^* \frac{\partial w_v^*}{\partial x^*} \tag{6.30}$$

$$\mu_l^* \frac{\partial w_l^*}{\partial y^*} = \mu_v^* \frac{\partial w_v^*}{\partial y^*}. \tag{6.31}$$

6.4 Solution methods

6.4.1 Boiling and Condensation Heat Transfer

As discussed in Chapters 2 and 3, the first principle modeling of boiling and condensation in a thermosyphon has proven challenging because of the lack of knowledge and the complexity of the mechanisms. The use of empirical correlations is a better way to describe the heat transfer processes associated with the phase-change phenomena.

In the condenser of hairpin thermosyphons, the condensation is most likely filmwise due to the small surface tension of CO_2. This was also verified by the lab experiment described by J. Xu and D. Goering [32]. Most of the existing experimental correlations and theoretical solutions are unable to predict the heat transfer performance when the condensation heat flux is extremely small. As discussed in Chapter 3, it is very likely that condensation under these small heat flux conditions is not strong enough to be the dominant heat transfer mechanism. When transitioning from forced convection to filmwise condensation, the convection heat transfer may still serve as a key mechanism even though filmwise condensation occurs at the same time. The experimental correlation developed by J. Xu and D. Goering [32] can predict this heat transfer behavior fairly well, so this correlation will be used as part of the thermosyphon modeling.

The boiling heat transfer in the thermosyphon evaporator is another phenomenon that is difficult to simulate theoretically. Fortunately, there have been abundant experimental studies in this area, most of which have resulted in experimental correlations. Several researchers including J.C. Chen [5], K. Gungor and R. Winterton [14; 15], S.G. Kandlikar [18], Z. Liu and R. Winterton [20], J. Thome and El Hajal [29], C.Y. Park and P. Hrnjak [21; 22], H. Steiner et al. [28], and W. Zhang et al. [35] developed general boiling heat transfer correlations based on a large bank of data both from their own experiments and from the literature. Additionally, the correlations by C. Park [21; 22] and R. Yun et al. [34] were developed from experiments using CO_2 as the working fluid.

Under extremely small heat flux conditions, it is possible that just single-phase liquid convection is strong enough to remove heat from the evaporator wall, no nucleate boiling occurs and evaporation at the liquid-vapor interface may be the only phase change process in the evaporator. This transitional evaporation would require a correlation which can cover heat transfer mechanisms of both pure convection and boiling. Fortunately, several correlations have been developed using a superposition method first introduced by J.C. Chen [5]. Chen's method combines the convection heat transfer and the nucleate boiling heat transfer together with weighting coefficients. The promotion and suppression relationship between these two mechanisms can easily be considered in this type of correlation. After a careful review of all the available correlations developed with this method, the one developed by S. Kandlikar [18] in 1990 was selected to predict the heat transfer coefficient in the evaporator. This correlation eliminates the discontinuity at the transition point from convective boiling to nucleate boiling and incorporates a fluid-dependent parameter to extend the applicability to other fluids that is not used in its development. This correlation is given in Equation (6.32).

$$\frac{h_{TP}}{h_l} = C_1 Co^{C_2} (25 Fr_{lo})^{C_5} + C_3 Bo^{C_4} F_{fl} \tag{6.32}$$

where,

h_{TP} is the two phase heat transfer coefficient;

h_l is the single-phase liquid-only heat transfer coefficient given by

$h_l = 0.023 Re_l^{0.8} Pr_l^{0.4} (k_l / D)$;

$C_1 \sim C_5$ are constants developed in this study;

$Co = \left(\frac{1-x}{x}\right)^{0.8} \left(\frac{\rho_g}{\rho_l}\right)^{0.5}$ is the convection number;

$Fr_{lo} = \frac{G^2}{\rho_l^2 gD}$ is the Froude number with all flow as liquid;

$Bo = \frac{q}{GL}$ is the boiling number; and

F_{fl} is a fluid-dependent parameter.

The fluid-dependent parameter for carbon dioxide is not provided by S. Kandlikar [18]. As suggested by Kandlikar, the F_{fl} for carbon dioxide in the current model is estimated as the multiplier in the Forster and Zuber [12] correlation for pool boiling.

6.4.2 Flow simulation

The liquid and vapor flow within the thermosyphon can be considered as forced convection. Under this forced convection configuration, the velocity field and the temperature distribution are uncoupled and the mass conservation and momentum equations are sufficient for determining the flow field [1]. The fluid temperature distribution can be determined as an afterthought, by using the just-determined velocity distribution and the energy conservation principle. The governing equations to determine the velocity field are relatively simple, it is the geometry that complicates the problem. Numerical simulation with a commercial CFD code, FLUENT, was used in solving this two-dimensional problem.

The numerical solution of the Poisson equations in FLUENT can be verified by simulating a simpler one-dimensional problem and comparing with the analytical solution. This one-dimensional problem is illustrated in Figure 6.3.

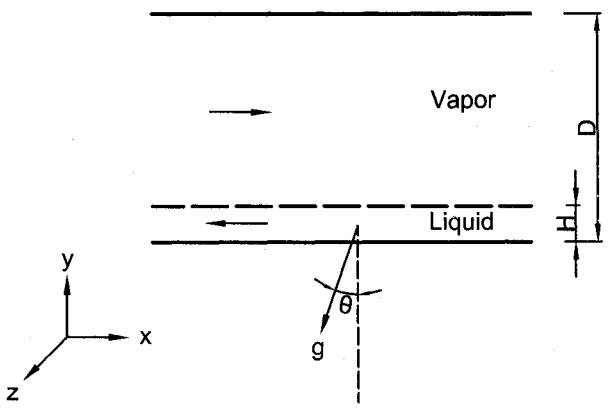

Figure 6.3 One-dimensional countercurrent problem.

The distance between the top and bottom wall is D, the liquid film has a thickness of H, and the flow channel is infinite in the z direction. The liquid and vapor flow have exactly the same mass flow rate, but travel in opposite directions. The longitudinal component of gravity is the dominant driving force for the liquid phase, while the pressure gradient drives the vapor phase. The countercurrent flow is balanced, and there is no acceleration in either the liquid or vapor phases. The velocity gradient in the x direction is zero. Thus the problem is one-dimensional with velocity changing only in the y direction. The governing equations are as follows:

$$\dot{m}_l = -\dot{m}_v \tag{6.33}$$

$$\mu_l \frac{\partial^2 w_l}{\partial y^2} = \rho_l g \sin(\theta) = \Phi_l \tag{6.34}$$

$$\mu_v \frac{\partial^2 w_v}{\partial y^2} = \frac{\partial p_v}{\partial z} = \Phi_v . \tag{6.35}$$

The boundary conditions are:

$$w_l = 0 \qquad \text{at } y = 0 \tag{6.36}$$

$$w_l = w_v \qquad \text{at } y = H \tag{6.37}$$

$$\mu_l \left.\frac{dw_l}{dy}\right|_H = -\mu_v \left.\frac{dw_v}{dy}\right|_H \qquad \text{at } y = H \tag{6.38}$$

$$w_v = 0 \qquad \text{at } y = D. \tag{6.39}$$

This problem has an analytical solution given by Equation (5.39) and Equation (6.41).

$$w_l = y^2 \frac{\Phi_l\left(H\mu_v - \mu_l H + \mu_l D\right)}{2\mu_l D\left(HD\mu_v - HD\mu_l + D^2\mu_l\right)} + y\frac{\Phi_l\left(2H^2\mu_l - H^2\mu_v - 2HD\mu_l\right) + \Phi_v\mu_l\left(2HD - H^2 - D^2\right)}{2\mu_l\left(H\mu_v - H\mu_l + D\mu_l\right)} \tag{6.40}$$

$$w_v = y^2 \frac{\Phi_v\left(H\mu_v - H\mu_l + D\mu_l\right)}{2\mu_v\left(H\mu_v - H\mu_l + D\mu_l\right)} + y\frac{\left(\Phi_l H^2\mu_v - 2\Phi_v H^2\mu_v + \Phi_v H^2\mu_l - \Phi_v D^2\mu_l\right)}{2\mu_v\left(H\mu_v - H\mu_l + D\mu_l\right)} + \frac{H^2 D\left(2\Phi_v\mu_v - \Phi_l\mu_v - \Phi_v\mu_l\right) + \Phi_v HD^2\left(\mu_l - \mu_v\right)}{2\mu_v\left(H\mu_v - H\mu_l + D\mu_l\right)} \tag{6.41}$$

In Figure 6.4, the results from the numerical simulation are compared with the analytical solution given in Equations (5.39) and (6.41). The diagram shows the velocity distribution in one cross-section from both the analytical solution and the FLUENT simulation. The liquid-vapor interface is indicated by a horizontal solid line and the cross-section is indicated by a vertical dashed line. The y-axis is the same as in Figure 6.3 and shows the vertical position in the flow channel. The x-axis shows the non-dimensional velocity magnitude.

Obviously, the FLUENT simulation matches the analytical solution very well. Therefore, it is reasonable to believe that numerical simulation in FLUENT can also provide an accurate prediction of the velocity distribution for the two-dimensional problem.

For the two-dimensional FLUENT simulation, a representative cross-section (with a 0.1D film thickness) of the circular pipe is shown in Figure 6.5 with the generated mesh. A fine boundary mesh is used near the wall area and the liquid-vapor interface to capture more details where high velocity gradients may exist.

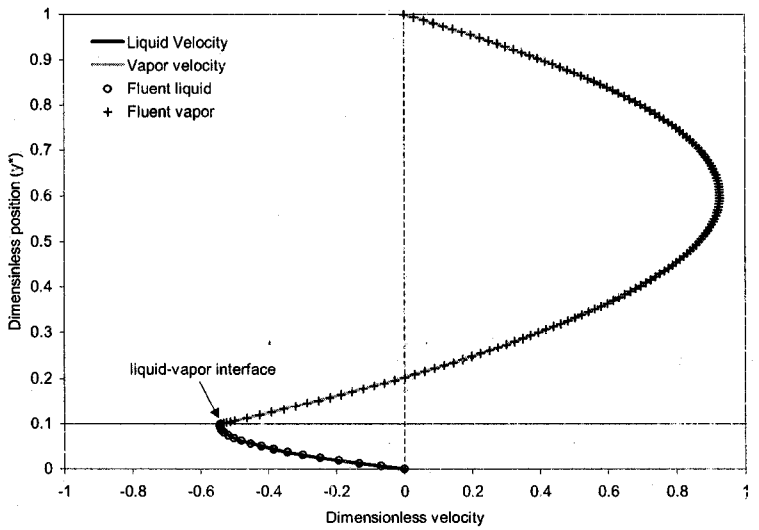

Figure 6.4 One-dimensional simulation in FLUENT with analytical solution.

An iterative method is used in solving this problem. The source term in the liquid-phase is known for any given film thickness, while a tentative pressure gradient can be used as the source term in the vapor phase. Both the liquid and vapor equations can be solved together, and the total flow rate for each phase can then be found by integrating over their own portion of the cross section. According to the steady state assumption and mass conservation, at any cross-section of the thermosyphon the mass flow rate of the liquid film and the vapor core should be equal in magnitude and opposite in direction. If the integrated flow rates of the liquid phase and vapor phases are not equal, modifications can be made to the tentative pressure gradient in the vapor phase. After a number of iterations, the integrated flow rates in both phases become close enough to be considered equal. This strategy is used to solve Equations (6.24) and (6.25) for a particular film thickness (H^*). In order to form a complete solution for the entire thermosyphon, these

equations need to be solved for different film thicknesses. Ultimately, the velocity profile, flow rate and other flow characteristics can be regressed as functions of film thickness (H^*).

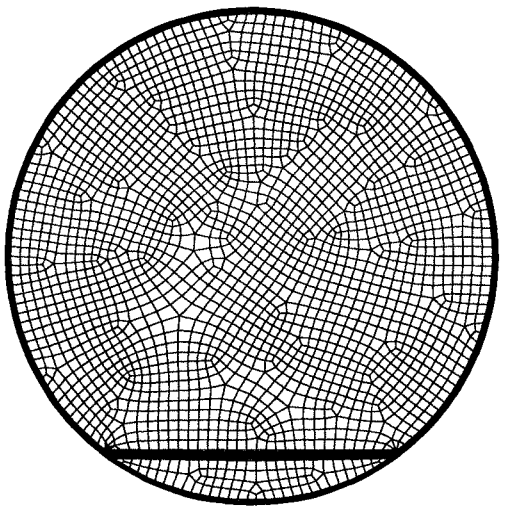

Figure 6.5 Mesh generated in Gambit for a two-dimensional pipe cross section.

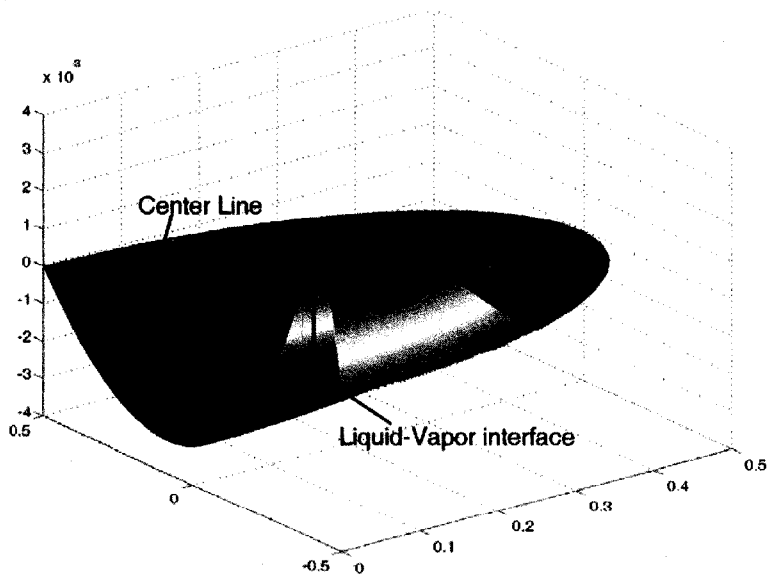

Figure 6.6 Velocity surface.

The velocity distribution across the section is illustrated by a three-dimensional surface in Figure 6.6, for a $0.1D$ film thickness case. Only half of the cross section is shown to reveal the velocity profile on the center line. Obviously, the liquid velocities are all positive, while some of the vapor near the liquid-vapor interface is entrained by friction and moves in the direction of liquid flow. The bulk vapor flow still has negative velocity and moves in the opposite direction from the liquid flow.

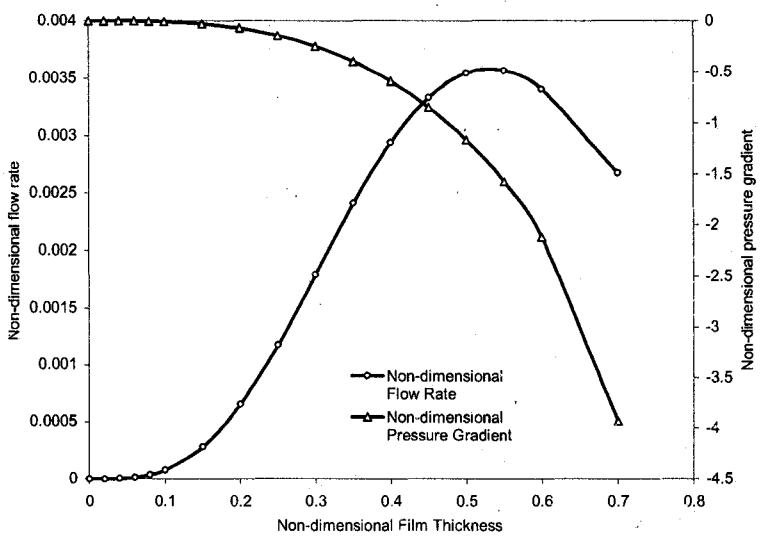

Figure 6.7 Flow rate and pressure gradient vs. film thickness.

The dependence of the mass flow rate and the pressure gradient on the film thickness is shown in Figure 6.7, with the flow rate scale on the left and the pressure gradient scale on the right. As shown in Figure 6.7, the pressure gradient always increases (in absolute value) as the film thickness increases, while the flow rate reaches a maximum value around a film thickness of 0.55. Beyond this limit, any increase of film thickness can actually result in a decrease in flow rate because the high vapor velocity and interfacial friction make a portion of the liquid flow backward. In reality, the flow limit can occur at a much smaller film thickness because of turbulent flow, a wavy interface, or liquid drop entrainment in the vapor flow. The flow that occurs in a hairpin thermosyphon should only occupy in the leftmost region of the figure. To ensure accuracy linear interpolation instead of a fitted equation is used in the comprehensive model.

6.4.3 Solution sequence

As discussed previously, the thermosyphon to be modeled is divided into a number of control volumes. Each of these control volumes has a similar structure but different parameters such as vapor velocity, liquid velocity, film thickness, and pressure drop, and temperature profiles. These control volumes are joined to each other to constitute the condenser, the adiabatic section and the evaporator. The heat transfer and fluid flow calculations are based on these individual control volumes.

At the beginning, a tentative working temperature is calculated based on the mean temperature of the condenser wall and the evaporator wall. This tentative working temperature is assigned to each control volume, together with a tentative heat transfer coefficient. The heat flux and mass source in each control volume can be determined based on the fixed wall temperature and the tentative parameters for the working fluid. The mass source in each control volume can then be calculated and added to the vapor or liquid flow. Based on the mass flow rate in each control volume, the condensate film thickness and the pressure gradient in the vapor flow can also be determined using the relations given in Figure 6.7. In the evaporator, the liquid mass flow rate into the liquid pool is compared with the vapor mass flow rate out of the liquid pool. Generally, these two mass flow rates are not equal at the beginning, which also indicates the overall heat flux in the condenser and the evaporator are not equal.

At this point, a new working temperature has to be proposed based on the heat transfer difference between the evaporator and the condenser. This temperature shift will have a significant impact on the performance ratio between the condenser and the evaporator. After several iterations, the right working temperature will finally be reached, which also determines the film thickness distribution, the temperature distribution, and all the other flow and thermal parameters. At this point, all of the governing equations and boundary conditions are satisfied simultaneously. The parameters contained in each control volume constitute the solution to the original modeling problem.

6.5 Results and discussions

6.5.1 Details within the thermosyphon

To illustrate the performance of this thermosyphon model, several example simulations were carried out under typical hairpin thermosyphon working conditions. The parameters and boundary conditions used in these simulations are listed in Table 6.1.

Table 6.1 Known parameters

Parameter	Units	Value
Working fluid	--	CO_2
Inclination angle	°	3.0
Condenser wall temperature	°C	-8.0
Condenser diameter	mm	78.0
Condenser wall thickness	mm	5.0
Condenser length	m	10.0
Evaporator wall temperature	°C	-6.0
Evaporator diameter	mm	78.0
Evaporator wall thickness	mm	5.0
Evaporator length	m	17.0
Adiabatic section diameter	mm	78.0
Adiabatic section wall thickness	mm	5.0
Adiabatic section length	m	2.0
Charging ratio	--	0.66

The charging ratio is the ratio between the volume of the working fluid all in the liquid phase at the operating temperature and the volume of the evaporator. In this simulation, the condenser and evaporator are both divided into 100 control volumes. The adiabatic section is divided into 20 control volumes. The simulation results are summarized in Table 6.2.

From Table 6.2, it can be found that the thermosyphon working temperature tends to be closer to the temperature of the condenser wall. This is mainly due to the fact that the thermal resistance in the condenser is significantly smaller than that of the evaporator. Although the length of the condenser is shorter than the evaporator, the effective heat transfer area of the condenser is still larger than the evaporator, because the effective heat

transfer area (the wetted area) in the evaporator only occupies a small portion of the evaporator pipe. To maintain the balance between the heat absorbed in the evaporator and the heat dissipation in the condenser, a large portion of the 2-degree overall temperature difference is consumed in the evaporator. The small discrepancy between the heat rate in the condenser and that in the evaporator is the result of using the mass flow rate in judging convergence and using the local latent heat in the heat transfer calculation.

Table 6.2 Summary of modeling results

Parameter	Units	Value
Working temperature	°C	-7.65
Working pressure	kPa	2821.0
Overall pressure drop	Pa	957.1
Condenser heat rate	W	123.8
Condenser mass flow rate	g/s	0.49
Condenser mass storage	kg	14.8
Adiabatic section mass storage	kg	3.0
Evaporator heat rate	W	-122.9
Evaporator mass flow rate	g/s	0.49
Evaporator mass storage	kg	35.6
Length of liquid pool	m	4.36

Under these working conditions, the liquid CO_2 is about 10 times heavier than the CO_2 vapor. This relatively small difference in the CO_2 liquid and vapor density explains why the mass storage in the condenser is so large even though there is only a small amount of liquid CO_2 condensate there. It also explains the 4.36 m liquid pool at the balanced condition with an initial charge ratio of 0.66.

A more detailed illustration of the pressure and pressure gradient distribution in the thermosyphon is given in Figure 6.8. The CO_2 vapor density at the working condition is around 77 kg/m^3. This results in a relatively high hydrostatic pressure gradient. The pressure gradient required to overcome the vapor flow friction and drive the vapor flow is very small in magnitude and is literally negligible compared to the hydrostatic pressure

gradient. Therefore, the variation of absolute pressure in the thermosyphon is nearly linear. The overall pressure drop from the evaporator to the condenser is about 1000 Pa. As shown in Figure 6.8, the pressure gradient in the condenser increases with the x-coordinate because of the increasing mass flow rate accumulating along the pipe. In the adiabatic section, no phase change is occurring, the mass flow rate and pressure gradient are all constant. In the evaporator (not in the liquid pool), the pressure gradient decreases with the x-coordinate because of the decreasing mass flow rate, but this rate of decrease is much smaller than the rate of increase in the condenser because of the small wetted area of the condensate flow in the evaporator.

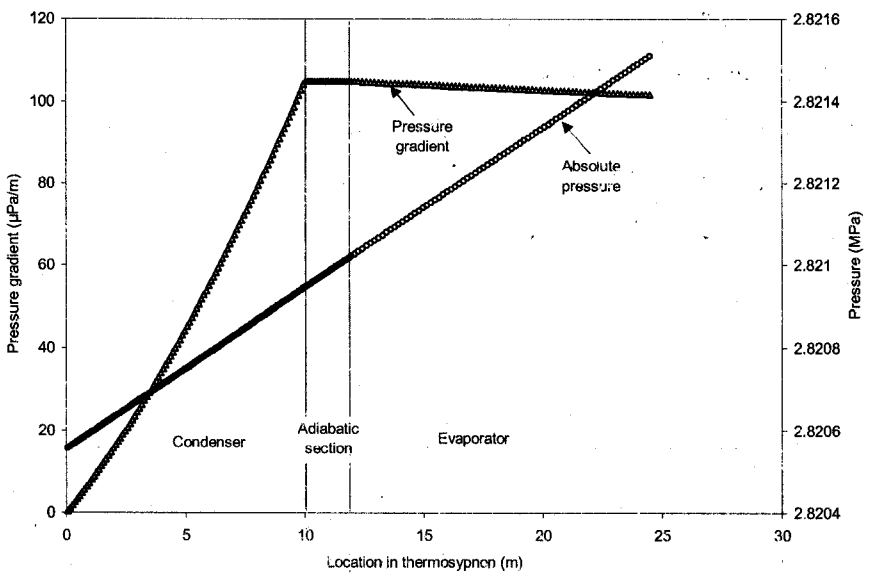

Figure 6.8 Pressure and pressure gradient distribution.

Figure 6.9 shows the condensate film thickness and the local heat transfer rate along the thermosyphon. Because of the velocity dependent heat transfer coefficient, the local heat transfer rate in the condenser is not uniform: it is stronger at the entrance of the condenser and weaker at the tip. In the evaporator (not in the liquid pool), the wetted area is very limited, which results in a very small evaporative heat transfer rate. Most of the heat

absorbed in the evaporator is absorbed in the liquid pool. There is no heat transfer in the adiabatic section. As a result of the local heat transfer rate, the condensate film thickness starts from zero at the top of the condenser and achieves its maximum at the outlet of the condenser; it remains constant in the adiabatic section, and decreases slightly in the evaporator until it reaches the liquid pool (which is not shown in Figure 6.9).

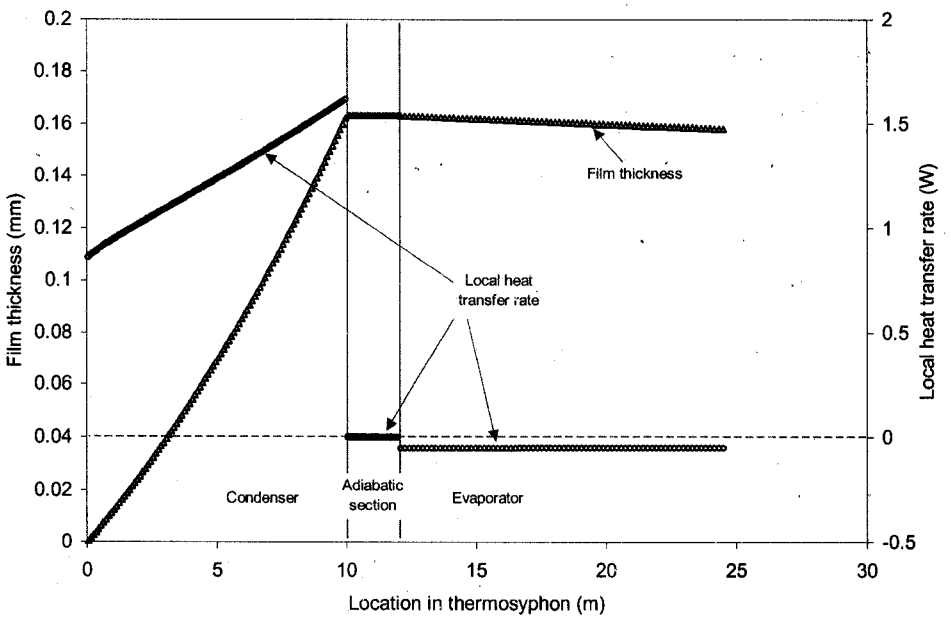

Figure 6.9 Film thickness and local heat flux distribution.

6.5.2 Temperature Boundary Influences

A series of simulations were performed to examine the dependence of the thermosyphon performance on the temperature difference between the evaporator and condenser. The wall temperature of the evaporator was fixed at -6 °C while the condenser temperature was varied from -8 °C to -12°C in 0.5 C° increments. The simulation results are summarized in Table 6.3.

Table 6.3 Summary of 9 simulations

No.	Condenser Wall temperature	Evaporator Wall temperature	Working Temperature	Overall heat flux	Pressure drop	Pool length
	°C	°C	°C	W	Pa	m
1	-8.0	-6.0	-7.65	123.8	957	4.36
2	-8.5	-6.0	-8.01	183.4	940	4.45
3	-9.0	-6.0	-8.36	251.7	929	4.49
4	-9.5	-6.0	-8.72	331.9	919	4.53
5	-10	-6.0	-9.07	432.0	902	4.62
6	-10.5	-6.0	-9.43	540.8	892	4.66
7	-11.0	-6.0	-9.79	665.0	882	4.69
8	-11.5	-6.0	-10.14	818.6	866	4.77
9	-12.0	-6.0	-10.50	979.7	856	4.80

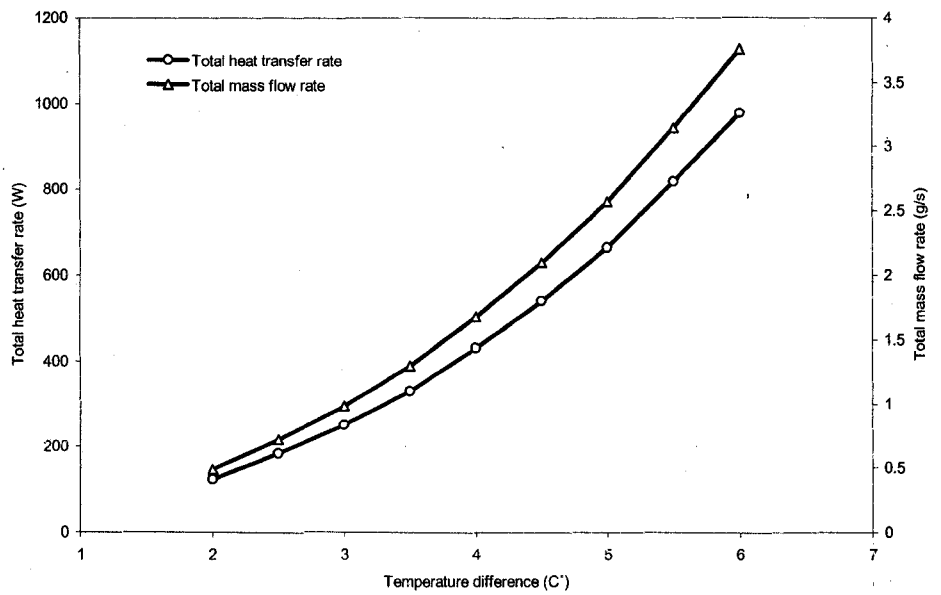

Figure 6.10 Temperature difference influence on total mass flux and pressure drop.

The influences of temperature difference on the total heat transfer rate and the total mass flow rate are illustrated in Figure 6.10. The x-coordinate is the wall temperature difference between the evaporator and the condenser. The total heat transfer rate and mass flow rate are plotted against the operating temperature difference on the scales at the left and right sides of the plot, respectively. The heat transfer performance of the hairpin thermosyphon is clearly enhanced by increasing the temperature difference. One

major reason for this positive feedback is the positive relationship between the Reynolds number and the Nusselt number in the condensation heat transfer correlation obtained from the lab experiment (see J. Xu and D. Goering [32]). Besides increasing the driving force of heat transfer, the increasing operating temperature difference can also increase the heat transfer coefficient by inducing higher mass flow rate and Reynolds number.

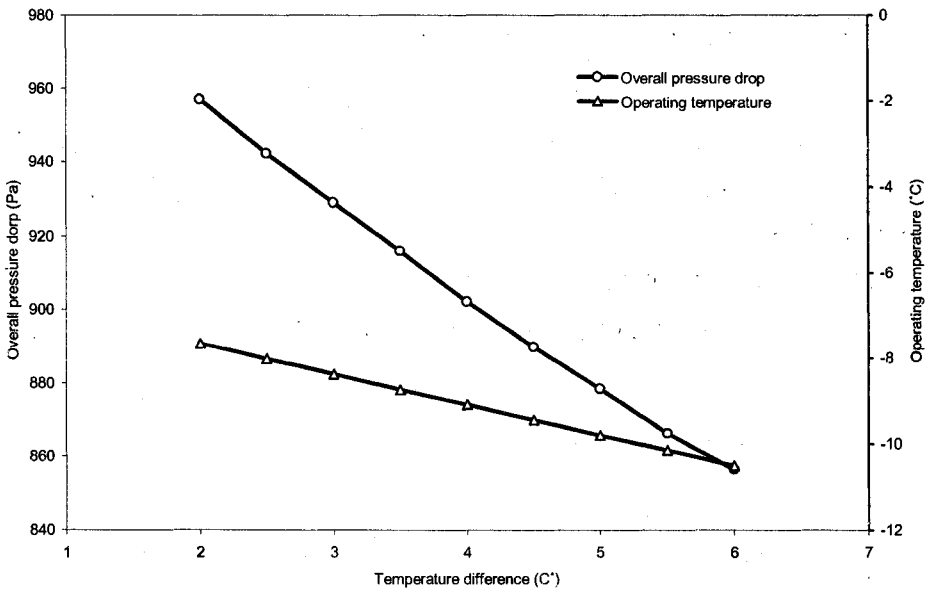

Figure 6.11 Dependences of overall pressure drop and operating temperature on the temperature difference.

The behavior of the total pressure drop and the operating temperature is given in Figure 6.11 as a function of temperature difference. In contrast to the heat transfer performance, the pressure drop through the thermosyphon decreases as the temperature difference increases. The reason for this different trend has to do with the variation of CO_2 properties with changing temperature. As discussed previously, the pressure gradient driving the vapor flow is much smaller than the hydrostatic pressure gradient. The hydrostatic pressure gradient essentially determines the overall pressure drop. As shown in Figure 6.11, as the temperature difference increases, the thermosyphon operating temperature drops because of the fixed evaporator temperature. This drop in operating

temperature results in a reduced saturation vapor density, as shown in Figure 6.12. This lower vapor density is the reason for the decreasing hydrostatic pressure gradient and the overall pressure drop.

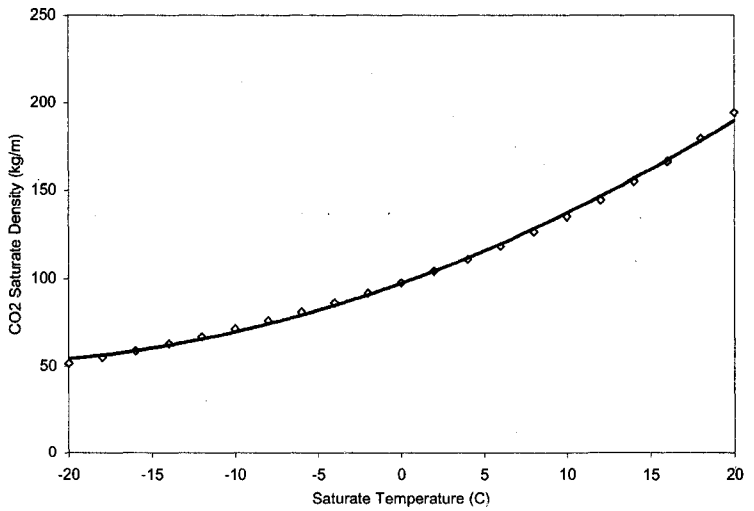

Figure 6.12 Density of saturated carbon dioxide vapor at different temperatures.

6.5.3 Charging Ratio Influences

The charge ratio in this research is defined as the ratio of the volume that the working fluid occupies in liquid form at the working temperature to the total volume of the evaporator. A series of simulations was carried out to reveal the charge ratio's influences on the performance of a hairpin thermosyphon. Under a 2 C° operating temperature difference, 10 different charge ratios, ranging from 0.66 to 1.1, are studied and summarized in Table 6.4.

The charge ratio has a very strong influence on the heat transfer performance of the thermosyphon. High charge ratio enhances the thermosyphon performance especially when the thermal resistance on the evaporator side is relatively larger than the thermal resistance of the condenser. More detailed analysis is given in the following paragraphs

to illustrate the charge ratio influence on the liquid pool length, the heat transfer rate, and the operating temperature.

Table 6.4 Summary of 10 simulations of charging ratio influence

No.	Charging ratio	Evaporator/Condenser Wall temperature	Working Temperature	Overall heat flux	Pressure drop	Pool length
	-	°C	°C	W	Pa	m
1	0.66	-6.0/-8.0	-7.65	123.8	957	4.355
2	0.70	-6.0/-8.0	-7.54	166.9	920	5.270
3	0.75	-6.0/-8.0	-7.43	219.6	877	6.538
4	0.80	-6.0/-8.0	-7.33	271.1	833	7.759
5	0.85	-6.0/-8.0	-7.23	323.0	782	8.747
6	0.90	-6.0/-8.0	-7.16	370.6	736	10.290
7	0.95	-6.0/-8.0	-7.09	418.0	684	11.597
8	1.00	-6.0/-8.0	-7.03	461.3	638	12.854
9	1.05	-6.0/-8.0	-6.97	504.2	585	14.174
10	1.10	-6.0/-8.0	-6.92	544.9	531	15.498

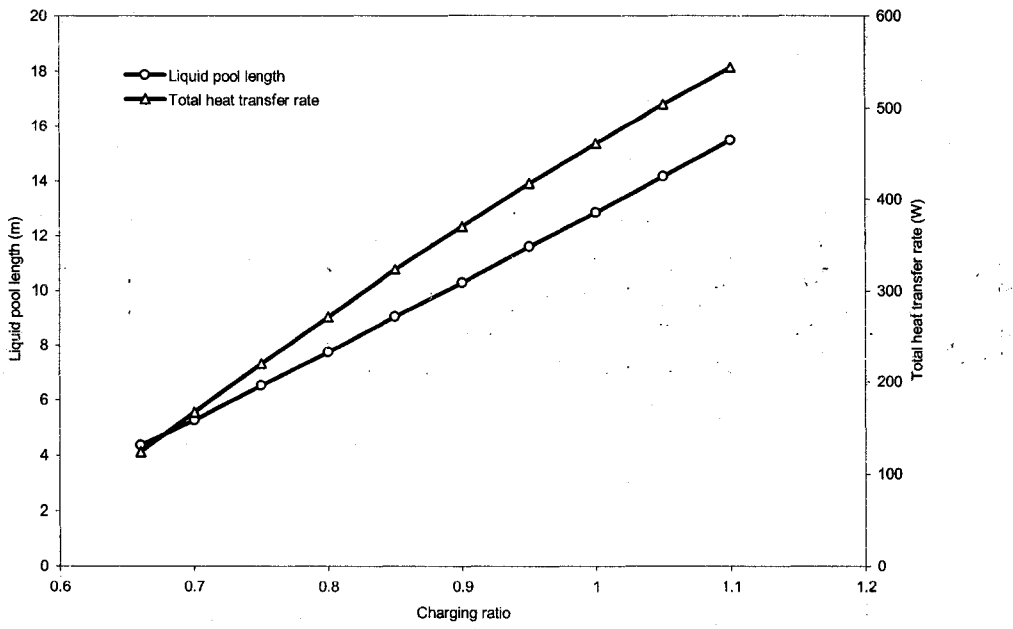

Figure 6.13 Charging ratio influence on the balanced pool length and total heat flux.

Figure 6.13 shows the relations between the charging ratio and both the length of liquid pool and the total heat transfer rate. The charging ratio has a nearly linear relation with the liquid pool length. The heat transfer rate also increases when the charge ratio increases. For an inclined setup like the hairpin thermosyphon, the returning condensate forms a small rivulet on the bottom of the evaporator pipe, leaving most of the pipe wall dry. The boiling heat transfer is greatly limited by the small wetted area in the evaporator. A large charging ratio can effectively increase the wetted area in the evaporator and thus enhance the overall heat transfer performance. For a vertical thermosyphon, on the other hand, the charging ratio doesn't have as much influence on the evaporator heat transfer performance, because the returning condensate covers a larger portion of the circumference of the evaporator pipe. An increase in the charge ratio does not help increase the wetted wall area in this case.

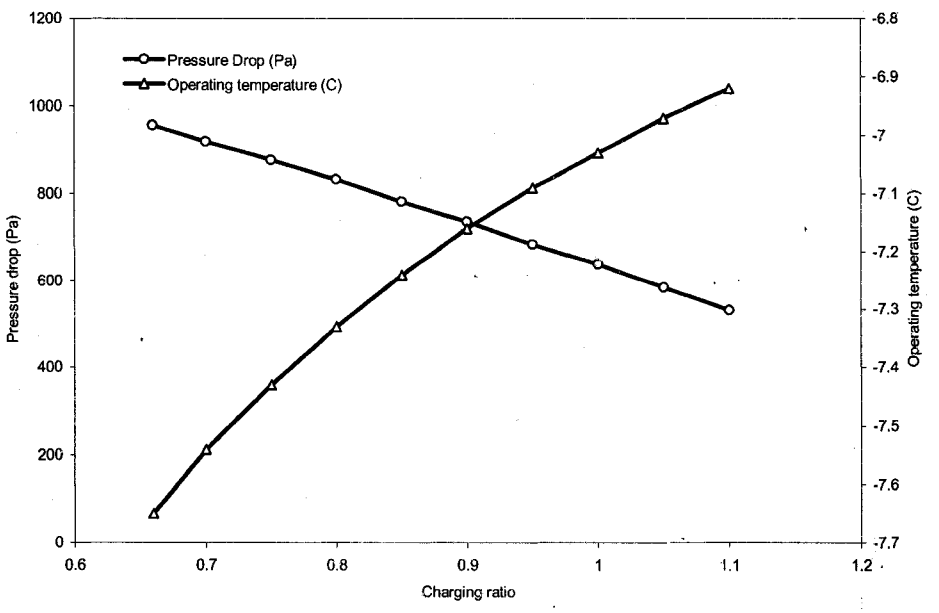

Figure 6.14 Charge ratio influence on the total pressure drop and working temperature.

As shown in Figure 6.14, the working temperature shifts toward the evaporator side when the charging ratio increases. This is also due to the enhancement of heat transfer in the

evaporator. Under the same condenser and evaporator wall temperature, a large charging ratio enhances the heat transfer process and reduces the thermal resistance in the evaporator. It tilts the original thermal resistance balance between the condenser and evaporator and induces a redistribution of temperature differences. As the thermal resistance in the evaporator decreases, a smaller temperature difference is required in the evaporator, and thus the working temperature shifts to the evaporator side.

6.5.4 Comparison with full scale road test

The model prediction is compared with the full scale road test data from Thompson Drive. The experimental data used in the comparison dates from 01/01/2005 to 08/14/2006. All the non-operational data points (condenser warmer than the evaporator) are eliminated from the comparison. There are about 6500 valid data points during this period. All the data points are corrected for the temperature measurement error as described by J. Xu and D. Goering [32]. The parameters in the modeling prediction are the same as shown in Table 6.1. The condenser temperature is set to -8 °C, the evaporator temperature changes from -7 °C to -3.6 °C. Both the experimental data and the modeling prediction are plotted in Figure 6.15 for comparison.

As shown in Figure 6.15, the experimental data is very scattered because of the transient effects in the real field experiment and the measurement errors. Never-the-less the majority of the data points display a fairly linear behavior with increasing temperature difference. The model prediction is not linear, which is mainly because of the non-linear experimental correlations used for the condensation and evaporation heat transfer coefficients. Compared with experimental data, the model prediction tends to underestimate heat transfer at low temperature differences and overestimate at higher temperature differences. But it gives pretty good predictions in the temperature difference range from 1.5 C° to 4 C°, which represents most of the actual operating range of the hairpin thermosyphons.

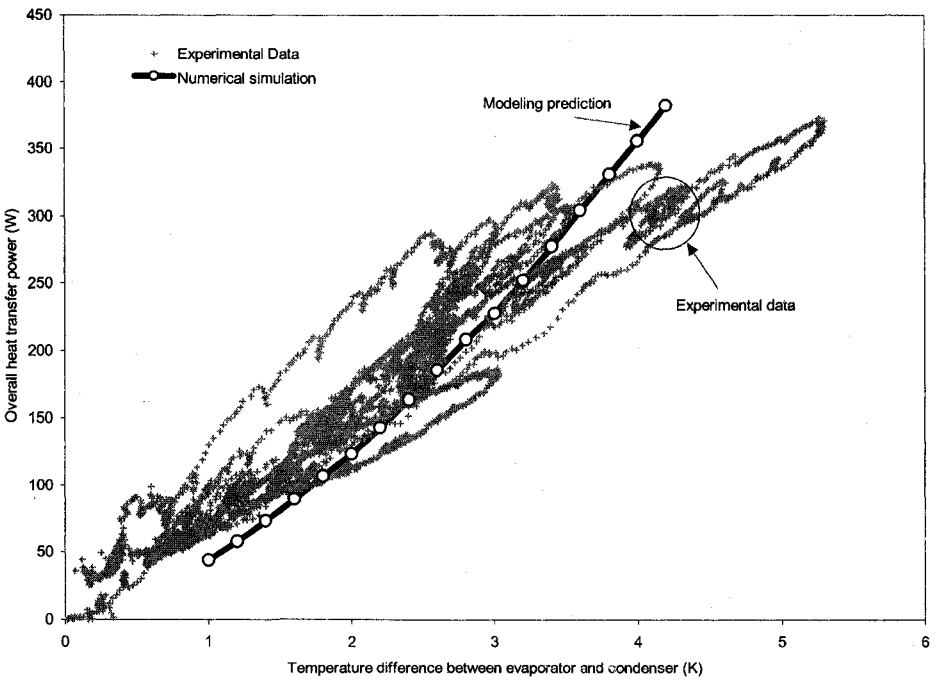

Figure 6.15 Comparison with full scale road test.

6.6 Conclusions

The quasi one-dimensional model for inclined long thermosyphons is developed to predict their comprehensive heat transfer performance. There are several features that distinguish this model from other comprehensive models:

- The current model is developed specifically for long inclined thermosyphons.
- The current model uses the condensation heat transfer correlation developed from the lab experiment at an extremely low heat flux conditions, which make it suitable for predicting the performance of thermosyphons used in typical arctic applications.
- The current model uses a 2D numerical analysis to determine the velocity distribution over the pipe section and the relations between the vapor pressure gradient, liquid film thickness and the longitudinal mass flow rate.

This model can be used to predict hairpin thermosyphon performance in the road embankment stabilization applications in permafrost areas. The comparison of the model

prediction with the full scale road test data shows fairly good agreement over the majority of the operating range of hairpin thermosyphons.

6.7 Acknowledgements

This work was supported by Alaska Experimental Program to Stimulate Competitive Research (EPSCoR) and Alaska Department of Transportation & Public Facilities (AKDOT).

6.8 Nomenclature

A area

$C(z)$ phase change perimeter

D inner diameter

c_p specific heat

$\vec{F}$ body force

F_{fl} fluid-dependent parameter

H film thickness

h heat transfer coefficient

L latent heat

$\dot{M}$ mass generation

$\dot{m}$ effective mass source in cross section

p pressure

q local heat flux

T temperature

u velocity in x-direction

$\vec{V}$ velocity vector

v velocity in y-direction

w velocity in z-direction

Greek Symbols

α thermal diffusivity

Δ difference

θ inclination angle of the thermosyphon

Φ dissipation function (including the internal heat generation).

ρ fluid density

μ dynamic viscosity

υ kinematic viscosity

Superscriptions

* dimensionless parameter

$\rightarrow$ vector

$\cdot$ source term

Subscriptions

0 characteristic parameter

c condenser

e evaporator

l liquid

v vapor

w wall

TP two phase

Dimensionless Groups

$Bo = \frac{q}{GL}$ boiling number

$Co = \left(\frac{1-x}{x}\right)^{0.8}\left(\frac{\rho_g}{\rho_l}\right)^{0.5}$ convection number

$Fr_{lo} = \frac{G^2}{\rho_l^2 gD}$ Froude number with all flow as liquid

$Ja = \frac{c_{p,l}(T_{w,e} - T_{w,c})}{L}$ Jacob number

$Nu = \frac{hD}{k_l}$ Nusselt number

$Pr = \frac{\upsilon}{\alpha}$ Prandtl number

$Re = \frac{VD}{\upsilon}$ Reynolds number

$\Phi_l^* = -\frac{\rho_l g \sin\theta}{\mu_l} \cdot \frac{D^2}{w_0}$ dimensionless source term in the liquid phase

$\Phi_v^* = \frac{\partial P}{\partial z} \cdot \frac{1}{\mu_l} \cdot \frac{D^2}{w_0}$ dimensionless source term in the vapor phase

6.9 References

[1] Bejan, A. (1993). Heat Transfer. New York, John Wiley & Sons, Inc.

[2] Casarosa, C. (1988). "Experimental investigation and analytical modeling of a closed two-phase thermosyphon with imposed convection boundary conditions." International Journal of Heat and Mass Transfer **31**(9): 1815-1833.

[3] Chato, J. C. (1960). Laminar condensation inside horizontal and inclined tubes. Department of Mechanical Engineering, Massachusetts Institute of Technology (MIT). **Doctoral:** 203.

[4] Chato, J. C. (1962). "Laminar Condensation inside horizontal and inclined tubes." ASHRAE Journal: 52-60.

[5] Chen, J. C. (1966). "Correlation for Boiling Heat Transfer to Saturated Fluids in Convective Flow." Industrial & engineering chemistry process design and development **5**(3): 322-329.

[6] Chen, M. M. (1961). "An Analytical Study of Laminar Film Condensation: Part 1 -- Flat Plates." Journal of Heat Transfer (Transactions of the ASME) **83**: 48-54.

[7] Chen, S. J., J. G. Reed, et al. (1984). "Reflux condensation in a two-phase closed thermosyphon." International Journal of Heat and Mass Transfer **27**(9): 1587-1594.

[8] Collier, J. G. (1972). Convective Boiling and Condensation. London, McGraw-Hill.

[9] Dhir, V. and J. Lienhard (1971). "Laminar Film Condensation on Plane and Axisymmetric Bodies in Nonuniform Gravity." Journal of Heat Transfer (Transactions of the ASME): 97-100.

[10] Dobran, F. (1985). "Heat transfer in an Annular Two-Phase Flow." Journal of Heat Transfer (Transactions of the ASME) **107**: 472-476.

[11] Dobran, F. (1985). "Steady-state characteristics and stability thresholds of a closed two-phase thermosyphon." International Journal of Heat and Mass Transfer **28**(5): 949-957.

[12] Forster, H. K. and N. Zuber (1955). "Dynamics of vapor Bubbles and boiling heat transfer." Journal of AIChE **1**(4): 531-535.

[13] Gross, U. (1992). "Reflux Condensation Heat-Transfer inside a Closed Thermosiphon." International Journal of Heat and Mass Transfer **35**(2): 279-294.

[14] Gungor, K. E. and R. H. S. Winterton (1986). "A General Correlation for Flow Boiling in Tubes and Annuli." International Journal of Heat and Mass Transfer **29**(3): 351-358.

[15] Gungor, K. E. and R. H. S. Winterton (1987). "Simplified General Correlation for Saturated Flow Boiling and Comparisons of Correlations with Data." Chemical Engineering Research & Design **65**(2): 148-156.

[16] Harley, C. and A. Faghri (1994). "Complete Transient two-dimensional analysis of two-phase closed thermosyphons including the falling condensate film." Journal of Heat Transfer (Transactions of the ASME) **116**(2): 418-426.

[17] Kamminga, W. (1980). "An analytic solution of the film thickness of laminar film condensation on inclined pipes." International Journal of Heat and Mass Transfer **23**: 1291-1293.

[18] Kandlikar, S. G. (1990). "A General Correlation for Saturated 2-Phase Flow Boiling Heat-Transfer inside Horizontal and Vertical Tubes." Journal of Heat Transfer-Transactions of the ASME **112**(1): 219-228.

[19] Lee, Y. and U. Mital (1972). "A Two-phase closed thermosyphon." International Journal of Heat and Mass Transfer **13**(9): 1695-1707.

[20] Liu, Z. and R. H. S. Winterton (1991). "A General Correlation for Saturated and Subcooled Flow Boiling in Tubes and Annuli, Based on a Nucleate Pool Boiling Equation." International Journal of Heat and Mass Transfer **34**(11): 2759-2766.

[21] Park, C. Y. and P. S. Hrnjak (2005). "Flow boiling heat transfer of CO2 at low temperatures in a horizontal smooth tube." Journal of Heat Transfer-Transactions of the ASME **127**(12): 1305-1312.

[22] Park, C. Y. and P. S. Hrnjak (2007). "CO2 and R410A flow boiling heat transfer, pressure drop, and flow pattern at low temperatures in a horizontal smooth tube." International Journal of Refrigeration-Revue Internationale Du Froid **30**(1): 166-178.

[23] Reed, J. G. (1985). Analytical modeling of two-phase closed thermosyphon. Department of Mechanical Engineering. Berkeley, University of California, Berkeley. **Ph.D.:** 145.

[24] Reed, J. G. (1987). "Modeling of the two-phase closed thermosyphon." Journal of Heat Transfer (Transactions of the ASME) **109**(3): 9.

[25] Rohsenow, W. M. (1956). "Heat transfer and temperature distribution in laminar film condensation." Journal of Heat Transfer (Transactions of the ASME) **78**: 1645-1648.

[26] Sparrow, E. M. (1959). "A boundary layer treatment of laminar film condensation." Journal of Heat Transfer (Transactions of the ASME) **81**: 13-18.

[27] Spendel, T. (1981). Laminar Film condensation Heat Transfer in Closed Two-Phase Thermosyphons. 4th International Heat Pipe Conference, London, UK.

[28] Steiner, H., A. Kobor, et al. (2005). "A wall heat transfer model for subcooled boiling flow." International Journal of Heat and Mass Transfer **48**(19-20): 4161-4173.

[29] Thome, J. R. and J. El Hajal (2004). "Flow boiling heat transfer to carbon dioxide: general prediction method." International Journal of Refrigeration-Revue Internationale Du Froid **27**(3): 294-301.

[30] Tien, C. L. and A. R. Rohani (1974). "Analysis of the effects of vapour pressure drop on heat pipe performance." International Journal of Heat and Mass Transfer **17**: 61-67.

[31] Wang, J. C. Y. and Y. W. Ma (1991). "Condensation Heat-Transfer inside Vertical and Inclined Thermosiphons." Journal of Heat Transfer-Transactions of the ASME **113**(3): 777-780.

[32] Xu, J. and D. Goering (2008). Theroetical and experimental analysis of two-phase thermosyphons. Department of Mechanical Engineering. Fairbanks, University of Alaska Fairbanks. **Ph.D.:** 200.

[33] Xu, J. and D. J. Goering (2008). "Experimental validation of passive permafrost cooling systems." Cold Regions Science and Technology.

[34] Yun, R., Y. Kim, et al. (2005). "Convective boiling heat transfer characteristics of CO2 in microchannels." International Journal of Heat and Mass Transfer **48**(2): 235-242.

[35] Zhang, W. Z., T. Hibiki, et al. (2005). "Correlation for flow boiling heat transfer at low liquid Reynolds number in small diameter channels." Journal of Heat Transfer-Transactions of the ASME **127**(11): 1214-1221.

[36] Zuo, Z. J. and F. Gunnerson (1994). "Numerical modeling of the steady-state two-phase closed thermosyphon." International Journal of Heat and Mass Transfer **37**(17): 2715-2722.

[37] Zuo, Z. J. and F. Gunnerson (1995). "Heat transfer analysis of an inclined two-phase closed thermosyphon." Journal of Heat Transfer (Transactions of the ASME) **117**(4): 1073-1075.

Chapter 7 General Conclusions and Recommendations for Future Work

7.1 Conclusions

7.1.1 Laboratory experiments on carbon dioxide condensation

A laboratory experiment to study carbon dioxide condensation in an inclined steel pipe under very small heat flux conditions was carried out. The condensation was observed to occur in a filmwise fashion. Under the experimental conditions used, carbon dioxide is very close to its critical point. As a result, the density difference between the liquid and vapor phases and the latent heat are relatively small. The condensation mechanism under these conditions can be quite different from the fully developed condensation that can be predicted well by Nusselt's theory. The assumption that the liquid condensate film presents the primary resistance to heat flow, which is widely adopted in modeling, does not hold in this case. The thermal resistance of vapor convection cannot be neglected when comparing with the thermal conduction in the condensate film. An experimental correlation is proposed with a superposition method to include both the convection and condensation effects. Over the range of the experiments, the correlation shows good agreement with the experimental data.

7.1.2 Full scale field tests

A full scale field test of hairpin thermosyphon performance in a roadway embankment test section was carried out as part of the Thompson Drive project. The operation of these thermosyphons during the winter months transfers heat from the road embankment foundation to the road surface and rejects it to the cold ambient air. This heat release enhances frost sublimation from the surface of the road and generally results in dark strips on the road surface. The temperature and heat flux data show that the hairpin thermosyphons are only active during the winter time; they start up and shut down automatically when the temperature difference between the evaporator and condenser varies seasonally. The data clearly verify the ability of the hairpin thermosyphon to transfer heat from the evaporator to the condenser during winter months and show that

the heat transfer ceases during summer when the condenser is at higher temperature than the evaporator. This behavior is responsible for the thermal diode effect and the resulting cooling of the foundation soils.

7.1.3 Modeling of inclined two-phase thermosyphon

A quasi one-dimensional model for inclined long thermosyphons with carbon dioxide as the working fluid was developed to predict their overall heat transfer performance. The shallow inclination, low heat flux rates, and the 2D numerical cross section by cross section analysis distinguished this model from previous comprehensive models. The current model can be used to predict hairpin thermosyphon performance in the road embankment stabilization applications in permafrost areas. The comparison of the model prediction with the full scale road test data shows fairly good agreement over the range of hairpin thermosyphon operation.

7.2 Recommendations for Future Work

7.2.1 Laboratory experiment on carbon dioxide boiling and evaporation

As one of the complex processes in the thermosyphon operation, the carbon dioxide evaporation process in the evaporator is still quite difficult to simulate. Under small heat flux conditions, nucleate boiling may not occur and the convection of liquid carbon dioxide might have a large influence on heat removal from the evaporator wall. The phase change process may only occur on the liquid vapor interface in the form of evaporation. These features of the evaporator behavior could be investigated in a laboratory experiment. What's more, more accurate heat transfer correlations could be developed to describe this process for utilization in thermosyphon modeling.

7.2.2 Study on the circumferential variation of condensate heat transfer

One finding from the laboratory experiment on carbon dioxide condensation is a circumferential variation of heat transfer coefficient. One possible reason for this variation is a circumferential vapor convection driven by density difference. Another

possible reason is the uneven condensate distribution and velocity profile on the condenser perimeter. Experiments with advanced measurements showing vapor temperature difference across the vapor core or numerical simulations with accurate modeling of the condensation process inside the condenser will help reveal the actual causation of this circumferential variation.

7.2.3 3D numerical modeling

One limitation of the current thermosyphon model results from the long pipe assumption. When the thermosyphon is short, the flow field is not one-dimensional, and the velocities in the x and y directions are too large to be neglected. Even for a long thermosyphon, this situation can occur at the far end of the condenser where the bulk mass flow rate is reduced and the radical velocity cannot be neglected. Under these circumstances, a 3D numerical model is necessary to accurately predict the flow and heat transfer processes. This type of 3D modeling could possibly be done with commercial CFD software like FLUENT. One major difficulty would be the method used to describe the phase change phenomenon in the numerical model. On the liquid-vapor interface very fine grids are generally required to reveal the interface location and the film growth. However, the large mass and energy source due to the phase change process can destabilize the simulation and, thus, convergence may be hard to achieve. Innovative methods will be needed to accomplish this.

7.2.4 Comprehensive embankment model of thermosyphon

The performance of the thermosyphon depends not only on its internal processes, but also on the heat transfer occurring outside its boundary. Simplified temperature or heat flux boundary conditions cannot accurately reflect the real working conditions of the thermosyphon. A better way to predict thermosyphon performance would be a comprehensive coupled model including not only the thermosyphon itself but also the embankment materials surrounding it. What's more, the transient effect should probably

be considered because the data from Thompson Drive shows that the thermosyphon and embankment are impacted by transient conditions most of the time.

Appendices

Appendix A User defined functions in FLUENT

```
/* ex_integrate.c */


#include "stdio.h"
#include "udf.h"
#include "math.h"

real s_l, s_v, y_lv, dt;

DEFINE_INIT(initrate, d)
{
    s_l=1.0;
    s_v=-1.0;
    y_lv=-0.4;
    dt=273.15;
}

DEFINE_SOURCE(liquid_source, c,t,dS,eqn)
{
    return s_l;
}

DEFINE_SOURCE(vapor_source, c,t,dS,eqn)
{
    return s_v;
}

DEFINE_EXECUTE_AT_END(Cal_Integration)
{

    Domain *d;
    Thread *t;
    real xc[ND_ND], x,y;       /* Position of the cell */
    real sum_vapor=0.; /* Integrate vapor temperature. */
    real sum_liquid=0.;        /* Integrate liquid temperature */
    real error;
    real coeff;
    real un_relax;
    cell_t c;

    FILE *OutFile;
    OutFile = fopen("v_profile.txt", "w");
    if (OutFile == NULL){
        Message("Cannot Open v_profile.txt file! \n");
        return;
    }

    d = Get_Domain(1);         /* mixture domain if multiphase */

    thread_loop_c(t,d){
        if (SOLID_THREAD_P(t)){
            begin_c_loop(c,t)

                C_CENTROID(xc,c,t);
                x=xc[0];
                y=xc[1];
                fprintf(OutFile, "%d   %e   %e   %e\n", c, x, y, C_T(c,t)-dt);
                if (y>=y_lv) sum_vapor += (C_T(c,t)-dt) * C_VOLUME(c,t);
                else sum_liquid += (C_T(c,t)-dt) * C_VOLUME(c,t);
```

```
        end_c_loop(c,t)
      }
    }

    fclose(OutFile);

    sum_vapor *= 0.0798;
    error = (-sum_vapor - sum_liquid)*100./fabs(sum_liquid);
    un_relax = 0.5;
    coeff = 100./(un_relax*error+100.);

    printf("Vapor Integral: %g,      Liquid Integral: %g\n", sum_vapor, sum_liquid);
    printf("Error level:    %g\%,      Revise Coeff:    %g\n",error, coeff);
    printf("s_l:            %g\n", s_l);
    printf("s_v:            %g\n", s_v);
    s_v *= coeff;

    fflush(stdout);
}
```

Appendix B Main programming in Borland C++

```
//---------------------------------------------------------------------------
// --- di_main.h ---
//---------------------------------------------------------------------------

#include <stdio.h>
#include <math.h>
#include <iostream.h>
#include <iomanip.h>
#include <conio.h>
#include <fstream.h>
#include "cv_class.h"
```

```
//---------------------------------------------------------------------------
// --- di_main.cpp ---
//---------------------------------------------------------------------------

#pragma hdrstop
#include "di_main.h"
#pragma argsused

#define N_E 100        // The evaporator will be cut into 1000 C.V.
#define N_C 100      // The condenser will be cut into 1000 C.V.
#define N_A 21      // The I-section will be cut into 1000 C.V.  Better be odd
#define C_C 1e-5    // The convergence criteria
#define U_R0.01     // The under relaxation coefficient

int main(int argc, char* argv[])
{
    // Variable definition ***
    ControlVolume Cv_E[N_E];
    ControlVolume Cv_C[N_C];
    ControlVolume Cv_A[N_A];
    double OD, ID;                      // (m) The outer diameter and inner diameter
    double Len_E, Len_C, Len_A;         // (m) The L of evaporator, condenser and I-section
    double theta;                       // (°) The inclination angle
    double T, Tw_E, Tw_C;               // (°C) The temperature of working, evaporator wall
                                        //      and condenser wall
    double K;                           // thermal conductivity of the wall material
    int i;                              // index
    int LastFilm, middle;               // the last_film and middle of the CV index
    double mass, m, m_rest;             // (kg) The mass of working fluid, the mass not in
                                        // the pool and the mass in the pool
    double len_p, len_pp;               // the length of full liquid pool and partial pool
    double A_pool;                      // the phase change area in the liquid pool
    double h_pool;                      // the boiling coefficient in the liquid pool
    double m_dot_pool;                  // the evaporator rate in the liquid pool
    double T_pool;                      // the temperature of the pool liquid
    double heat_C, heat_A, heat_E;      // the overall heat of all three sections
    double mass_C, mass_A, mass_E;      // the overall mass storage of all three sections

    // Input known parameters ***
    Tw_E=-6;
    Tw_C=-8;
    T=(Tw_E+Tw_C)/2.0;
    K = 45.0;

    OD=0.089;
    ID=0.078;

    Len_E = 17.0;
    Len_C = 10.0;
    Len_A = 2.0;
    theta = 3*PI/180;

    mass = 0.66*PI*ID*ID*Len_E*1000.0/4.0;

    // initiate the condenser
    for (i = 0; i < N_C; i++) {
        // initiate the geometry parameters
        Cv_C[i].GeoIni(i, ID, OD, Len_C/N_C, 'C', 0.0, theta);
        // initiate the thermal parameters
        Cv_C[i].ThermalIni(Tw_C, T, K);
        // initaiate the condensation
        Cv_C[i].CoefficientIni(100.0/*6000.0*/);
    }
    // initiate the idiabatic section
    for (i = 0; i < N_A; i++) {
        Cv_A[i].GeoIni(i, ID, OD, Len_A/N_A, 'A', Len_C, theta);
        Cv_A[i].ThermalIni(T, T, K);
```

```
    Cv_A[i].CoefficientIni(100.0);
}
// initiate the evaproator
for (i = 0; i < N_E; i++) {
    Cv_E[i].GeoIni(i, ID, OD, Len_E/N_E, 'E', Len_C+Len_A, theta);
    Cv_E[i].ThermalIni(Tw_E, T, K);
    Cv_E[i].CoefficientIni(100.0);
}
// *************************

// the initial calculation of the mass flow
// the total mass in the vapor and film section
m = 0;

// the first control volume of condenser has 0 input mass flow
Cv_C[0].m_dot_z = 0.0;

for (i = 0; i < N_C-1; i++) {
    // M_dot() determine the mass flow increase due to the condensation
    // in this section (control volume) of condenser
    // the overall heat flow rate in this section is also determined
    Cv_C[i].M_dot();

    // the mass flow at the outlet of the No.(i) comtrol volume is the
    // mass flow at the entrance of the No.(i+1) control volume
    Cv_C[i+1].m_dot_z=Cv_C[i].m_dot_zdz;
}
// the last control volume of the condenser
Cv_C[N_C-1].M_dot();

// this loop determine the film thickness and mass accumulation
// in each control volume in the condenser
for (i = 0; i < N_C; i++) {
    // this function determine the film thickness of the control volume
    // based on the center flow rate of the C.V.
    // the geometry of the flow is also determined,
    // and the pressure gradient in this C.V. also.
    Cv_C[i].m2H();

    // this will determine the overall mass in the control volume
    // including the vapor and the condensate
    Cv_C[i].H2m();

    // sum up all the mass in the condenser
    m += Cv_C[i].m;
}

// the inlet mass flow of the adiabatic section is the same as
// the outlet of the condenser
Cv_A[0].m_dot_z=Cv_C[N_C-1].m_dot_zdz;

// do the same for the adiabatic section as in the condener,
// except no condensation is occuring
for (i = 0; i < N_A-1; i++) {
    Cv_A[i].M_dot();
    Cv_A[i+1].m_dot_z=Cv_A[i].m_dot_zdz;
}
Cv_A[N_A-1].M_dot();

for (i = 0; i < N_A; i++) {       // the mass in adiabatic section
    Cv_A[i].m2H();
    Cv_A[i].H2m();
    m += Cv_A[i].m;
}

// the inlet mass flow of the evaporator is the same as
// the outlet of the adiabatic section
```

```
Cv_E[0].m_dot_z=Cv_A[N_A-1].m_dot_zdz;

// try to do the same as in the condenser and the adiabatic section
// the only difference here is that the liquid film is getting
// thinner and may be evaporated completely.
// it can also reach the liquid pool before it get to the bottom.
for (i = 0; i < N_E-1; i++) {
    // the mass source
    Cv_E[i].M_dot();
    // the inlet mass flow of nect control volume
    Cv_E[i+1].m_dot_z=Cv_E[i].m_dot_zdz;
    // the film thickness of this C.V.
    Cv_E[i].m2H();
    // the mass cumulation in the C.V.
    Cv_E[i].H2m();
    // overall mass in the upstream.
    m += Cv_E[i].m;

    // So, the left mass in the system is:
    m_rest = mass - m;

    // this section is a tentative progress to see if the mass left
    // is much enough to form a pool that can cover the rest
    // of the evaporator
    double v_rest;
    v_rest=m_rest / Cv_E[i].wf.density_L;

    // compare the v_rest with the volume of a complete partial pool
    if ( v_rest >= PI*pow(ID,3)/(8.0*tan(theta)) ) {
        // So, a full pool
        len_pp =  ID/tan(theta);
        len_p =  ( m_rest/Cv_E[N_E-1].wf.density_L -
        PI*pow(ID,3)/(8.0*tan(theta)) )/(PI*ID*ID/4.0);
    }
    else {
        // So, a partial pool
        // iteration to get the right h
        double v_t, h;
        h = ID/2;
        //v_t = h2v(h, ID/2, theta);
        v_t =(pow(ID/2,2)*sqrt(h*(ID-h))-0.25*ID*ID*(0.5*ID-h)*acos((0.5*ID-
        h)/(0.5*ID))
            -pow(h*(2*2-h),1.5)/3)/tan(theta);
        //v_t =(pow(ID/2,2)*sqrt(h*(2*r-h))-r*r*(r-h)*acos((r-h)/r)-pow(h*(2*2-
        h),1.5)/3)/tan(theta);

        // regress to find the right h
        while ( fabs(v_t-v_rest)/v_rest>=1e-6 ){
            h=h*v_rest/v_t;
        }
        len_p=0;
        // the length of the liquid pool (a partial pool)
        len_pp=h/tan(theta);
    }

    // judge if the pool and film will cover the full evaporator
    // if it do, the loop will stop and the index of the last C.V.
    // that is not in the liquid pool is given.
    // if not, the film will reach deeper into the evaporator to
    // the next control volume.
    double coverage;
    coverage = len_p+len_pp+(i+1)*Len_E/N_E;
    if ((coverage>=Len_E) && (coverage<=Len_E+Len_E/N_E)) {
        // the index of the last C.V. that is not in the pool
        LastFilm = i;
        // the properties of the last film C.V. is used for the liqui pool
        //h_pool = Cv_E[LastFilm].h;
```

```
        h_pool = Cv_E[LastFilm].h;
        T_pool = Cv_E[LastFilm].T;
        break;
    }
}

// the wet area of the liquid pool, this area is the boiling surface
if (len_p >= 0) {
    A_pool = PI*ID*len_p + PI*ID*len_pp/2.0;
}
else{
    double H;
    H=len_pp*tan(theta);
    A_pool = (ID/tan(theta))*(sqrt(H*(ID-H))-(ID/2-H)*acos(2*(ID/2-H)/ID));
}

// the mass flow rate at the outlet of the liquid pool
m_dot_pool = A_pool*h_pool*(Tw_E-T_pool)/Cv_E[LastFilm].wf.latent_heat;

// This patches the pressure gradient as zero
for (i = LastFilm; i < N_E; i++) {
    Cv_E[i].pg = 0.0;
}

// adjust the working temperature to balance the mass flow rate
while (fabs((m_dot_pool-Cv_E[LastFilm].m_dot_zdz)/Cv_E[LastFilm].m_dot_zdz)>=1e-5 ){

    // First adjust the adiabatic section, temperature, pressure gradient, and
       properties;
    T = T + U_R*((m_dot_pool-
       Cv_E[LastFilm].m_dot_zdz)/Cv_E[LastFilm].m_dot_zdz)*(Tw_E-Tw_C);

    if (T>=Tw_E||T<=Tw_C) {
        cout << "tentative temperature goes out of limitation!"<<endl;
        cout << "Divergence!"<<endl;
        getch();
        return 1;
    }

    // The adiabatic section
    // the middle index
    middle = N_A/2;
    // the middle C.V. is under working temperature
    Cv_A[middle].T = T;
    Cv_A[middle].T2Properties();
    // distribute the pressure over the middle C.V.
    // find the working temperature for the pressure.
    Cv_A[middle].P_distribute_working();

    for (i = 1; i <= N_A/2; i++) {
        // upwards into the adiabatic section
        Cv_A[(middle-i)].p_zdz = Cv_A[(middle-i+1)].p_z;
        Cv_A[middle-i].P_distribute_upwards();
        Cv_A[middle-i].T2Properties();
        // downwards into the adiabatic section
        Cv_A[(middle+i)].p_z = Cv_A[(middle+i-1)].p_zdz;
        Cv_A[middle+i].P_distribute_downwards();
        Cv_A[middle+i].T2Properties();
    }

    // The condenser
    Cv_C[N_C-1].p_zdz = Cv_A[0].p_z;
    Cv_C[N_C-1].P_distribute_upwards();
    Cv_C[N_C-1].T2Properties();
    for (i = 2; i <= N_C; i++) {
        Cv_C[N_C-i].p_zdz = Cv_C[N_C-i+1].p_z;
        Cv_C[N_C-i].P_distribute_upwards();
```

```
    Cv_C[N_C-i].T2Properties();
}

// The evaporator
Cv_E[0].p_z = Cv_A[N_A-1].p_zdz;
Cv_E[0].P_distribute_downwards();
Cv_E[0].T2Properties();
for (i = 1; i < N_E; i++) {
    Cv_E[i].p_z = Cv_E[i-1].p_zdz;
    Cv_E[i].P_distribute_downwards();
    Cv_E[i].T2Properties();
}

m = 0;  // the total mass in the vapor and film section

Cv_C[0].m_dot_z = 0.0;
for (i = 0; i < N_C-1; i++) {
    Cv_C[i].M_dot();
    Cv_C[i+1].m_dot_z=Cv_C[i].m_dot_zdz;
}
Cv_C[N_C-1].M_dot();

for (i = 0; i < N_C; i++) {       // film thickness & the mass accumulation
    Cv_C[i].m2H();
    Cv_C[i].H2m();
    m += Cv_C[i].m;
}

Cv_A[0].m_dot_z=Cv_C[N_C-1].m_dot_zdz;
for (i = 0; i < N_A-1; i++) {
    Cv_A[i].M_dot();
    Cv_A[i+1].m_dot_z=Cv_A[i].m_dot_zdz;
}
Cv_A[N_A-1].M_dot();

for (i = 0; i < N_A; i++) {       // the mass in idiabatic section
    Cv_A[i].m2H();
    Cv_A[i].H2m();
    m += Cv_A[i].m;
}

Cv_E[0].m_dot_z=Cv_A[N_A-1].m_dot_zdz;

////////////////////////////////////////////////////////////////////
for (i = 0; i < N_E-1; i++) {
    Cv_E[i].M_dot();
    Cv_E[i+1].m_dot_z=Cv_E[i].m_dot_zdz;
    Cv_E[i].m2H();
    Cv_E[i].H2m();
    m += Cv_E[i].m;
    // So, the left mass in the system is:
    m_rest = mass - m;
    double v_rest;
    v_rest=m_rest / Cv_E[i].wf.density_L;

    if ( v_rest >= PI*pow(ID,3)/(8.0*tan(theta)) ) {
        // do something that have a full pool
        len_pp =  ID/tan(theta);
        len_p =  ( m_rest/Cv_E[N_E-1].wf.density_L -
    PI*pow(ID,3)/(8.0*tan(theta)) )/(PI*ID*ID/4.0);
    }
    else {  // partial pool
        // iteration to get the right h
        double v_t, h;
        h = ID/2;
```

```
            v_t =(pow(ID/2,2)*sqrt(h*(ID-h))-0.25*ID*ID*(0.5*ID-h)*acos((0.5*ID-
                  h)/(0.5*ID))-pow(h*(2*2-h),1.5)/3)/tan(theta);

            if (v_t <= 0) {
                cout << "close to the dry out limitation!"<<endl;
                cout << "check if the convergence of the regression!"<<endl;
                cout << endl << "Presss any key to continue! " << endl;
                getch();
                return 1;
            }

            while ( fabs(v_t-v_rest)/v_rest>=1e-6 ){
                h=h*v_rest/v_t;
            }
            len_p=0;
            len_pp=h/tan(theta);
        }

        // judge if the pool and film will cover the full evaporator
        double coverage;
        coverage = len_p+len_pp+(i+1)*Len_E/N_E;
        if ((coverage>=Len_E) && (coverage<=Len_E+Len_E/N_E)) {
            LastFilm = i;
            h_pool = Cv_E[LastFilm].h;
            //h_pool = 40;
            //h_pool = 10*Cv_E[LastFilm].wf.thermal_conductivity_L/ID;
            T_pool = Cv_E[LastFilm].T;
            break;
        }
    }

    // This patches the pressure gradient as zero
    for (i = LastFilm; i < N_E; i++) {
        Cv_E[i].pg = 0.0;
    }

    if (len_p >= 0) {
        A_pool = PI*ID*len_p + PI*ID*len_pp/2.0;
    }
    else{
        double H;
        H=len_pp*tan(theta);
        A_pool = (ID/tan(theta))*(sqrt(H*(ID-H))-(ID/2-H)*acos(2*(ID/2-H)/ID));
    }

    m_dot_pool = A_pool * h_pool * ( Tw_E - T_pool) / Cv_E[LastFilm].wf.latent_heat;

    for (i = LastFilm; i < N_E; i++) {
        Cv_E[i].H =((i-LastFilm)*Len_E/N_E+Len_E/(2*N_E))*tan(theta);
        if (Cv_E[i].H >= ID) {
            Cv_E[i].H = ID;
        }
        Cv_E[i].h = Cv_E[LastFilm].h;
        Cv_E[i].m = 0;
        Cv_E[i].pg = 0;
        Cv_E[i].pg_real = 0;
        Cv_E[i].T = Cv_E[LastFilm].T;
        Cv_E[i].Pool_heat();
    }


    //WT=0;
// end of the while loop
}

// the "after" calculations
heat_C=heat_A=heat_E=0;
```

```
mass_C=mass_A=mass_E=0;
for (i = 0; i < N_C; i++) {
    heat_C += Cv_C[i].Q ;
    mass_C += Cv_C[i].m ;
}
for (i = 0; i < N_A; i++) {
    heat_A += Cv_A[i].Q ;
    mass_A += Cv_A[i].m ;
}
for (i = 0; i < LastFilm; i++) {
    heat_E += Cv_E[i].Q ;
    mass_E += Cv_E[i].m ;
}
heat_E += h_pool*(T_pool - Tw_E)*A_pool;
mass_E += m_rest;

// all the output routines
//out2file();
ofstream Sout, Dout;
Sout.open("Sumout.dat",ios::out);
Dout.open("Detailout.dat", ios::out);
if (Sout.fail()||Dout.fail()){
    cout<<"Fail in the file openning!"<<endl;
    getch();
    return 1;
}
Sout<< setiosflags(ios::left);
Sout<< "Thermosyphon modeling results summary"<< endl << endl;

Sout<< setw(26)<< "Working temperature(C):" << setw(10)<<setprecision(3)<<T;
Sout<< setw(26)<< "Working pressure(Pa):" <<setw(10)<<setprecision(8)
       <<Cv_A[middle].wf.sat_pressure<<endl;
Sout<< setw(26)<< "Condenser wall T.(C):" << setw(10)<<setprecision(3)<<Tw_C;
Sout<< setw(26)<< "Evaporator wall T.(C):" << setw(10)<<setprecision(3)<<Tw_E<< endl;
Sout<< setw(26)<< "Pressure drop(Pa):" << setw(10)<<setprecision(3)
       <<Cv_E[LastFilm].wf.sat_pressure-Cv_C[0].wf.sat_pressure<< endl;
Sout<<endl;

Sout<< "-------------------------------------------------------------------------------"
       <<endl;
Sout<< "Condenser:"<<endl;
Sout<< "-------------------------------------------------------------------------------"
       <<endl;
Sout<< setw(26)<< "Length(m):" << setw(10)<<setprecision(3)<< Len_C;
Sout<< setw(26)<< "CV number:" << setw(10) << setprecision(0) << N_C << endl;
Sout<< setw(26)<< "Overall Heat Rate(W):" << setiosflags(ios::fixed)<<setw(10)
       << setprecision(2) << heat_C;
Sout<< setw(26)<< "Overall Mass Rate(g/s):" << setw(10)<< setprecision(4)
       << Cv_C[N_C-1].m_dot_zdz*1000<<endl;
Sout<< setw(26)<< "Overall Mass storage(kg):" << setw(10)<<setprecision(3)
       << mass_C<<endl;
Sout<<endl;

Dout<< "-------------------------------------------------------------------------------"
       <<endl;
Dout<< "Condenser:"<<endl;
Dout<< "-------------------------------------------------------------------------------"
       <<endl;
Dout<<setw(6)<<"Index"<<setw(5)<<"LCT"<<setw(7)<<"Z(m)"<<setw(10)<<"P(Mpa)";
Dout<<setw(10)<<"T(C)"<<setw(8)<<"H(mm)"<<setw(10)<<"m(kg)"<<setw(12)<<"pg(Pa/m)"
       <<setw(12)<<"pg_r(Pa/m)"<<setw(10)<<"Q(W)"<<endl;
for (i = 0; i < N_C; i++) {
    Dout<<setw(6)<<Cv_C[i].index;
    Dout<<setw(5)<<Cv_C[i].where;
    Dout<< setiosflags(ios::fixed)<<setw(7)<<setprecision(3)<<Cv_C[i].z;
    Dout<< setiosflags(ios::fixed)<<setw(10)<<setprecision(6)<<Cv_C[i].p*1e-6;
    Dout<< setiosflags(ios::fixed)<<setw(10)<<setprecision(3)<<Cv_C[i].T;
```

```
    Dout<< setiosflags(ios::fixed)<<setw(8)<<setprecision(4)<<Cv_C[i].H*1000;
    Dout<< setiosflags(ios::fixed)<<setw(10)<<setprecision(3)<<Cv_C[i].m;
    Dout<< setiosflags(ios::fixed)<<setw(12)<<setprecision(5)<<Cv_C[i].pg;
    Dout<< setiosflags(ios::fixed)<<setw(12)<<setprecision(7)<<Cv_C[i].pg_real;
    Dout<< setiosflags(ios::fixed)<<setw(10)<<setprecision(3)<<Cv_C[i].Q<<endl;
}

Sout<< "--------------------------------------------------------------------------------"
       <<endl;
Sout<< "Adiabatic Section:" <<endl;
Sout<< "--------------------------------------------------------------------------------"
       <<endl;
Sout<< setiosflags(ios::left)<< setw(26)<< "Length(m):" << setw(10)<<setprecision(3)
       << Len_A;
Sout<< setw(26)<< "CV number:" << setw(10) << setprecision(0) << N_A << endl;
Sout<< setw(26)<< "Overall Heat Rate(W):" << setiosflags(ios::fixed)<<setw(10)
       << setprecision(2) << heat_A;
Sout<< setw(26)<< "Overall Mass Rate(g/s):" << setw(10)<< setprecision(4)
       << Cv_A[N_A-1].m_dot_zdz*1000<<endl;
Sout<< setw(26)<< "Overall Mass storage(kg):" << setw(10)<<setprecision(3)
       << mass_A<<endl;
Sout<<endl;

Sout<<setw(6)<<"Index"<<setw(5)<<"LCT"<<setw(7)<<"Z(m)"<<setw(10)<<"P(Mpa)";
Sout<<setw(10)<<"T(C)"<<setw(10)<<"H(mm)"<<setw(10)<<"m(kg)"<<setw(10)<<"pg(Pa/m)"
       <<setw(10)<<"Q(W)"<<endl;

Dout<< endl;
Dout<< "--------------------------------------------------------------------------------"
       <<endl;
Dout<< "Adiabatic Section:" <<endl;
Dout<< "--------------------------------------------------------------------------------"
       <<endl;
Dout<<setw(6)<<"Index"<<setw(5)<<"LCT"<<setw(7)<<"Z(m)"<<setw(10)<<"P(Mpa)";
Dout<<setw(10)<<"T(C)"<<setw(8)<<"H(mm)"<<setw(10)<<"m(kg)"<<setw(12)<<"pg(Pa/m)"
       <<setw(12)<<"pg_r(Pa/m)"<<setw(10)<<"Q(W)"<<endl;

for (i = 0; i < N_A; i++) {
    Dout<<setw(6)<<Cv_A[i].index;
    Dout<<setw(5)<<Cv_A[i].where;
    Dout<< setiosflags(ios::fixed)<<setw(7)<<setprecision(3)<<Cv_A[i].z;
    Dout<< setiosflags(ios::fixed)<<setw(10)<<setprecision(6)<<Cv_A[i].p*1e-6;
    Dout<< setiosflags(ios::fixed)<<setw(10)<<setprecision(3)<<Cv_A[i].T;
    Dout<< setiosflags(ios::fixed)<<setw(8)<<setprecision(4)<<Cv_A[i].H*1000;
    Dout<< setiosflags(ios::fixed)<<setw(10)<<setprecision(3)<<Cv_A[i].m;
    Dout<< setiosflags(ios::fixed)<<setw(12)<<setprecision(5)<<Cv_A[i].pg;
    Dout<< setiosflags(ios::fixed)<<setw(12)<<setprecision(7)<<Cv_A[i].pg_real;
    Dout<< setiosflags(ios::fixed)<<setw(10)<<setprecision(3)<<Cv_A[i].Q<<endl;
}

Sout<<endl;
Sout<< "--------------------------------------------------------------------------------"
       <<endl;
Sout<< "Evaporator:" <<endl;
Sout<< "--------------------------------------------------------------------------------"
       <<endl;
Sout<< setiosflags(ios::left)<< setw(26)<< "Length(m):" << setw(10)<<setprecision(3)
       << Len_E;
Sout<< setw(26)<< "CV number:" << setw(10) << setprecision(0) << N_E << endl;
Sout<< setw(26)<<"Full Length of Pool(m):" << setw(10)<<setprecision(3)<<len_p;
Sout<< setw(26)<<"Partial Pool Length(m):" << setw(10)<<setprecision(3)<<len_pp<<endl;
Sout<< setw(26)<< "Overall Heat Rate(W):" << setiosflags(ios::fixed)<<setw(10)
       << setprecision(2) << heat_E;
Sout<< setw(26)<< "Overall Mass Rate(g/s):" << setw(10)<< setprecision(4)
       << Cv_E[0].m_dot_z*1000<<endl;
Sout<< setw(26)<< "Overall Mass storage(kg):" << setw(10)<<setprecision(3)
       << mass_E<<endl;
```

```
Dout<<endl;
Dout<< "------------------------------------------------------------------------------"
       <<endl;
Dout<< "Evaporator:" <<endl;
Dout<< "------------------------------------------------------------------------------"
       <<endl;
Dout<<setw(6)<<"Index"<<setw(5)<<"LCT"<<setw(7)<<"Z(m)"<<setw(10)<<"P(Mpa)";
Dout<<setw(10)<<"T(C)"<<setw(8)<<"H(mm)"<<setw(10)<<"m(kg)"<<setw(12)<<"pg(Pa/m)"
       <<setw(12)<<"pg_r(Pa/m)"<<setw(10)<<"Q(W)"<<endl;
for (i = 0; i < LastFilm; i++) {
    Dout<<setw(6)<<Cv_E[i].index;
    Dout<<setw(5)<<Cv_E[i].where;
    Dout<< setiosflags(ios::fixed)<<setw(7)<<setprecision(3)<<Cv_E[i].z;
    Dout<< setiosflags(ios::fixed)<<setw(10)<<setprecision(6)<<Cv_E[i].p*1e-6;
    Dout<< setiosflags(ios::fixed)<<setw(10)<<setprecision(3)<<Cv_E[i].T;
    Dout<< setiosflags(ios::fixed)<<setw(8)<<setprecision(4)<<Cv_E[i].H*1000;
    Dout<< setiosflags(ios::fixed)<<setw(10)<<setprecision(3)<<Cv_E[i].m;
    Dout<< setiosflags(ios::fixed)<<setw(12)<<setprecision(5)<<Cv_E[i].pg;
    Dout<< setiosflags(ios::fixed)<<setw(12)<<setprecision(7)<<Cv_E[i].pg_real;
    Dout<< setiosflags(ios::fixed)<<setw(10)<<setprecision(3)<<Cv_E[i].Q<<endl;
}

Sout.close();
Dout.close();

//out2monitor();
cout<< "Thermosyphon modeling results"<< endl;

cout<< "------------------------------------------------------------------------------"
       <<endl;
cout<< "Condenser:"<<endl;
cout<< "------------------------------------------------------------------------------"
       <<endl;

cout<< setiosflags(ios::left);
cout<<setw(6)<<"Index"<<setw(5)<<"LCT"<<setw(7)<<"Z(m)"<<setw(10)<<"P(Mpa)";
cout<<setw(10)<<"T(C)"<<setw(8)<<"H(mm)"<<setw(10)<<"m(kg)"<<setw(12)<<"pg(Pa/m)"
       <<setw(10)<<"Q(W)"<<endl;

for (i = 0; i < N_C; i++) {
    cout<<setw(6)<<Cv_C[i].index;
    cout<<setw(5)<<Cv_C[i].where;
    cout<< setiosflags(ios::fixed)<<setw(7)<<setprecision(3)<<Cv_C[i].z;
    cout<< setiosflags(ios::fixed)<<setw(10)<<setprecision(6)<<Cv_C[i].p*1e-6;
    cout<< setiosflags(ios::fixed)<<setw(10)<<setprecision(3)<<Cv_C[i].T;
    cout<< setiosflags(ios::fixed)<<setw(8)<<setprecision(4)<<Cv_C[i].H*1000;
    cout<< setiosflags(ios::fixed)<<setw(10)<<setprecision(3)<<Cv_C[i].m;
    cout<< setiosflags(ios::fixed)<<setw(12)<<setprecision(5)<<Cv_C[i].pg;
    cout<< setiosflags(ios::fixed)<<setw(10)<<setprecision(3)<<Cv_C[i].Q;
    cout<< endl;
}
cout<<endl;
COUT<< "------------------------------------------------------------------------------"
       <<endl;
cout<< "Adiabatic Section:" <<endl;
cout<< "------------------------------------------------------------------------------"
       <<endl<<endl;

cout<<setw(6)<<"Index"<<setw(5)<<"LCT"<<setw(7)<<"Z(m)"<<setw(10)<<"P(Mpa)";
cout<<setw(10)<<"T(C)"<<setw(8)<<"H(mm)"<<setw(10)<<"m(kg)"<<setw(12)<<"pg(Pa/m)"
       <<setw(10)<<"Q(W)"<<endl;

for (i = 0; i < N_A; i++) {
    cout<<setw(6)<<Cv_A[i].index;
    cout<<setw(5)<<Cv_A[i].where;
    cout<< setiosflags(ios::fixed)<<setw(7)<<setprecision(3)<<Cv_A[i].z;
```

```
    cout<< setiosflags(ios::fixed)<<setw(10)<<setprecision(6)<<Cv_A[i].p*1e-6;
    cout<< setiosflags(ios::fixed)<<setw(10)<<setprecision(3)<<Cv_A[i].T;
    cout<< setiosflags(ios::fixed)<<setw(8)<<setprecision(4)<<Cv_A[i].H*1000;
    cout<< setiosflags(ios::fixed)<<setw(10)<<setprecision(3)<<Cv_A[i].m;
    cout<< setiosflags(ios::fixed)<<setw(12)<<setprecision(5)<<Cv_A[i].pg;
    cout<< setiosflags(ios::fixed)<<setw(10)<<setprecision(3)<<Cv_A[i].Q;
    cout<< endl;
}

cout<<endl;
cout<< "-------------------------------------------------------------------------------"
       <<endl;
cout<< "Evaporator:" <<endl;
cout<< "-------------------------------------------------------------------------------"
       <<endl;
cout<<setw(6)<<"Index"<<setw(5)<<"LCT"<<setw(7)<<"Z(m)"<<setw(10)<<"P(Mpa)";
cout<<setw(10)<<"T(C)"<<setw(8)<<"H(mm)"<<setw(10)<<"m(kg)"<<setw(12)<<"pg(Pa/m)"
       <<setw(10)<<"Q(W)"<<endl;
for (i = 0; i < LastFilm; i++) {
    cout<<setw(6)<<Cv_E[i].index;
    cout<<setw(5)<<Cv_E[i].where;
    cout<< setiosflags(ios::fixed)<<setw(7)<<setprecision(3)<<Cv_E[i].z;
    cout<< setiosflags(ios::fixed)<<setw(10)<<setprecision(6)<<Cv_E[i].p*1e-6;
    cout<< setiosflags(ios::fixed)<<setw(10)<<setprecision(3)<<Cv_E[i].T;
    cout<< setiosflags(ios::fixed)<<setw(8)<<setprecision(4)<<Cv_E[i].H*1000;
    cout<< setiosflags(ios::fixed)<<setw(10)<<setprecision(3)<<Cv_E[i].m;
    cout<< setiosflags(ios::fixed)<<setw(12)<<setprecision(5)<<Cv_E[i].pg;
    cout<< setiosflags(ios::fixed)<<setw(10)<<setprecision(3)<<Cv_E[i].Q;
    cout<< endl;
}

//  summary output:
cout<< endl << endl;

cout<< "Thermosyphon modeling results summary"<< endl;

cout<< setw(26)<< "Working temperature(C):" << setw(10)<<setprecision(3)<<T;
cout<< setw(26)<< "Working pressure(Pa):" << setw(10)<<setprecision(2)
       <<Cv_A[middle].wf.sat_pressure<<endl;
cout<< setw(26)<< "Condenser wall T (C):" << setw(10)<<setprecision(3)<<Tw_C;
cout<< setw(26)<< "Evaporator wall T (C):" << setw(10)<<setprecision(3)<<Tw_E<< endl;
cout<< setw(26)<< "Pressure drop(Pa):" << setw(10)<<setprecision(3)
       <<Cv_E[LastFilm].wf.sat_pressure-Cv_C[0].wf.sat_pressure<< endl;
cout<<endl;

cout<< "-------------------------------------------------------------------------------"
       <<endl;
cout<< "Condenser:"<<endl;
cout<< "-------------------------------------------------------------------------------"
       <<endl;
cout<< setiosflags(ios::left)<< setw(26)<< "Length(m):" << setw(10)<<setprecision(3)
       << Len_C;
cout<< setw(26)<< "CV number:" << setw(10) << setprecision(0) << N_C << endl;
cout<< setw(26)<< "Overall Heat Rate(W):" << setiosflags(ios::fixed)<<setw(10)
       << setprecision(2) << heat_C;
cout<< setw(26)<< "Overall Mass Rate(g/s):" << setw(10)<< setprecision(4)
       << Cv_C[N_C-1].m_dot_zdz*1000<<endl;
cout<< setw(26)<< "Overall Mass storage(kg):" << setw(10)<<setprecision(3)
       << mass_C<<endl;

cout<<endl;
cout<< "-------------------------------------------------------------------------------"
       <<endl;
cout<< "Adiabatic Section:" <<endl;
cout<< "-------------------------------------------------------------------------------"
       <<endl;
cout<< setiosflags(ios::left)<< setw(26)<< "Length(m):" << setw(10)<<setprecision(3)
```

```
        << Len_A;
    cout<< setw(26)<< "CV number:" << setw(10) << setprecision(0) << N_A << endl;
    cout<< setw(26)<< "Overall Heat Rate(W):" << setiosflags(ios::fixed)<<setw(10)
        << setprecision(2) << heat_A;
    cout<< setw(26)<< "Overall Mass Rate(g/s):" << setw(10)<< setprecision(4)
        << Cv_A[N_A-1].m_dot_zdz*1000<<endl;
    cout<< setw(26)<< "Overall Mass storage(kg):" << setw(10)<<setprecision(3)
        << mass_A<<endl;

    cout<<endl;
    cout<< "-------------------------------------------------------------------------------"
        <<endl;
    cout<< "Evaporator:" <<endl;
    cout<< "-------------------------------------------------------------------------------
        "<<endl;
    cout<< setiosflags(ios::left)<< setw(26)<< "Length(m):" << setw(10)<<setprecision(3)
        << Len_E;
    cout<< setw(26)<< "CV number:" << setw(10) << setprecision(0) << N_E << endl;
    cout<< setw(26)<<"Full Length of Pool(m):" << setw(10)<<setprecision(3)<<len_p;
    cout<< setw(26)<<"Partial Pool Length(m):" << setw(10)<<setprecision(3)<<len_pp<<endl;
    cout<< setw(26)<< "Overall Heat Rate(W):" << setiosflags(ios::fixed)<<setw(10)
        << setprecision(2) << heat_E;
    cout<< setw(26)<< "Pool Heat Rate(W):" << setiosflags(ios::fixed)<<setw(10)
        << setprecision(2) << h_pool*(T_pool - Tw_E)*A_pool <<endl;
    cout<< setw(26)<< "Overall Mass Rate(g/s):" << setw(10)<< setprecision(4)
        << Cv_E[0].m_dot_z*1000;
    cout<< setw(26)<< "Overall Mass storage(kg):" << setw(10)<<setprecision(3)
        << mass_E<<endl<<endl;

    cout << endl << "Presss any key to continue! " << endl;
    getch();

    return 0;
}
```

```
//-----------------------------------------------------------------------------
// --- vc_class.h ---
//-----------------------------------------------------------------------------

#include <iostream.h>
#include <prop.h>
#define g 9.81
#define PI 3.1415926

class WorkingFluid
{
    private:

    public:
        double temperature;              // C
        double sat_pressure;             // Pa
        double latent_heat;              // J/kg
        double specific_volume_L;        // m^3/kg
        double specific_volume_v;        // m^3/kg
        double density_L;                // kg/m^3
        double density_V;                // kg/m^3
        double specific_heat_L;          // J/kg_K
        double specific_heat_V;          // J/kg_K
        double dynamic_viscosity_L;      // Pa_s
        double dynamic_viscosity_V;      // Pa_s
        double kinematic_viscosity_L;    // m^2/s
        double kinematic_viscosity_V;    // m^2/s
        double thermal_conductivity_L;   // W/m_K
        double thermal_conductivity_V;   // W/m_K
        double surface_tension;          // N/m

        void CO2_Properties(double t);
        void DisplayProperties();

};

class ControlVolume
{
    // All properties in this class will be dimensionless
    public:
        WorkingFluid wf;                 // the working fluid properties
        char   where;                    // the location of CV 'C','E' or 'I'
        int    index;                    // the index of this CV, from 0-1000 eg.
        double theta;                    // the inclination of the pipe (degree)

        // all variables
        double z;                        // the z coordinate (z)
        double T;                        // the temperature (T)
        double Tw, Twi;                  // the wall temperature (Tw)
        double D;                        // the inner diameter (D)
        double D_o;                      // the outer diameter (D_o)
        double H;                        // the height of the film (H)
        double dz;                       // the thickness in z direction (dz)
        double C;                        // the circumference of phase change (C)
        double m;                        // the overall mass in this CV (m)
        double m_dot;                    // the mass source in unit phase change surface
        double w_l;                      // the liquid velocity (v_l)
        double w_v;                      // the vapor velocity (v_v)
        double m_dot_z;                  // the inlet mass flow rate m_dot(z)
        double m_dot_zdz;                // the outlet mass flow rate m_dot(z+dz)
        double m_dot_center;             // the mass flow rate in the center of the C.V.
        double p_z;                      // the pressure at z (Pa)
        double p_zdz;                    // the pressure at zdz (Pa)
        double p;                        // the pressure at the middle of the control
                                         // volume (Pa)
        double pg, pg_real;              // the pressure gradient in current Control
                                         // volume (Pa/m)
```

```
        double kw;                          // the thermal conductivity of the wall
        double h;                           // the heat transfer coefficient (h)
        double Q;                           // the heat flow rate in this C.V. (W)
        double Re_v, Re_l;                  // the Reynold number for vapor phase
        double Pr_l, Pr_v;                  // the Prandtl number for liquid phase
        double Ja;                          // the Jacobe number
        double Nu;                          // the Nusselt number
        double Ra;                          // the Rayleigh namber

        double temp;
        double m_star, h_star, S_star;


    public:
        void T2Properties();
        void ThermalIni(double tw, double t, double k);
        void GeoIni(int i, double d_cv, double d_o, double delta_z, char w, double z_0,
            double alpha);
        void CoefficientIni(double h);
        void M_dot();
        void m2H();
        void H2m();
        void P_distribute_working();
        void P_distribute();
        void P_distribute_upwards();
        void P_distribute_downwards();
        void DisplayProperties(double tw, double t);
        void Pool_heat();

};
```

```
//---------------------------------------------------------------------------
// --- cv_class.cpp ---
//---------------------------------------------------------------------------
#include "cv_class.h"

void WorkingFluid::CO2_Properties(double t)
{
        temperature = t;                            // C
        sat_pressure = dSatPres(t);                 // Pa
        latent_heat = dLatHeat(t);                  // J/kg
        specific_volume_L = dSpeVolL(t);            // m^3/kg
        specific_volume_v = dSpeVolV(t);            // m^3/kg
        density_L = dDensitL(t);                    // kg/m^3
        density_V = dDensitV(t);                    // kg/m^3
        specific_heat_L = dSpeHeaL(t);              // J/kg_K
        specific_heat_V = dSpeHeaV(t);              // J/kg_K
        dynamic_viscosity_L = dDynVisL(t);          // Pa_s
        dynamic_viscosity_V = dDynVisV(t);          // Pa_s
        kinematic_viscosity_L = dKinVisL(t);        // m^2/s
        kinematic_viscosity_V = dKinVisV(t);        // m^2/s
        thermal_conductivity_L = dTheConL(t);       // W/m_K
        thermal_conductivity_V = dTheConV(t);       // W/m_K
        surface_tension = dSurTens(t);              // N/m
}

void WorkingFluid::DisplayProperties()
{
    cout<<" This is in the Working Fluid class! "<<endl;
    cout<<"t = "<<temperature<<endl<<"P = "<<sat_pressure<<endl;
}

void ControlVolume::T2Properties()
{
    wf.CO2_Properties(T);
    p = wf.sat_pressure;
}

void ControlVolume::ThermalIni(double tw, double t, double k)
{

    wf.CO2_Properties(t);
    T=t;
    Tw=tw;
    kw=k;
}

void ControlVolume::GeoIni(int i, double d_cv, double d_o, double delta_z, char w, double
          z_0, double alpha)
{
    index = i;
    z=z_0+index*delta_z+delta_z/2.0;
    H=0.0;
    D=d_cv;
    D_o=d_o;
    dz=delta_z;
    where=w;
    theta= alpha;
    if (w=='C') {
        C=PI*D;     // initial phase changing perimeter in condenser
    }
    else {
        C=0;        // initial phase changing perimeter in evaporator & I section
    }

}

void ControlVolume::CoefficientIni(double co)
```

```
{
    h=co;
}

void ControlVolume::M_dot()
{
    double R1, R2;
    R1 =  D*log(D_o/D)/(2.0*kw);              // conduction resistance
    R2 = 1.0/h;                               // convection resistance
    Q = (T-Tw)*C*dz/(R1+R2);
    m_dot = Q /(wf.latent_heat);
    m_dot_zdz=m_dot_z + m_dot;
    if (m_dot_z <= 0) {
        m_dot_z = 0;
    }
    if (m_dot_zdz <= 0) {
        m_dot_zdz =0;
    }
}


void ControlVolume::m2H()      // From mass flux to film thickness, interpolation
{
    double H_star[20], Sv_star[20], V_star[20];
    H_star[0]=0.0; H_star[1]=0.02; H_star[2]=0.04; H_star[3]=0.06;
    H_star[4]=0.08; H_star[5]=0.1; H_star[6]=0.15; H_star[7]=0.2;
    H_star[8]=0.25; H_star[9]=0.3; H_star[10]=0.35; H_star[11]=0.4;
    H_star[12]=0.45; H_star[13]=0.5; H_star[14]=0.55; H_star[15]=0.6;
    H_star[16]=0.7; H_star[17]=0.0; H_star[18]=0.0; H_star[19]=0.0;

    Sv_star[0]=0.0; Sv_star[1]=-2.00373E-05; Sv_star[2]=-0.000424612; Sv_star[3]=-
            0.00155036;
    Sv_star[4]=-0.00384707; Sv_star[5]=-0.0078631; Sv_star[6]=-0.0283144; Sv_star[7]=-
            0.0705804;
    Sv_star[8]=-0.142136; Sv_star[9]=-0.249399; Sv_star[10]=-0.398096; Sv_star[11]=-
            0.59313;
    Sv_star[12]=-0.844422; Sv_star[13]=-1.16494; Sv_star[14]=-1.57733; Sv_star[15]=-
            2.12022;
    Sv_star[16]=-3.92893; Sv_star[17]=0.0; Sv_star[18]=0.0; Sv_star[19]=0.0;

    V_star[0]=0.0; V_star[1]=2.93777E-07; V_star[2]=3.50757E-06; V_star[3]=1.40550E-05;
    V_star[4]=3.71631E-05; V_star[5]=7.86709E-05; V_star[6]=2.80906E-04;
            V_star[7]=6.53407E-04;
    V_star[8]=1.1780E-03; V_star[9]=1.7926E-03; V_star[10]=2.4115E-03; V_star[11]=2.9430E-
            03;
    V_star[12]=3.3336E-03; V_star[13]=3.5430E-03; V_star[14]=3.5623E-03;
            V_star[15]=3.4042E-03;
    V_star[16]=2.6740E-03; V_star[17]=0.0; V_star[18]=0.0; V_star[19]=0.0;

    m_dot_center = (m_dot_z + m_dot_zdz)/2.0;
    m_star = m_dot_center*wf.dynamic_viscosity_L/(pow(D,4)*pow(wf.density_L,2)
            *9.81*sin(theta) );

    for (int i = 1; i <= 15; i++) {       // interpolation the Sv_star and H_star
        if (m_star<=V_star[i]) {
            h_star = H_star[i-1]+(H_star[i]-H_star[i-1])*(m_star-V_star[i-1])/(V_star[i]-
            V_star[i-1]);
            S_star = Sv_star[i-1]+(Sv_star[i]-Sv_star[i-1])*(m_star-V_star[i-
            1])/(V_star[i]-V_star[i-1]);
            break;
        }
    }

    H = h_star*D;

    pg = -(S_star - wf.density_V/wf.density_L)*wf.density_L*9.81*sin(theta);
    pg_real = -S_star*wf.density_L*9.81*sin(theta);
```

```
    if (where=='C' ) {
        C = D*(PI-acos((D-2*H)/D));
    }
    else if (where=='E') {
        C = D*acos((D-2*H)/D);
    }
    else{
        C = 0;
    }

    // the following sectin update the heat transfer coefficient
    if (where == 'C') {
        Pr_v = wf.specific_heat_V*wf.dynamic_viscosity_V/wf.thermal_conductivity_V;
        Pr_l = wf.specific_heat_L*wf.dynamic_viscosity_L/wf.thermal_conductivity_L;
        Ja = wf.specific_heat_L*(T-Tw)/wf.latent_heat;
        Ra = g*(wf.density_L-wf.density_V)*D*D*D*wf.specific_heat_L/
            (wf.kinematic_viscosity_L*wf.thermal_conductivity_L);
        double A_l, A_v;
        A_l = 0.1*D*D*acos((D-2*H)/D)-0.125*D*D*sin(2*acos((D-2*H)/D));
        A_v = PI*D*D - A_l;
        w_v = m_dot_center/(wf.density_V * A_v);
        Re_v = w_v*D/wf.kinematic_viscosity_V ;

//      First correlation
//      Nu=0.021*pow(Pr_l,2.61)*pow(Ja,-0.568)*pow(Re_v,0.867);  //old correlation

//      The one with the constant coefficient
        Nu = 0.0642*pow(Re_v,0.867)*pow(Pr_v,1.729)+0.0133*pow(Ra,0.0298)*pow(Ja,-1.759);

//      The one with Ja in convection prediction
//      Nu=1.817*pow(Re_v,0.817)*pow(Pr_v,1.457)*pow(Ja,0.0337)+
//          0.045*pow(Ja,-0.266)*pow(Ra,0.237);

//      The one with new method  (not sucessful)
//      Nu=0.000178*pow(Re_v,1.118)*pow(Pr_v,1.92)*pow(Ja,-1.568)*5.0+
//          1.62e-6*pow(Ja,1.165)*pow(Ra,0.464)*0.728*pow(Ra,0.25)*pow(Ja,-0.25);

//      The one with only Ra and Ja
//      Nu=0.000646*pow(Ja,1.163)*pow(Ra,0.566);

        h = Nu*wf.thermal_conductivity_L/(D);
    }
    else {

        // Kandlikar paper correlation
        double Bo, Co, Fr_lo, F_fl;
        double c1, c2, c3, c4, c5;
        double Co_kand;
        Bo = fabs(Q) /(m_dot_center*wf.latent_heat);
        //Bo = 4.2e-5;
        Co = pow((1-0.5)/0.5,0.8)*pow(wf.density_V/wf.density_L,0.5);
        if (Co <=0.65) {
            c1=1.136;
            c2=-0.9;
            c3=667.2;
            c4=0.7;
            c5=0.3;
        }
        else {
            c1=0.6683;
            c2=-0.2;
            c3=1058.0;
            c4=0.7;
            c5=0.3;
        }
```

```
        Fr_lo = pow((m_dot_center*4.0/(PI*D*D)),2)/(pow(wf.density_L,2)*9.81*D);
        F_fl = 2.2;  // take as Nitrogen
        Co_kand = 1.8*c1*pow(Co,c2)*pow((25*Fr_lo),c5)+c3*pow(Bo,c4)*F_fl;

        // force convection
        Pr_l = wf.specific_heat_L*wf.dynamic_viscosity_L/wf.thermal_conductivity_L;
        double A_l, A_v;
        A_l = 0.5*D*D*acos((D-2*H)/D)-0.125*D*D*sin(2*acos((D-2*H)/D));
        w_l = m_dot_center/(wf.density_L * A_l);
        Re_l = w_l*D/wf.kinematic_viscosity_L ;
        Nu = 0.023*pow(Re_l,0.8)*pow(Pr_l,0.4);
        h = Nu*wf.thermal_conductivity_L/D;
        Nu *= Co_kand;
        h *= Co_kand;
        temp = h;
    }
}

void ControlVolume::H2m()  // From the film thickness to the liquid mass in C.V.
{
    double A_l, A_v;
    A_l=0.5*D*D*acos((D-2*H)/D)-0.125*D*D*sin(2*acos((D-2*H)/D));
    A_v= PI*D*D - A_l;

    m=A_l*dz*wf.density_L+A_v*dz*wf.density_V;
}

void ControlVolume::P_distribute_working()
{
    double dp;
    dp = pg * dz;
    p_z = p - dp/2.0;
    p_zdz = p + dp/2.0;
    //T = (1e-12)*p*p + 2e-5*p -52.375;
    T=-51.94444 + sqrt(-0.00379835+0.0036*1e-6*p)/0.0018;
    if ( where == 'A' ) {      // to keep the adiabatic section insulated
        Tw = T;
    }
}

void ControlVolume::P_distribute_upwards()        // p_z is known variable
{
    double dp;
    dp = pg*dz;
    p_z = p_zdz - dp;
    p = p_zdz - dp/2;
    //T = 1e-12*p*p + 2e-5*p -52.375;             // this is no good
    T=-51.94444 + sqrt(-0.00379835+0.0036*1e-6*p)/0.0018;
    if ( where == 'A' ) {      // to keep the adiabatic section insulated
        Tw = T;
    }
}

void ControlVolume::P_distribute_downwards() // p_zdz is know variable
{
    double dp;
    dp = pg*dz;
    p_zdz = p_z + dp;
    p = p_z + dp/2;
    //T = 1e-12*p*p + 2e-5*p -52.375;
    T=-51.94444 + sqrt(-0.00379835+0.0036*1e-6*p)/0.0018;
    if ( where == 'A' ) {      // to keep the adiabatic section insulated
        Tw = T;
    }
}

void ControlVolume::DisplayProperties(double tw, double t)
```

```
{
    wf.CO2_Properties(t);
    T=t;
    Tw=tw;
}

void ControlVolume::Pool_heat()
{
    if (H<(D-0.001)) {
        C = D*acos((D-2*H)/D);
    }
    else {
        C = PI*D;
    }
    Q = h*(T-Tw)*C*dz;

}
```

```
//-----------------------------------------------------------------------------
// --- porp.h ---
//-----------------------------------------------------------------------------

#include <stdio.h>
#include <math.h>
#include <iostream.h>

// Saturate pressure under temperature t
double dSatPres(double t);

// Latent heat under temperature t
double dLatHeat(double t);

// Specific volume of liquid under temperature t
double dSpeVolL(double t);

// Specific volume of vapor under temperature t
double dSpeVolV(double t);

// Liquid density under temperature t
double dDensitL(double t);

// Vapor density under temperature t
double dDensitV(double t);

// Specific heat of liquid under temperature t
double dSpeHeaL(double t);

// Specific heat of Vapor under temperature t
double dSpeHeaV(double t);

// Dynamic viscosity of liquid under tempertaure t
double dDynVisL(double t);

// Dynamic viscosity of Vapor under temperature t
double dDynVisV(double t);

// Kinematic viscosity of liquid under temperature t
double dKinVisL(double t);

// Kinematic viscosity of vapor under temperarure t
double dKinVisV(double t);

// Liquid thermal conductivity under temperature t
double dTheConL(double t);

// Vapor thermal conductivity under temperature t
double dTheConV(double t);

// Surface tension under temperature t
double dSurTens(double t);
```

```
//---------------------------------------------------------------------------
// --- porp.cpp ---
//---------------------------------------------------------------------------

#pragma hdrstop
#include <prop.h>
#pragma argsused

// Saturate pressure under temperature t
double dSatPres(double t)
{
    double SatPressure;
    SatPressure = 0.0009*pow(t,2)+0.0935*t+3.4835;
    SatPressure *= 1e6;              // in the SI unit of Pa
    return SatPressure;
}

// Latent heat under temperature t
double dLatHeat(double t)
{
    double LatentHeat;
    LatentHeat = -0.0337*pow(t,2)-3.1715*t+231.11;
    LatentHeat *= 1e3;               // in the SI unit of J/kg
    return LatentHeat;
}

// Specific volume of liquid under temperature t
double dSpeVolL(double t)
{
    double SpecificVolumeL;
    SpecificVolumeL = 1e-7*pow(t,2)+7.7e-6*t+0.001078;
    // in the SI unit of m3/kg
    return SpecificVolumeL;
}

// Specific volume of vapor under temperature t
double dSpeVolV(double t)
{
    double SpecificVolumeV;
    SpecificVolumeV = 5e-6*pow(t,2)-0.0003445*t+0.010231;
    // in the SI unit of m3/kg
    return SpecificVolumeV;
}

// Liquid density under temperature t
double dDensitL(double t)
{
    return 1.0/dSpeVolL(t);          // in the SI unit of kg/m3
}

// Vapor density under temperature t
double dDensitV(double t)
{
    return 1.0/dSpeVolV(t);          // in the SI unit of kg/m3
}

// Specific heat of liquid under temperature t
double dSpeHeaL(double t)
{
    double SpecificHeatL;
    SpecificHeatL = 8e-8*pow(t,5)+2e-6*pow(t,4)+2e-5*pow(t,3)+
        0.0008*pow(t,2)+0.0316*t+2.5464;
    SpecificHeatL *=1000;            // in the SI unit of J/kg_K
    return SpecificHeatL;
}

// Specific heat of Vapor under temperature t
```

```
double dSpeHeaV(double t)
{
    double SpecificHeatV;
    SpecificHeatV = 1e-7*pow(t,5)+4e-6*pow(t,4)+3e-5*pow(t,3)+
        0.0012*pow(t,2)+0.0478*t+1.8723;
    SpecificHeatV *=1000;              // in the SI unit of J/kg_K
    return SpecificHeatV;
}

// Dynamic viscosity of liquid under tempertaure t
double dDynVisL(double t)
{
    double DynamicViscosityL;
    DynamicViscosityL = 0.0084*pow(t,2)-1.8031*t+99.426;
    DynamicViscosityL *= 1e-6;         // in the SI unit of Pa_S
    return DynamicViscosityL;
}

// Dynamic viscosity of Vapor under temperature t
double dDynVisV(double t)
{
    double DynamicViscosityV;
    DynamicViscosityV = 2e-6*pow(t,4)+6e-5*pow(t,3)+0.0015*pow(t,2)+
        0.104*t+14.788;
    DynamicViscosityV *= 1e-6;         // in the SI unit of Pa_S
    return DynamicViscosityV;
}

// Kinematic viscosity of liquid under temperature t
double dKinVisL(double t)
{
    return dDynVisL(t)/dDensitL(t);    // in the SI unit of m2/s
}

// Kinematic viscosity of vapor under temperarure t
double dKinVisV(double t)
{
    return dDynVisV(t)/dDensitV(t);    // in the SI unit of m2/s
}

// Liquid thermal conductivity under temperature t
double dTheConL(double t)
{
    double ThermalConductivityL;
    ThermalConductivityL = -1.2236*t+110.3;
    ThermalConductivityL *= 1e-3;      // in the SI unit of W/m_K
    return ThermalConductivityL;
}

// Vapor thermal conductivity under temperature t
double dTheConV(double t)
{
    double ThermalConductivityV;
    ThermalConductivityV = 1e-5*pow(t,4)+0.0004*pow(t,3)+
        0.0077*pow(t,2)+0.324*t+19.687;
    ThermalConductivityV *= 1e-3;      // in the SI unit of W/m_K
    return ThermalConductivityV;
}

// Surface tension under temperature t
double dSurTens(double t)
{
    double SurfaceTension;
    SurfaceTension = 9e-7*pow(t,2)-0.0002*t+0.0045;
    // in the SI unit of N/m
    return SurfaceTension;
}
```